THE APPLICATION OF MONOCHROMATIC PHOTONEUTRON SPECTROSCOPY IN AN EXAMINATION OF NUCLEAR ENERGY LEVELS OF ^{180}Ta, ^{202}Tl AND ^{204}Tl

By

© THOMAS COUSINS, B.Sc., M.Sc.

A Thesis

Submitted to the School of Graduate Studies

in Partial Fulfilment of the Requirements

for the Degree

Doctor of Philosophy

McMaster University

November 1982

MONOCHROMATIC PHOTONEUTRON SPECTROSCOPY

DOCTOR OF PHILOSOPHY (1982)
(Physics)

McMASTER UNIVERSITY
Hamilton, Ontario

TITLE: The Application of Monochromatic Photoneutron Spectroscopy In An Examination of Nuclear Energy Levels of ^{180}Ta, ^{202}Tl And ^{204}Tl

AUTHOR: Thomas Cousins, B.Sc. (University of Windsor)
M.Sc. (McMaster-University)

SUPERVISOR: Professor T.J. Kennett

NUMBER OF PAGES: xv,195

ABSTRACT

Monochromatic photons from in-core neutron capture sources of aluminum, copper, iron, nickel and chromium were used to initiate the (γ,n) reaction on the ^{181}Ta, ^{205}Tl and ^{203}Tl nuclei. The use of this method allows precise measurement of the Q values for the $^{181}Ta(\gamma,n)^{180}Ta$ (7579 ± 2 Kev) and the $^{205}Tl(\gamma,n)^{204}Tl$ (7549 ± 1 Kev) reactions. Comparison of the $^{181}Ta(\gamma,n)$ data with the $^{180}Ta(n,\gamma)$ data confirms the existence of an isomeric state in ^{180}Ta at 73 ± 2 Kev. Over twenty previously unobserved levels in ^{180}Ta were populated with typically 2 Kev precision in energy determination. Well-documented levels in ^{204}Tl were observed to also be populated.

The total (γ,n) cross sections were measured and the gamma ray strength functions were deduced for the stronger (γ,n) channels. The small incident gamma ray energy spread of a few ev allows excitation of individual excited state resonances in ^{205}Tl, while averaging over many compound resonances in ^{181}Ta is observed. The number of degrees of freedom for a Porter-Thomas distribution of reduced widths was also estimated and gave some credence to the deduced γ-ray strength functions. Attempts to assign spin and parity in the residual ^{180}Ta and ^{204}Tl nuclei were thwarted by the assumption of a dominant electric-dipole absorption cross section, and by the half-integer ground state spins of the ^{205}Tl and ^{181}Ta targets.

ACKNOWLEDGEMENTS

Firstly I would like to thank my supervisor, Dr. Terry Kennett for putting up with me for six years without becoming completely frustrated. He and Dr. Bill Prestwich were always enthuiastic, encouraging and sympathetic with respect to the problems associated with experimental nuclear physics while maintaining their sanities and senses of humour.

The staff of the Health Physics Department at the reactor was always available and helpful. Special thanks here go to Dr. John Harvey for helpful hints on experimental safety and short iron play.

The Reactor Supervision Staff were of great aid - particularly Mr. Morley Davis, Mr. Nick "Where's Teenage Head playing this week?" Vandervleit, and Mr. Mike "Which source is it this Monday, Cousins?" Batler. The latter was particularly valuable after Sunday Goon festivals with Eccles.

For design and implementation of the electronics used in this thesis, no one could have been more helpful than Mr. Kenrick Chan.

Special thanks to Miss Brenda Pershaw for doing a super job in typing up this usually incoherent and illegible original manuscript.

Perhaps the most important people in keeping me going through my lengthy stay are Mr. Harry (John) Mendolsen and his fine staff and Anna.

Many thanks to Dr. Nick Barkman for the much help he gave me through the entire stay - in technical aspects, punkouts, and the opening of his halfway house. Those other birds of N.R.B. have all contributed in their own way to making me feel at home, especially Tervo, Eddie Rabbit, Carmichael, Chris, Colm, Gary and Bill.

Finally to all the various members of the Nuclods/Oldclods (Dione, Leo, Pete, etc.), Ferrets (McGrattan, the big guy, Carlos, etc.), Slender Members (Al, Vytas Rickey, Lise, etc.), Snegmatics (Captain Wussy, Shagabugger, Kim, Stirrup, Connie, etc.) and Degenerate states (Gord, Freddie, etc.), thanks for reinforcing my view that there are still people in the world who realize there is more to academic life than academics.

TABLE OF CONTENTS

TABLE OF CONTENTS (CONT'D)

TABLE OF CONTENTS (CONT'D)

TABLE OF CONTENTS (CONT'D)

LIST OF ILLUSTRATIONS

LIST OF ILLUSTRATIONS (CONT'D)

LIST OF ILLUSTRATIONS (CONT'D)

LIST OF ILLUSTRATIONS (CONT'D)

LIST OF TABLES

LIST OF TABLES (CONT'D)

LIST OF TABLES (CONT'D)

CHAPTER ONE

1.0 INTRODUCTION

Since the very first experiments on the photodisintegration of the deuteron (Ch 34), the field of photonuclear spectroscopy has proven a valuable tool for both experimental and theoretical nuclear structure studies. Early experimenters in the photoneutron field were limited by poor energy resolution of both photon sources and neutron detection systems and accordingly their work concerned almost exclusively gross structures of the neutron energy spectrum - chiefly the massive Giant Dipole Resonance. Studies of this phenomenon led to the development of such theories as the hydrodynamic model of the nucleus (Go 48, St 50) and microscopic shell model calculations (Br 57, Br 59).

In recent years however technological advances have allowed studies of the fine structure of the photoneutron reaction. In particular experimenters at this facility (Mc 77, Ba 81) have devised a system in which these energy resolution problems are circumvented. The system makes use of monochromatic photons generated by thermal neutron capture in the core of a nuclear reactor, in concert with a high resolution ^{3}He gridded ionization chamber as a neutron detector.

This work has shown that when such a γ ray beam is allowed to strike a monoelemental (or monoisotopic) target of mass A, (where A ~ 200) then the (γ,n) reaction produces neutron groups of distinct energy. These neutron energies may be related to the nuclear energy levels in the residual (mass A - 1) nucleus via the equation

$$E_n = \frac{A - 1}{A}(E_\gamma - Q - E_x)$$

where E_n = neutron energy

A = mass number of the target nucleus

$A - 1$ = mass number of the residual nucleus

E_γ = incident photon energy

Q = photoneutron Q value

E_x = excited state energy in the residual nucleus

It is an expansion of this technique which is to be presented here, whereby a variety of incident γ ray energies are allowed to impinge upon natural Tantalum and Thallium targets. As a result, information about the energy levels in ^{180}Ta, ^{202}Tl and ^{204}Tl is garnered.

In section 1.1, the superiority of this method over other methods of photoneutron spectroscopy is discussed, while the reasons behind the choice of the above nuclei as targets are presented in section 1.2.

1.1 Superiority of the Method

From the previous section, the primary factors governing the applicability of photoneutron spectroscopy as a tool for revealing nuclear energy level information are the energy resolution of both the incident γ ray and the neutron detector.

1.1.1 Photon Sources

Sources of monochromatic photons for photoneutron spectroscopy may be divided into three major classes:

(i) Bremsstrahlung photon beams

(ii) Positron annihilation in flight

(iii) Photons produced in nuclear excitations.

The third group above may be subdivided into beams produced from (n,γ) or (p,γ) sources or those produced from nuclear resonance scattering of Bremsstrahlung.

Table (1.1) lists typical energy resolution associated with each photon production method. The methodology behind each reaction will not be discussed here, it having already been covered in an excellent review article by Bergere (Be 76). The major point is, of course, the far greater resolution attained by thermal neutron capture gamma ray sources.

TABLE 1.1

PHOTON ENERGY RESOLUTION FROM VARIOUS EXPERIMENTAL TECHNIQUES

TECHNIQUE	RESOLUTION	REFERENCE
1) Bremsstrahlung		
a) High Energy Tip		Fi 70a
b) Magnetic Pair Spectrometer	120 Kev at 10 Mev	Do 66
c) Compton Spectrometer	500 Kev at 20 Mev	Be 69a
d) Spectrometer using NaI Crystals	200 Kev at 10 Mev	Wy 65
e) Double Axis Compton Spectrometer	100 Kev at 10 Mev	Ah 73
f) Tagged Photon Beams	100 Kev at 10 Mev	OC 62
2) Positron Annihilation in Flight	75 Kev at 10 Mev	Fu 62
3) Nuclear Reactions		
a) $^{7}_{3}Li(p,\gamma)^{8}_{4}Be$	20 Kev at 17.6 Mev	Me 66
b) $^{13}_{6}C(p,\gamma)^{14}_{7}N$	25 Kev at 9.18 Mev	Ha 57
c) $^{27}Al(p,\gamma)^{28}Si$	20 Kev at 12.33 Mev	Me 58
d) $^{3}_{1}H(p,\gamma)^{4}_{2}He$	100 Kev at 22 Mev	Lo 66
e) Thermal Neutron Capture	~1 ev at all Energies	

For the experiments conducted and reported on here the gamma ray source was positioned in a reactor core and, thus, the resolution is chiefly governed by Doppler broadening due to thermal motion of the source atoms. This may be written as:

$$\frac{\Delta E}{E_\gamma} = \left(\frac{2kT}{Mc^2}\right)^{\frac{1}{2}} \qquad (1.1.1)$$

where k = Boltzmann's constant

M = Mass of the source atom

T = Temperature

E_γ = Photon energy

ΔE = Energy spread

Substituting, for γ ray energies of the order of 10 Mev, and $M \sim (30\text{-}70)$ a.m.u., yields $\Delta E \sim$ lev. Thus neutron capture γ rays provide the optimum energy resolution for photoneutron spectroscopy, however there is one major drawback to their use and this lies in the discrete nature of their energy spectra. Whereas Bremsstrahlung beams, positron annihilation beams and photon beams from the ${}_1^3H(p,\gamma)_2^4He$ reaction are variable over a wide energy range up to 100 Mev, any one particular capture γ ray source will yield only a few strong intensity lines over a finite energy range. For all practical purposes, when performing photoneutron spectroscopy E_γ must be greater than the photoneutron Q-value (approx 7 Mev) and almost all strong intensity lines have $E_\gamma < 10$ Mev. The only exceptions to the latter statement are the

10.83 Mev line arising from neutron capture in nitrogen, and the 11.387 Mev line arising from neutron capture in ^{59}Ni. However because of the low capture cross section in N(77.2 ± 2.1 mb, Is 81), the low number of γ rays (0.15) per disintegration (Ra 67), and the low density of nitrogen-containing compound such nitrogen sources in general yield low photon fluxes. In the case of nickel, ^{59}Ni has a 7.5 x 10^4 year halflife (Le 78) and may only be built up following neutron capture in ^{58}Ni, again limiting flux. There are, however, a number of examples of the use of the two transitions as γ ray sources, for example in Raman spectroscopy (Ja 75).

The discrete nature of γ ray energies is particularly distressing because of the fact that the photoneutron energy varies as $(E_\gamma - Q - E_x)$, and since most neutron detectors are more efficient at lower energies, one would like to set this value as close to zero as possible in order to see all energy levels populated with maximum statistical precision. Another problem arising from the use of neutron capture sources stems from the fact that if any one source has two strong lines separated by energy E_γ^1 then any excited state energy E_x may only be uniquely determined if $E_x < E_\gamma^1$.

The method presented here provides a technique to at least partially circumvent these problems. An examination of the literature reveals that in the range from 7 to 10 Mev there are a number of strong intensity γ rays from a variety of sources. The energies, intensities, cross sections and sources of these lines are presented in Table (1.2).

TABLE 1.2

PROMPT γ RAYS FROM THERMAL NEUTRON CAPTURE

ELEMENT	σ_c (barns) (BNL 325)	E_γ (Mev) (Ra 67)	I_γ (Ra 67) (No./100)
Iron	2.62 ± 0.6	7.632	27.19
		7.642	22.14
		9.298	3.08
Aluminum	0.235 ± .005	7.694	0.83
		7.724	16.58
Copper	3.85 ± .03	7.637	14.47
		7.915	28.40
Nickel	4.6 ± .1	7.819	9.04
		8.121	3.47
		8.533	18.74
		8.999	41.65
Chromium	3.1 ± .20	7.939	11.41
		8.484	4.06
		8.512	5.50
		8.884	24.14
		9.720	9.82

By interchange of in-core γ ray sources it is then possible to vary E_γ over a wide (3 Mev) energy range, albeit not continuously.

The methodology used in this thesis is to start with the lowest energy γ ray available (from an Aluminum source) in order to populate the ground state of the residual nucleus. This ground state transition will then be seen with maximum detector efficiency establishing the photoneutron Q value with greatest accuracy. By systematically increasing E_γ, with the interchange of sources, the excited states may be seen to grow in with corresponding neutron energies being made as low as possible. Since no two sources have strong lines separated by the same energy difference E_γ^1 the previously mentioned ambiguity in assigning energy levels will disappear.

Thus excited state energy levels can be easily and uniquely determined. Also, as will be pointed out in Chapter 2 the photoneutron cross sections as a function of neutron energy, as well as the angular distribution of these neutrons allow inference of spin and parity assignments.

1.1.2 Neutron Detection

Conventional methods of neutron detection are well documented (Ma 60). Among the most popular types are BF_3 proportional counters, time of flight neutron spectroscopy, ^3He neutron chambers, and organic

scintillators (both liquid and plastic). Of these four, only the ^3He detectors are suited for the experiments to be carried out here for the reasons outlined below.

The BF_3 detector relies on the $^{10}B(n,\alpha)^7Li$ reaction. The (n,α) cross section varies as $\frac{1}{v}$ and is comparable to the $^3He(n,p)^3H$ cross section to 1 Mev. However the high Q value (+2801 ± 4 Kev, Wa 77) of the reaction makes energy resolution poor. In photoneutron experiments, BF_3 detectors are surrounded by a moderating material such as wax in a "long counter" configuration (Al 60). Clearly, no energy information can be extracted.

Time of flight spectroscopy (Ne 60), relies on the measurement of a delayed coincidence between a reference time (i.e. the time when a burst of neutrons is produced) and the detection time of an event. For photoneutron spectroscopy the emitted neutrons must be produced in bursts with the use of a "chopper", or rotating mechanical shutter. For Kev neutrons however the steel shutters provide incomplete neutron attenuation, which, coupled with the large (~10 m) chopper to detector distance yielding small solid angle and efficiency, make this method also impractical.

The organic scintillators (Mu 60) with their threshold energy levels and limited energy resolution (~150 Kev at 1 Mev) are restricted to examining gross features of high energy neutron spectra.

In recent years, advances in the manufacture of ^{3}He gridded ionization chambers have resulted in detectors with excellent energy resolution (12 Kev for thermal neutrons, 27 Kev for 1 Mev neutrons) and reasonable efficiencies up to 2 Mev (Cu 71). Since when dealing with the energy level structures of odd-odd nuclei in the A = 180-200 range one may expect average spacings of order of 50 Kev, the superiority of this kind of neutron detector is apparent.

A brief discussion of the salient features of the ^{3}He detector relating to photoneutron spectroscopy is presented in secs. (4.1) and (4.4). A more complete discussion is given by McFee (Mc 77).

1.2 Energy Levels in ^{180}Ta, ^{202}Tl and ^{204}Tl

1.2.1 ^{180}Ta

The reason for the application of photoneutron spectroscopy as a technique for investigation of the nuclear energy level structure of ^{180}Ta is readily apparent when one examines the literature (i.e. Le 78). The energies, spins and parities of these levels as well as the $^{181}Ta(\gamma,n)^{180}Ta$ Q-value are shrouded in controversy and ambiguity. A brief discussion of the quest for these energy level assignments and the problems encountered therein, is given below.

^{180}Ta occurs in nature with isotopic abundance of 0.0123% (Wh 56) and from the systematics of nuclidic masses (Wa 77) it is known

that beta decay to both ^{180}Hf and ^{180}W is energetically possible. A lower limit of 10^{13} years (Ar 77) has been established for this half life of this naturally occurring configuration.

The production of ^{180}Ta in nuclear reactions yields a configuration which decays with an 8.15 hour half-life (Br 51). On the basis of early photoneutron threshold experiments by Geller et al (Ge 60) the 8.15 hour configuration was originally identified as an isomeric state lying 212 ± 23 Kev above the ground state.

Recently, however, several experiments have contradicted these results. Firstly, a Q-value of 7653 ± 4 Kev was reported by Lanier et al (La 72) for the $^{180}Ta(n,\gamma)^{181}Ta$ reaction - which clearly involves neutron capture only in the long-lived configuration. Secondly, recent experiments at this facility (Ba 79), used nickel capture photons to report the neutron binding energy in ^{181}Ta as only 7580 ± 5 Kev. Combining these two results places the long-lived configuration at an excitation energy of 73 ± 6 Kev, and thus constitutes a naturally occurring isomer.

Confirmation of these results has come from two other more recent publications. Sharma and associates (Sh 80) have reported a mass-spectrometric value of 7693 ± 20 Kev for the mass difference between the long-lived ^{180}Ta configuration coupled to a free neutron and ^{181}Ta. From a consideration of the Q-value for the beta decay of the short-lived state to ^{180}W, together with the ^{181}Ta - ^{180}W mass

difference, these authors also identify the short-lived configuration as the ground state of ^{180}Ta. Finally Warde et al (Wa 79) conducted angular distribution measurements on the ^{181}Ta(p,d)^{180}Ta reaction and assign the ground state spin and parity as 1^+. This paper also reports 5 states in ^{180}Ta with excitation energies under 302 Kev, and together with the levels quoted from another (γ,n) experiment at this facility (Mc 77) provide the only energy information thus far. It should be pointed out however, that the latter paper has energy uncertainties of at least ±9 Kev for all excited states, while the former paper quotes "no energy uncertainties".

1.2.2 The Thallium Isotopes

The usefulness of a study of the thallium isotopes using photoneutron spectroscopy can be seen by viewing Figs. (1.1) and (1.2) (copied from Le 78).

The excitation energies of the levels in ^{204}Tl are well known from ^{203}Tl(n,γ)^{204}Tl experiments (Fu 73). There do exist, however, some tentative levels (the dashed lines in Fig. (1.1)). In addition the spins and parities of many levels are not well-known. Of particular interest is the ground state ambiguity in spin.

The energy level picture in ^{202}Tl is not nearly so clear. For the most part, the results of the ^{203}Tl(p,d)^{202}Tl(Au 71) and the experiments involving decay to ^{202}Tl from $^{202m}_{82}$Pb (Gu 72) do not

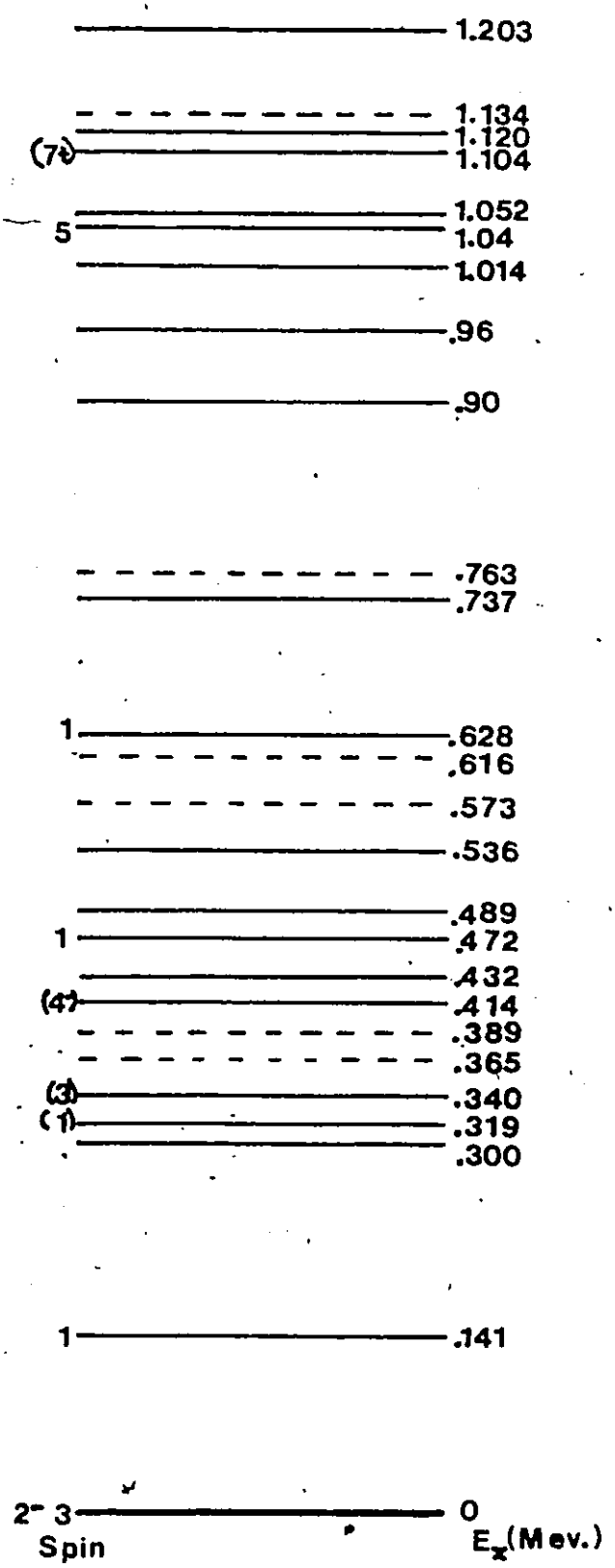

Figure 1.1 Nuclear Energy Levels in ^{204}Tl

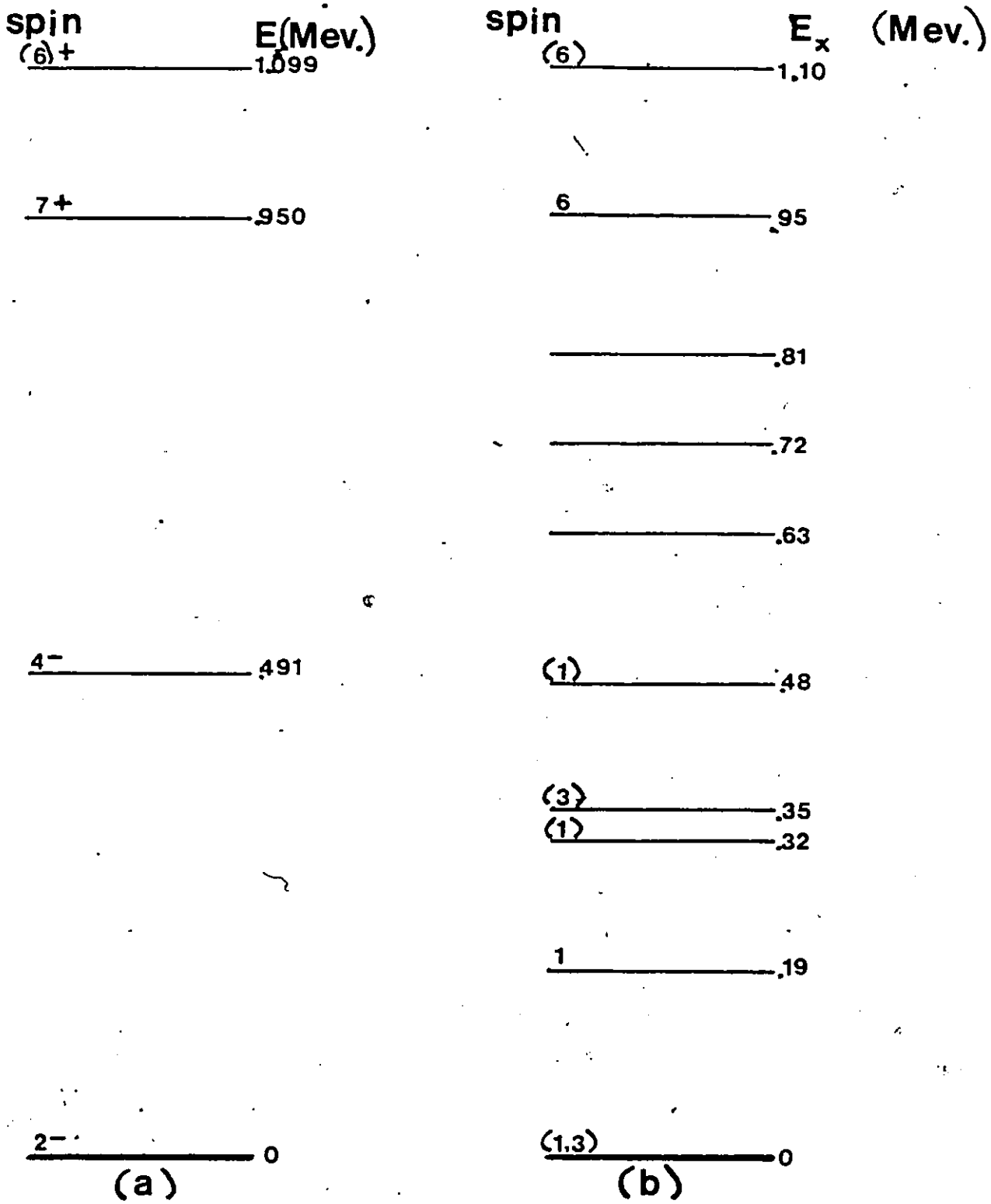

Figure 1.2 Nuclear Energy Levels in ^{202}Tl

a) from $^{203}Tl(p,d)^{202}Tl$ Reaction

b) from decay of ^{202m}Pb

coincide. In addition, the accuracy in determining many of the energy levels is not good.

The photoneutron Q-values are:

$Q\{^{205}Tl(\gamma,n)^{204}Tl\}$ = -7548 ± 3 Kev(Mc 77); -7555 ± 6 Kev (Wa 77)

$Q\{^{203}Tl(\gamma,n)^{202}Tl\}$ = -7737 ± 3 Kev(Mc 77); -7720 ± 20 Kev (Wa 71)

The reasons for using the thallium isotopes are three-fold:

a) By using the well known energy levels in ^{204}Tl, the theories to be developed in Chapter 2 may be tested before being applied to ^{180}Ta.

b) More information concerning the energy levels in ^{204}Tl and ^{202}Tl may be derived.

c) The photoneutron Q values may be measured to greater accurracy.

1.3 Brief Statement of Goals

The use of monochromatic photons of varying energy as sources for (γ,n) experiments should provide, if coupled with a high resolution ^{3}He neutron detector, an effective means of unravelling the problems associated with many unknown or ambiguous nuclear energy level assignments.

Identification of the incident γ ray energy associated with each neutron group gives straightforward values for the photoneutron Q value and excitation energy assignments. As will be shown in Chapter 2, the measurement of the photoneutron cross section for any one particular neutron energy group as a function of either neutron energy or emission angle may be used to infer spin and parity assignment to these levels, or to examine whether the photoneutron reaction proceeds on or off resonance.

In this experiment, these techniques may be used to examine ^{180}Ta, ^{204}Tl and ^{202}Tl. Whereas the void of reliable information on the first nucleus has been described, there exists enough knowledge on the latter two to verify the methodology to be used, while at the same time unravelling some discrepancies.

CHAPTER TWO

2.0 THEORY

2.1 The Interaction of Gamma Rays with Nuclei

The photoabsorption cross section as a function of incident γ ray energy follows very definite trends for any nucleus. These features are outlined below, more complete discussions can be found elsewhere (Be 76, Ha 76b, Sa 74).

In the energy region below the photoneutron threshold, photon scattering is the only process which can occur. Excitation into individual bound nuclear levels and Thompson scattering by the whole nuclear charge are the major mechanisms. Experiments using neutron capture γ ray sources in this region have reported several instances of the photon energy overlapping the bound resonance energy (Mo 70).

Just above the particle emission threshold (which occurs in the region of 6-8 Mev for heavy nuclei) the cross section begins to rise slowly. The (γ,n) reaction exhausts the particle production cross section as, especially for heavy elements, the Coulomb barrier prevents the (γ,p) reaction. In this region the density of states is still low enough in many nuclei to allow individual unbound levels associated

with the nuclear shell model effects to be excited. Collective modes (see sec. 2.2) may also be excited as components of the M1 and E2 resonances may be expected in this region. However the tail of the Giant Dipole Resonance is beginning to dominate.

Above photon energies of approximately 10 Mev the individual nuclear level structure of the cross section overlaps and the massive Giant Dipole Resonance dominates the spectrum.

This structure may be viewed as the interaction between the photon and the nuclear electric dipole moment from the oscillation of protons and neutrons against each other. The mean energy of the GDR has been both experimentally and theoretically shown to be $80A^{-1/3}$ Mev, where A is the nuclear mass number. This places the GDR at approximately 14.2 Mev in Ta and 13.6 Mev in Tl.

Since its discovery the GDR has pointed to a plethora of theoretical interpretations. These theories can basically be divided into two groups - the collective models and the microscopic models.

The collective (or hydrodynamic) models have at their origin the work of Goldhaber and Teller (Go 48) or Steinwedel and Jensen (St 50). Both models have as their basis the view of the nucleus as a combination of interpenetrating proton and neutron fluids, and the GDR representing a single normal vibrational mode of the fluid - thus the term hydrodynamic. These theories, and various extensions of them,

have proven particularly accurate at explaining such gross features as the splitting of the GDR for oblate, prolate and deformed nuclei (Be 69b, Ke 69, Ca 74). This GDR splitting has been shown to occur in the $^{181}Ta(\gamma,n)^{180}Ta$ cross section (Fu 58).

The microscopic models, as originally developed by Brown and Bolsterli (Br 59) take the view that the photon, as electromagnetic radiation, acts though a one-body operator, first creating a 1 particle -1 hole $|1p - 1h\rangle$ state in the target nucleus. The residual particle-hole interaction builds up a collective state which is a coherent sum of all such $|1p - 1h\rangle$ component states and which is pushed upward in energy carrying all the dipole strength. Both theories have found general acceptance, and the choice between the two in general is left to the individual experimenter.

The GDR continues to dominate the photoabsorption cross section up to about 25 Mev, with $(\gamma, 2n)$ and (γ,np) reactions becoming increasingly possible. At about 25 Mev the photon wavelength is small enough that short range correlations between the nucleons (such as the quasi-deuteron effect (Le 51)) are seen. Finally at extremely high energies ($E_\gamma > 100$ Mev) the photon wavelength is so small that individual nucleon resonances may be excited (i.e. photomeson production).

Figure (2.1) gives clarification to the processes discussed above.

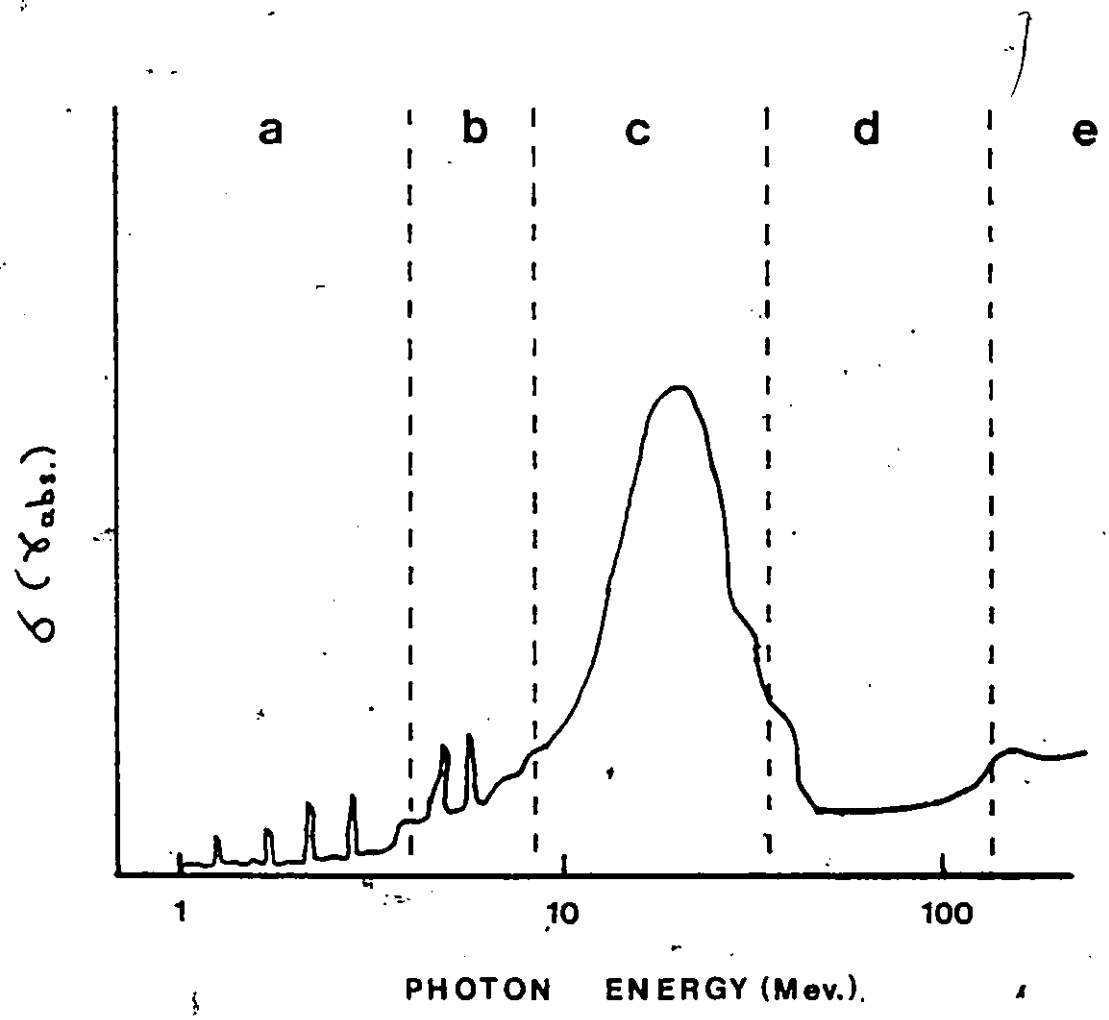

Figure 2.1 The γ Ray Absorption Cross Section

a) Excitation of Bound Resonances and Thomson Scattering
b) Excitation of Unbound Individual Excitated States. Tail of G.D.R.
c) Giant Resonance Excitations
d) Quasi-deutron effect and short-range correlations
e) Photomeson Region-excitation of individual nucleon resonances.

2.2 Giant Multipole Resonances

Whereas the GDR has been shown to dominate the photoneutron spectrum, other collective modes may also be excited in the photon energy region of 7-10 Mev. A brief discussion of these modes is presented below. A more complete discussion is given by Hanna (Ha 76a).

The giant multipole resonances may be classified according to the basic oscillations of a nucleus as done in Fig. (2.2), differentiation is made between electric and magnetic oscillations as well as isoscalar and isovector modes of oscillation.

The isoscalar electric modes are characterized by oscillations of the nucleus as a whole in which the protons and neutrons move in phase without any differentiation of spin. These are the oscillations of a charged liquid drop. In the isovector electric modes the protons oscillate against the neutrons without any spin differentiation. The GDR is an electric dipole (E1) resonance.

Magnetic modes are characterized by oscillations involving spin rather than charge. In the isoscalar vibrations protons and neutrons with spin up oscillate against protons and neutrons with spin down, while in the isovector modes protons with spin up oscillate against neutrons with spin up, and neutrons with spin down against protons with spin down.

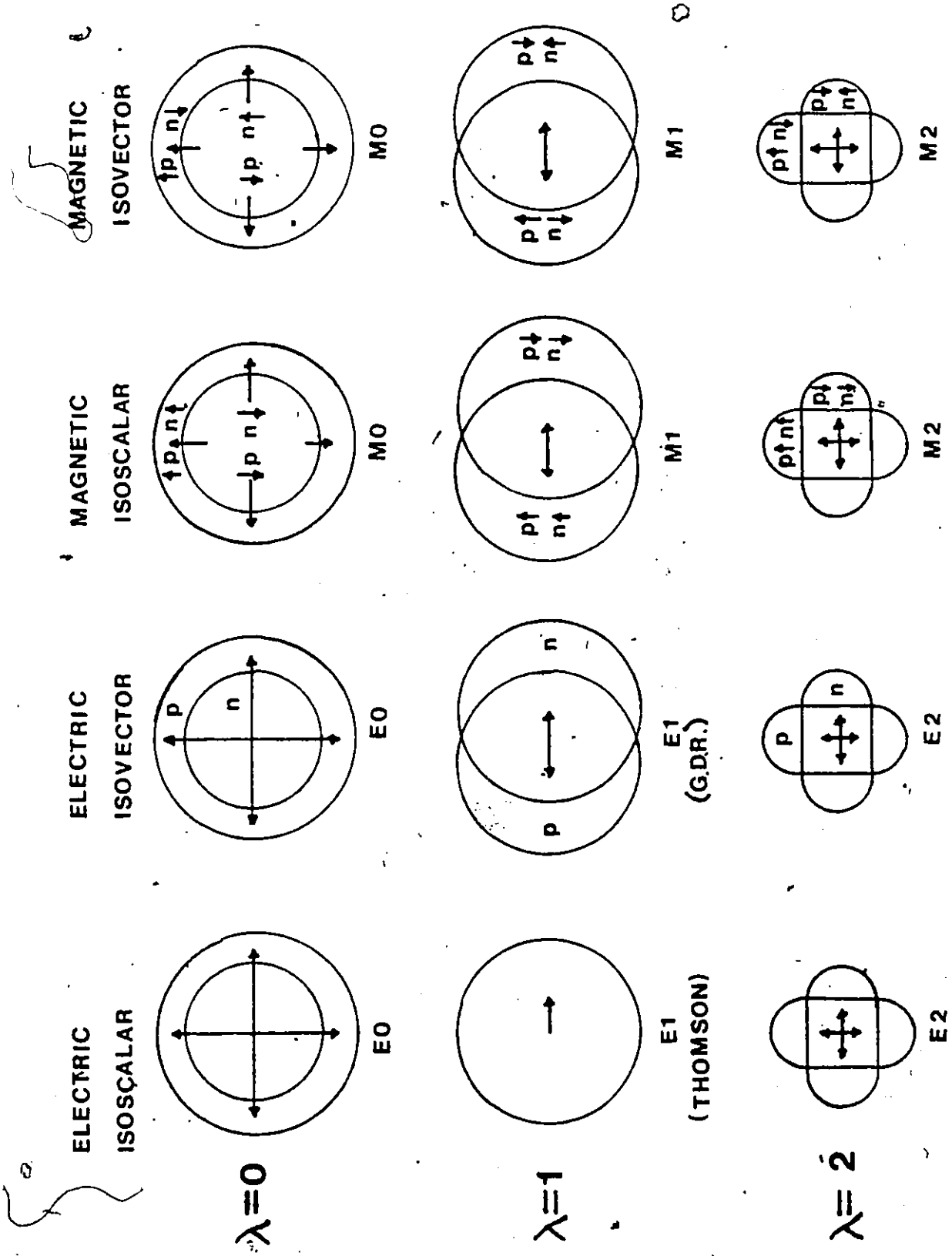

Figure 2.2 Giant Multipole Oscillations

In the energy region of interest, both the M1 isovector mode and the E2 isoscalar mode have been demonstrated to show strength. The properties of these resonances in relation to the GDR are listed in Table (2.1).

2.3 Monochromatic Photoneutron Spectroscopy for 7-10 Mev Photons

As discussed in the preceeding section, the photoneutron cross section in the region of 7-10 Mev represents the tail of the GDR, with individual unbound level resonances superimposed upon it, with perhaps some contributions from the M1 isovector and E2 isoscalar giant resonances. Depending on the density of states at energy E_γ in the target nucleus, the photon may overlap a number of unbound resonances, or excite one resonance level only or reach the continuum between them. The consequences of the last statement are discussed more in the following sections.

For the purpose of energy level assignments, regardless of the nature of the excited state reached, one may view the photoneutron reaction as shown in Fig. (2.3), where we have

$$\gamma + {}^{N}_{Z}A \rightarrow {}^{N}_{Z}A^{*} \rightarrow n + {}^{N-1}_{Z}(A-1) \qquad (2.3.1)$$

where

${}^{N}_{Z}A$ is the target nucleus of mass A

TABLE 2.1

PROPERTIES OF GIANT MULTIPOLE RESONANCES

RESONANCE	EXCITATION ENERGY E(Mev)
E1 (isovector)	$80/A^{1/3}$
E2 (isovector)	$130/A^{1/3}$
E2 (isoscalar)	$60/A^{1/3}$
M1 (isovector)	$45/A^{1/3}$

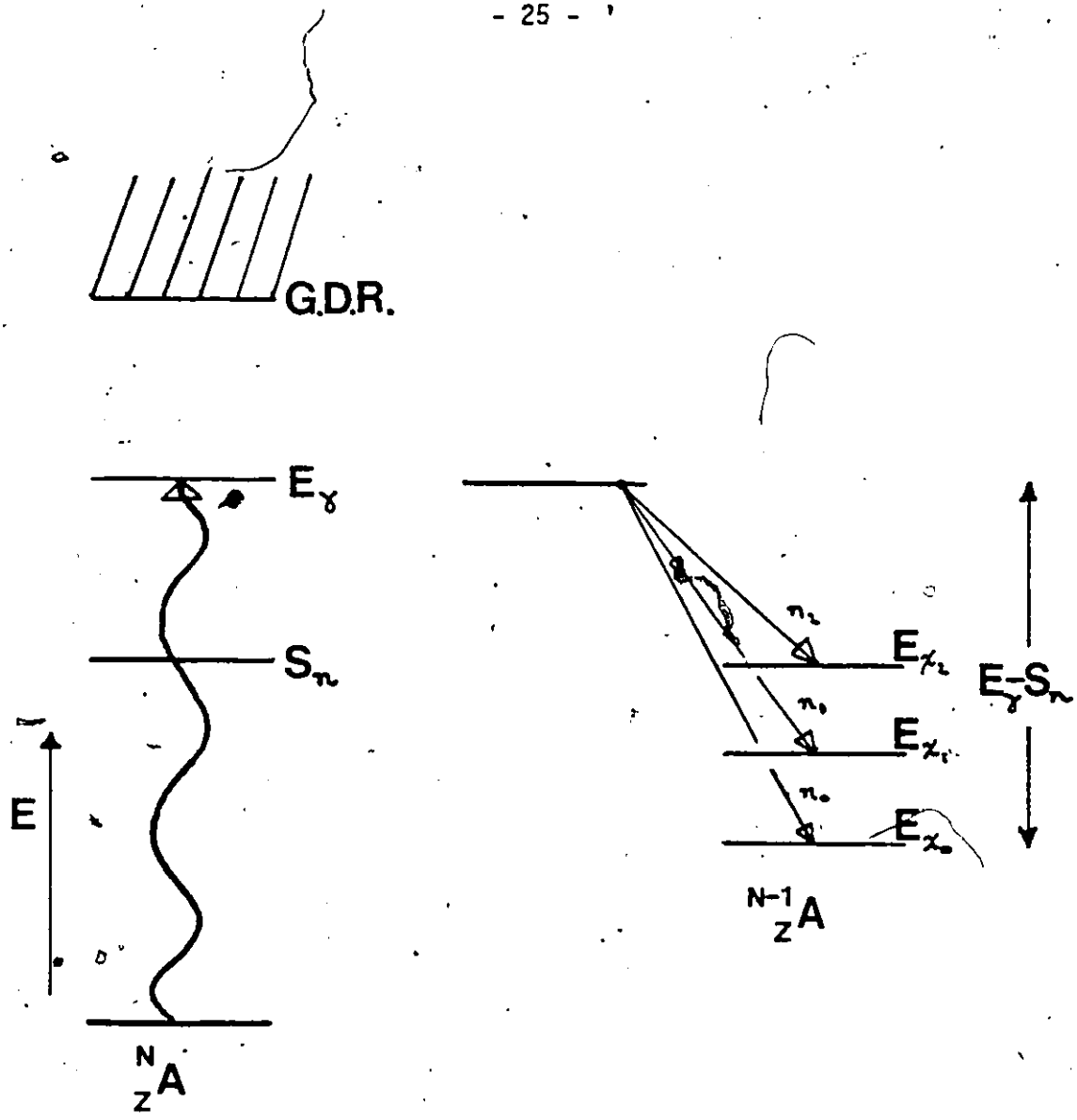

Figure 2.3 Schematic Diagram of Monochromatic Photoneutron Spectroscopy

$^{N}_{z}A^{*}$ is the excited state of the target nucleus following photon absorption

$^{N-1}_{z}(A - 1)$ is the residual nucleus

From the schematic representation, when a photon of energy E_γ strikes the target then provided $E_\gamma > S_n$ (the neutron binding energy) and $E_\gamma <$ GDR (the giant dipole resonance energy) the intermediate state $^{N}_{z}A^{*}$ is created. This state may then decay by neutron emission to one of excited states x_i in $^{N-1}_{z}(A - 1)$. It can easily be shown (Mc 77) that to great accurracy the neutron energy, E_{n_i}, associated with decay to the excited state x_i, is

$$E_{n_i} = \frac{A - 1}{A}(E_\gamma - S_n - E_{x_i}) \qquad (2.3.2)$$

2.4 Level Densities in Tantalum and Thallium

Before proceeding to the next sections it may be wise to consider the probability of the photon overlapping with the unbound resonance energy levels in the target nucleus. To do this we need knowledge of the level densities in both the tantalum and thallium nuclei. Such information is contained in the work of Gilbert and Cameron (Gi 64). These authors have developed a formula to predict

energy level densities over a wide energy range for any nucleus. Their method involves using a constant nuclear temperature representation at low excitation energies, while at high excitation energies the Fermi gas model is used.

Thus at energies corresponding to the gamma ray energies used here

$$s = K \exp(2\sqrt{a\,E}) \qquad (2.4.1)$$

where s = level density

E = excitation energy

K, a = constants determined from pairing energies and shell correction factors

Table (2.2) gives the level densities of all spins and parities at the individual γ ray energies to be used. Considering a gamma ray with full-width half-maximum of ~ 1 eV, then the cases are quite different for ^{181}Ta and ^{205}Tl. In the former case, the gamma ray may be seen to overlap with many resonances, while for the latter the level spacing is wider than the γ ray width. The case for ^{203}Tl lies somewhere in between.

One may expect then, that the photoneutron cross-section for Tantalum may exhibit much smoother varying structure with increasing γ ray energy than that for the Thallium isotopes which may exhibit fluctuations depending on whether the γ ray energy overlaps a resonance energy or not.

TABLE 2.2

PREDICTED ENERGY LEVEL DENSITIES IN Ta AND Tl

GAMMA RAY ENERGY (Mev)	DENSITY (per. ev)	AVERAGE SPACING (ev)
^{203}Tl		
7.724	.163	6.13
7.915	.204	4.90
8.533	.416	2.41
8.884	.616	1.62
8.999	.699	1.43
9.720	1.528	0.65
^{205}Tl		
7.724	.016	60.5
7.915	.020	50.3
8.533	.037	28.0
8.884	.049	20.2
8.999	.055	18.2
9.720	.101	9.6
^{181}Ta		
7.724	15.95	6.27×10^{-2}
7.915	21.32	4.67×10^{-2}
8.533	53.36	1.87×10^{-2}
8.884	88.58	1.13×10^{-2}
8.999	104.37	9.58×10^{-3}
9.720	285.53	3.50×10^{-3}

2.5 Orbital Angular Momentum of Emitted Neutrons

When assigning spins and parities to specific nuclear energy levels, the most important consideration is the orbital angular momentum of the emitted photoneutron. An examination of the angular distribution of the emitted photoneutrons may yield some information concerning the spins and parities of the excited state in the target nucleus as well as the populated level in the residual nucleus. In order to demonstrate how these features are related, we will follow closely along the lines of Carr and Baglin (Ca 71). Referring to Fig. (2.4) we have, as in the previous section, a photon incident upon a target nucleus of mass A, however we now choose to assign spins and parities as follows:

$J_A^{\pi_A}$ are the spin and parity of the ground state in the target nucleus

P is the nature of the excitation (p = 0 for magnetic, p = 1 for electric)

L is the multipolarity of the excitation

J^{π} are the spin and parity of the intermediate state reached.

ℓ is the orbital angular momentum of the emitted neutron

$J_{A-1}^{\pi_{A-1}}$ are the spin and parity of the excited state in the residual nucleus.

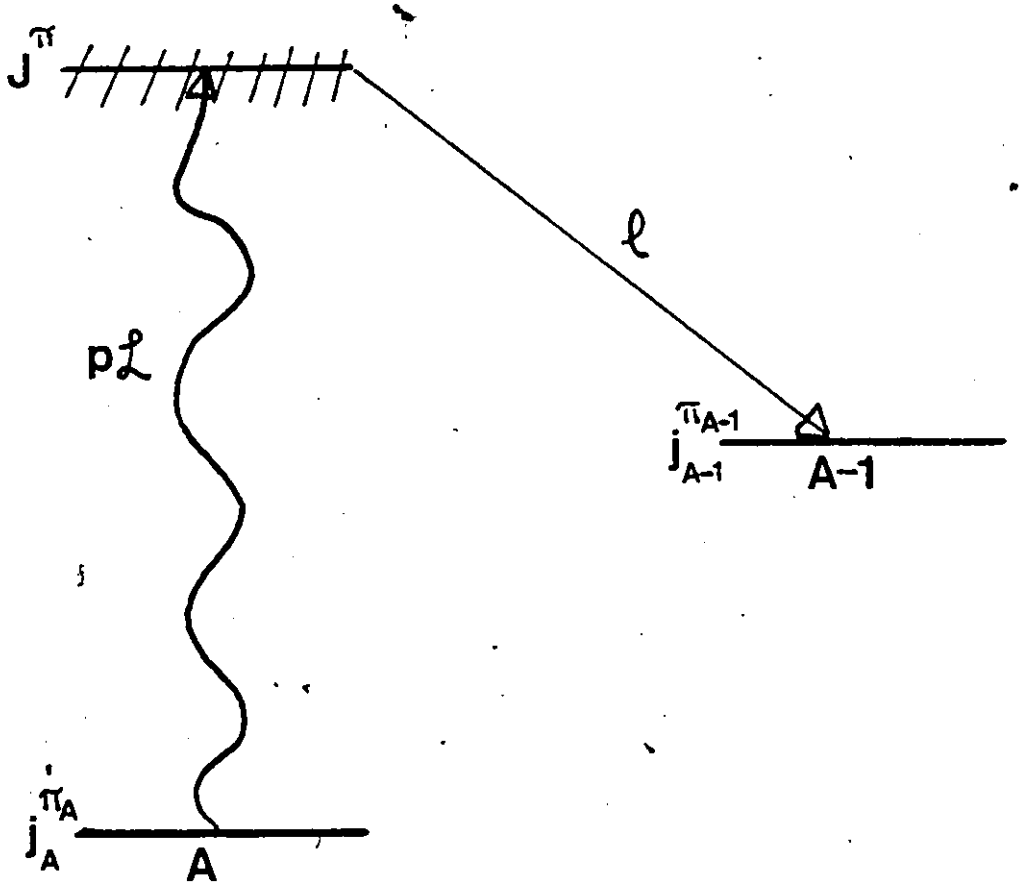

Figure 2.4 Schematic Diagram for Photoneutron Angular Momentum Considerations

We also know the spin and parity of the neutron to be $1/2^+$.

Now define a decay channel spin by

$$\vec{S} = \vec{J}_{neut} + \vec{J}_{A-1} \tag{2.5.1}$$

so that

$$\vec{S} + \vec{\ell} = \vec{J} \tag{2.5.2}$$

One finds the restrictions on J^π, ℓ and S are:

$$|j_A - L| \leq J \leq j_A + L \tag{2.5.3}$$

$$\pi = \pi_A(-1)^{p+L+1} \tag{2.5.4}$$

$$|j_{A-1} - \tfrac{1}{2}| \leq S \leq j_{A-1} + \tfrac{1}{2} \tag{2.5.5}$$

$$|J - S| \leq \ell \leq J + S \tag{2.5.6}$$

and ℓ must be odd if $\pi \neq \pi_{A-1}$

ℓ must be even if $\pi = \pi_{A-1}$

If one assumes incident E1 photon multipolarity (the validity of this assumption is discussed later in this section) the angular

distributions of emitted photoneutrons may not give a clear indication of level spins and parities. This is because unlike the even-even nucleus case (where the excited state is clearly 1^-) the odd-even target nuclei discussed here may, if many resonances are averaged over, excite 3 different spins. Considering the cases of ^{181}Ta, the target nucleus has a spin of $7/2^+$, thus an E1 excitation may produce $\frac{5}{2} \leq J \leq \frac{9}{2}$. Then, following decay, any state with spin $2 \leq J_{A-1} \leq 5$, and negative parity may be populated by emission of s-wave neutrons. It would seem more likely that ^{205}Tl, with its reduced level density may yield excitation of one spin and parity in the target nucleus. As seen in Chapter 4 this seems to be the case.

The value of the assumption of E1 excitation is born out by two facts. Firstly, a search for multipole mixing at this facility (Ba 81) has yielded E2/E1 ratios of typically under 5% over a wide energy range. Secondly, Holt et al (Ho 79) showed in a high resolution study of the (γ,n) reaction on lead targets that the dominant cross sections were E1 in nature.

2.6 Gamma Ray Strength Functions

In order to consider the variation of the photoneutron cross sections with photon energy it is useful to introduce the concept of a gamma ray strength function.

Consider we have a photon with energy spread Δ striking a target nucleus and causing excitation from the ground state J_0 to energy E_γ. Consider now we have a series of resonances around E_γ each with total width Γ_r, where the average value of Γ_r is much less than the average level spacing D. Then the single level Breit-Wigner formula holds, and we may write the total cross section for photoexcitation from the ground state spin J_0 of levels of spin J as

$$\sigma_\gamma^J(E) = \sum_r \frac{g_J \pi}{k^2} \frac{\Gamma_{\gamma r} \Gamma_r}{(E - Er)^2 + \Gamma_r^2/4} \qquad (2.6.1)$$

where g_J = statistical factor

k = photon wavenumber

$\Gamma_{\gamma r}$ = partial γ ray radiative width for transition to spin J state

Γ_r = total radiative width of spin J level

E_r = resonance energy

and the sum extends over all resonances.

Now the average cross section over the entire energy range may be written

$$\langle \sigma_\gamma^J(E) \rangle = \frac{1}{\Delta} \int_{E-\Delta/2}^{E+\Delta/2} \sigma_\gamma^J(E) dE \qquad (2.6.2)$$

or

$$\langle \sigma_\gamma^J(E) \rangle = \frac{1}{\Delta} \sum_r A_r \qquad (2.6.3)$$

where

$$A_r = \pi \, \sigma_{or} \, \Gamma_r / 2 \qquad (2.6.4)$$

with

σ_{or} = Peak resonance cross section

$$= \frac{4 \, g_J}{k^2} \pi \, \Gamma_\gamma / \Gamma_r$$

i.e. A_r is the area of a specific resonance (Se 76). The number of terms in the sum is clearly $N = \Delta/D$

So

$$\sum_r A_r = N \, \overline{A}_r \qquad (2.6.5)$$

$$= \frac{\Delta}{D} \cdot \frac{\pi}{2} \cdot \frac{4 \, g_J \pi}{k^2} \cdot \frac{\langle \Gamma_\gamma \rangle}{\Gamma_r} \cdot \Gamma_r$$

or

$$\langle \sigma_\gamma^J(E) \rangle = \frac{2\, g_J \pi^2}{k^2} \left\langle \frac{\Gamma_r}{D} \right\rangle \tag{2.6.6}$$

The dimensionless quantity $\left\langle \frac{\Gamma_\gamma}{D} \right\rangle$ is often called the strength function.

Now to find the total average radiative absorption cross section, we sum over all J

$$\langle \sigma_\gamma(E) \rangle = \sum_J \langle \sigma_\gamma^J(E) \rangle$$

$$= \frac{\pi^2}{k^2} \sum_J 2g_J \left\langle \frac{\Gamma_\gamma^J}{D_J} \right\rangle \tag{2.6.7}$$

Assuming the strength function to be independent of J (see Pr 62) and using

$$g = \sum_J 2g_J = \sum_{J=J_0-\lambda}^{J_0+\lambda} \frac{2J+1}{2J_0+1} = 2\lambda + 1 \tag{2.6.8}$$

where λ = photon multipolarity

then

$$\langle \sigma_\gamma(E) \rangle = (2\lambda + 1)\frac{\pi^2}{k^2}\left\langle \frac{\Gamma_\gamma}{D} \right\rangle \qquad (2.6.9)$$

As previously discussed, for heavy nuclei at γ ray energies up to a few MeV above the neutron emission threshold, the photoneutron reaction is the only one of any consequence. Alternately one may write $\Gamma_n \gg \Gamma_\gamma$ and so $\sigma_\gamma(E) = \sigma_{\gamma n}(E)$.

A compilation of strength functions may be found in the work of Bartholomew et al (Ba 73). In this work the energy dependance of Γ_γ is removed from our strength function via:

$$f_{xL} = \left\langle \frac{\Gamma_\gamma}{D} \right\rangle \frac{1}{E^{2\lambda + 1}} \qquad (2.6.10)$$

(this energy dependance removal is equivalent to the removal of the neutron penetrability when determining reduced widths, as discussed in the next section).

Now if dipole dominance is assumed, Bartholomew shows

$$f_{xL} = \frac{26 \times 10^{-8}\ \sigma_{\gamma n}(E_\gamma)}{g\ E_\gamma^3} \quad (\text{Mev}^{-3}) \qquad (2.6.11)$$

where $\sigma_{\gamma n}$ is in millibarns

and E_γ is in Mev.

So now with g = 3 (i.e. dipole dominance)

$$\bar{f}_{xL} = 8.67 \times 10^{-8} \frac{\langle \sigma_{\gamma n}(E_\gamma) \rangle}{E_\gamma^3} \quad (\text{Mev}^{-3}) \qquad (2.6.12)$$

As in previous sections one would expect the derivations of the strength function to hold where the density of states is higher, i.e. more so in tantalum than in thallium.

2.7 Transmission Coefficients and Reduced Widths

In order to examine the nature of photonuclear reactions more closely it is necessary to introduce the concepts of transmission coefficients, penetrabilities and reduced widths. These parameters can be used to examine such features as whether the photoneutron reaction proceeds via direct, semi-direct or compound reaction, or may contain some spin information concerning the energy levels in the residual nucleus.

We begin by making similar assumptions to those in the previous section, but now we require knowledge of the cross section for decay via a neutron of angular momentum ℓ. Proceeding as before, we write the single level Breit-Wigner formula

$$\sigma_{c\ell}^{J} = \frac{\pi}{k^2}(2\ell + 1) \frac{\Gamma_{n\ell}^{J} \Gamma_r}{(E - E_0)^2 + \Gamma_r^2/4} \qquad (2.7.1)$$

where now

$$k^2 = 2mE/h^2$$

$\Gamma_{n\ell}$ = the partial neutron width for orbital angular momentum ℓ.

Again if $\Gamma^J_{n\ell} << D^J$, the average may be taken, yielding

$$\langle \sigma^J_{c\ell} \rangle = \frac{\pi}{k^2}(2\ell + 1)\, 2\pi \frac{\langle \Gamma^J_{n\ell} \rangle}{\langle D^J \rangle} \qquad (2.7.2)$$

We now define the transmission coefficient for decay of the compound nucleus by

$$T_\ell(E) = 2\pi \frac{\langle \Gamma^J_{n\ell} \rangle}{\langle D^J \rangle} \qquad (2.7.3)$$

so

$$\langle \sigma^J_{c\ell} \rangle = \frac{\pi}{k^2}(2\ell + 1) T_\ell(E) \qquad (2.7.4)$$

Where it has been assumed here, as is normally done (Pr 62), that T_ℓ is a function of ℓ and E and not J.

Usually the average width in the term in eqn (2.7.3) above is separated into a neutron strength function S_ℓ and a penetrability P_ℓ, in a manner analogous to the gamma ray case from the preceeding

section. One may write,

$$\langle \Gamma^J_{n\ell} \rangle = 2\, S_\ell P_\ell \langle D_J \rangle \qquad (2.7.5)$$

Insertion into eqn (2.7.4) gives:

$$T_\ell = 4\pi\, S_\ell P_\ell \qquad (2.7.6)$$

and

$$\langle \sigma^J_{n\ell} \rangle = \frac{\pi}{k^2}(2\ell + 1)(4\pi\, S_\ell P_\ell) \qquad (2.7.7)$$

The penetrability term is often removed from the individual intensities, and the quantity remaining is labelled the reduced width. It is the distribution of these reduced widths which are the quantities generated by the various theories on the nature of photoneutron reactions. Clearly the removal of P_ℓ depends upon a knowledge of the orbital angular mementum of the emitted photoneutron. As has been pointed out, in general, for the experiments conducted in this thesis this is not generally the case.

One can easily show that (Pr 62), for neutrons in a square well,

$$P_0 = \rho$$

$$P_1 = \rho^3/(\rho^2 + 1)$$

$$P_2 = \rho^5/(\rho^4 + 3\rho^2 + 9)$$

$$P_3 = \rho^7/(\rho^6 + 6\rho^4 + 45\rho^2 + 225)$$

where $\rho = k\ a$

$$= \sqrt{2m\bar{E}}\ \frac{a}{\hbar}$$

where a = well radius.

An examination of the work of Auerbach and Perey (Au 62) shows that the transmission coefficients, for energies 2 Mev, are dominated by s-wave neutron emission. Since $P_\ell \alpha T_\ell$, it was decided that for the analysis carried out in Chapter 4 division of the partial photoneutron cross section by $\sqrt{E}$ would yield a first order approximation to the reduced width.

2.8 The Distribution of Reduced Widths

Once the reduced widths have been evaluated, their distribution at any one particular γ ray energy yields clues as to whether the reaction proceeds via direct or compound mechanisms. We begin by a discussion of the two processes.

A direct reaction proceeds without the formation of a compound nucleus. It proceeds very much faster than compound nuclear formation, with correspondingly greater resonance widths. This reaction is a one-step process in which the incident photon interacts directly with the scattered neutron.

A compound reaction is one in which, after a few internal collisions the neutron energy is sufficiently below that of the Fermi level that it does not have enough energy to escape. The nucleus "loses memory" of its origin, save that the nucleus has had its energy, angular momentum and parity altered, and after many rearrangements of nuclear configurations an exit channel occurs and a decay takes place. Thus, the probability of decay is assumed to be independent of the mode of formation. This is clearly a multistep process.

One property which may be used to differentiate between the two processes is the distribution of reduced widths. Hughes and Harvey (Hu 55) determined empirically that the distribution of reduced neutron widths ($\Gamma^0_{\lambda n} = \Gamma_{\lambda n}/(E_\lambda)^{\frac{1}{2}}$) has the form

$$P(x)dx = (2\sqrt{\pi})^{-1}\left(\frac{x}{2}\right)^{-\frac{1}{2}}\exp\left(-\frac{x}{2}\right)dx \qquad (2.8.1)$$

where

$$x = \Gamma^0_n/\langle\Gamma^0_n\rangle_{av}$$

where $\langle \Gamma_n^0 \rangle_{av}$ is the average reduced neutron width (Fi 70b). This distribution was predicted theoretically by Brink (Br 55) who suggested that due to the high density of states at any particular excitation energy, the central limit theorem of statistics would yield a Gaussian distribution of reduced width amplitudes, γ, with mean zero and variance γ^2 given by,

$$P(\gamma)d\gamma = (2\pi\langle\gamma^2\rangle_{av})^{-\frac{1}{2}}\exp(-\gamma^2/2\langle\gamma^2\rangle_{av})d\gamma \qquad (2.8.2)$$

so that the distribution of reduced widths becomes

$$P(\gamma^2)d\gamma^2 = (2\pi\gamma^2\langle\gamma^2\rangle_{av})^{-\frac{1}{2}}\exp(-\gamma^2/2\langle\gamma^2\rangle_{av})d\gamma^2 \qquad (2.8.3)$$

Equation (2.8.3) was derived independently by Porter and Thomas (Po 56). The authors have used arguments based upon the physical properties of the overlap integral in the definition of the reduced width amplitude.

The Porter-Thomas-Brink distributions are a special case (ν=1) of the chi-squared function with ν degrees of freedom:

$$\rho_\nu(x)dx = \overline{\Gamma}^{-1}(\nu/2)(\nu/2\langle x\rangle)^{\nu/2}\, x^{(\nu-2)/2}e^{-\nu x/2\langle x\rangle}dx \qquad (2.8.4)$$

where $\overline{\Gamma}$ is the incomplete gamma function.

The parameter ν is seen to correspond to the number of channels the reactions may proceed through. By computing $\rho_\nu(x)$ as a function of x for different values of ν it can easily be shown that the distribution narrows as the number of degrees of freedom increases.

Reactions which proceed by direct mechanisms should be expected to yield reduced widths which are narrowly distributed, since the reaction takes place through the influence of an average potential which should be approximately the same for all states. Hence, if an estimate of ν is obtained and found to be large, it is indicative of a direct (or semidirect) reaction, with a large number of excited states available for photon absorption. Conversely a smaller estimate of ν indicates the dominance of one excited state resonance.

Relating to this thesis, the number of degrees of freedom should be expected to be higher for tantalum than for thallium, based upon the higher density of states available for photoexcitation. The number of degrees of freedom should also be expected to increase with increasing photon energy in each nucleus.

As an estimate of the number of degrees of freedom we use the work of Lyclama et al (Ly 69). An estimate of ν was derived here having only a 1% bias, as

$$\langle \nu \rangle \doteq \left(\frac{n-3}{n}\right)\left(\frac{2}{\sigma^2}\right) - \frac{2}{n} \qquad (2.8.5)$$

$$\langle \sigma^2 \rangle = \frac{1}{n} \sum_i (x - \bar{x})^2 \qquad (2.8.6)$$

and

$$\bar{x} = \frac{1}{n} \sum_i x_i = 1$$

where x_i are the reduced widths normalized to a mean of 1.

n is the number of reduced widths in the sample.

CHAPTER THREE

3.0 THE EXPERIMENTAL SYSTEM

The (γ,n) facility at the McMaster Nuclear Reactor has been described previously (Mc 77). A brief discussion of the pertinent features for the particular experiments performed in this study is presented below.

3.1 The Beam Port Facility and Gamma Ray Sources

The McMaster Nuclear Reactor is a 5 Megawatt rated light-water cooled and moderated facility, in which the (93%) enriched uranium fuel elements are housed in a rectangular 9 x 6 grid.

The (γ,n) facility is located at Beam Port Number One of the reactor. The gamma ray sources for this experiment were placed, while in use, in a specially-built housing at position 1B of the fuel element grid. At position 1B, the sources are exposed to a thermal neutron flux of approximately 10^{13}n/cm^2/sec. Following neutron capture, the prompt γ ray beam was extracted and collimated by a series of stepped wood, concrete lead and wax plugs as shown in Fig. (3.1) to produce a 2.5 cm diameter beam at the external target position.

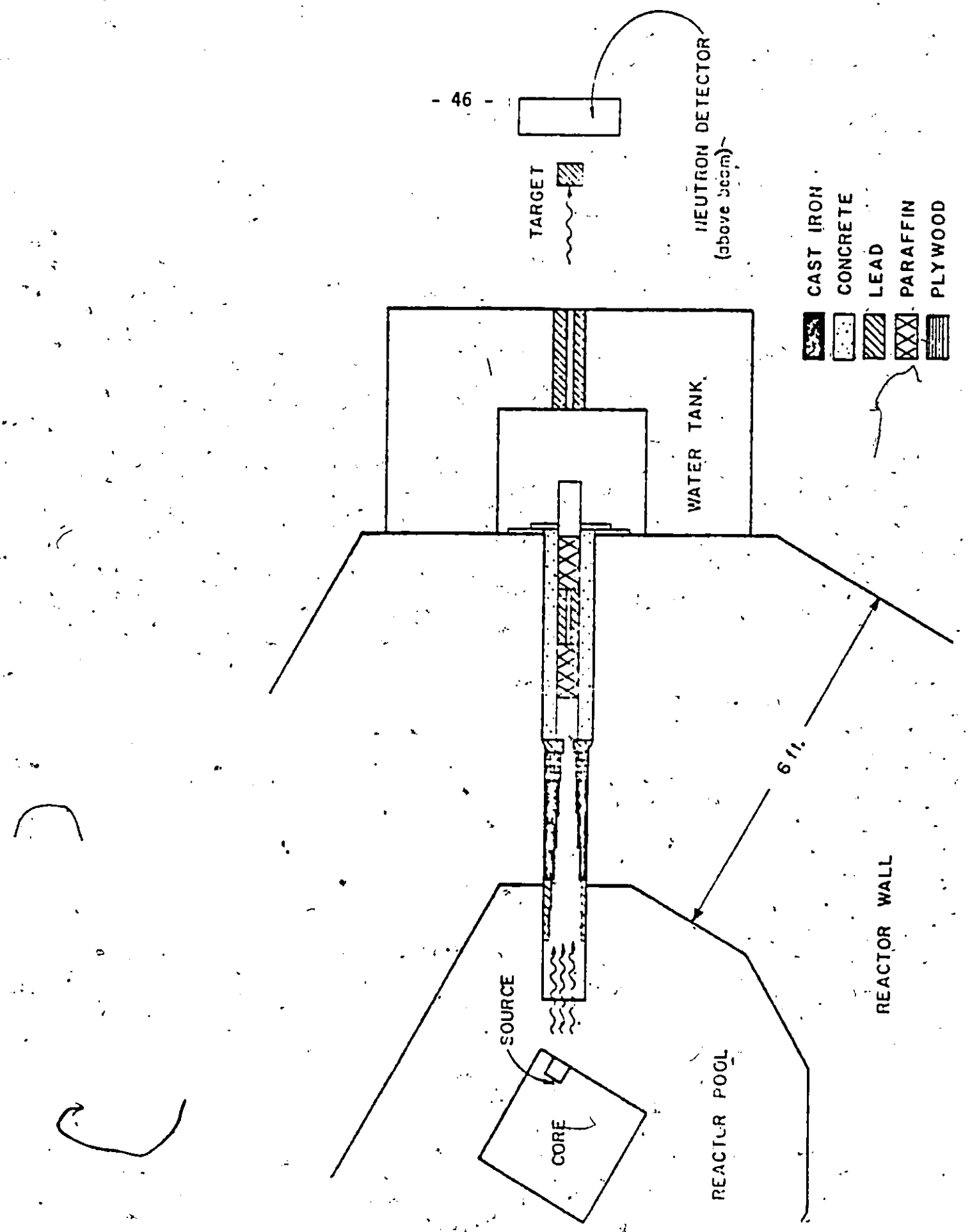

Figure 3.1 The (γ,n) Beam Port Facility at the McMaster Nuclear Reactor

For this experiment, five different γ ray sources were used. Figure (3.2) gives the physical dimensions of all sources, while Table (3.1) lists the physical make up of the individual targets and containers. The sources could be interchanged during weekly reactor shutdowns, and while not in use all sources were stored under approximately 15' of water to afford biological protection from the long-lived radioactivity built up during in-core use.

The measurement of both the relative and absolute γ ray fluxes from each source will be discussed later.

3.2 The Targets

The photoneutron targets used in the experiments consisted of:

a) Thallium: Natural thallium (70.5% ^{205}Tl; 29.5% ^{203}Tl) was melted and formed by use of a cubic mold and then machined to form a 2.54 cm cube.

b) Tantalum: Four sheets of natural Ta, each measuring 3.81 cm x 2.81 cm x 0.64 cm were stacked one atop the other to produce an effective 3.81 cm x 3.81 cm x 2.54 cm cube.

In order to position the targets directly in the γ ray beam, any or all of three methods could be used:

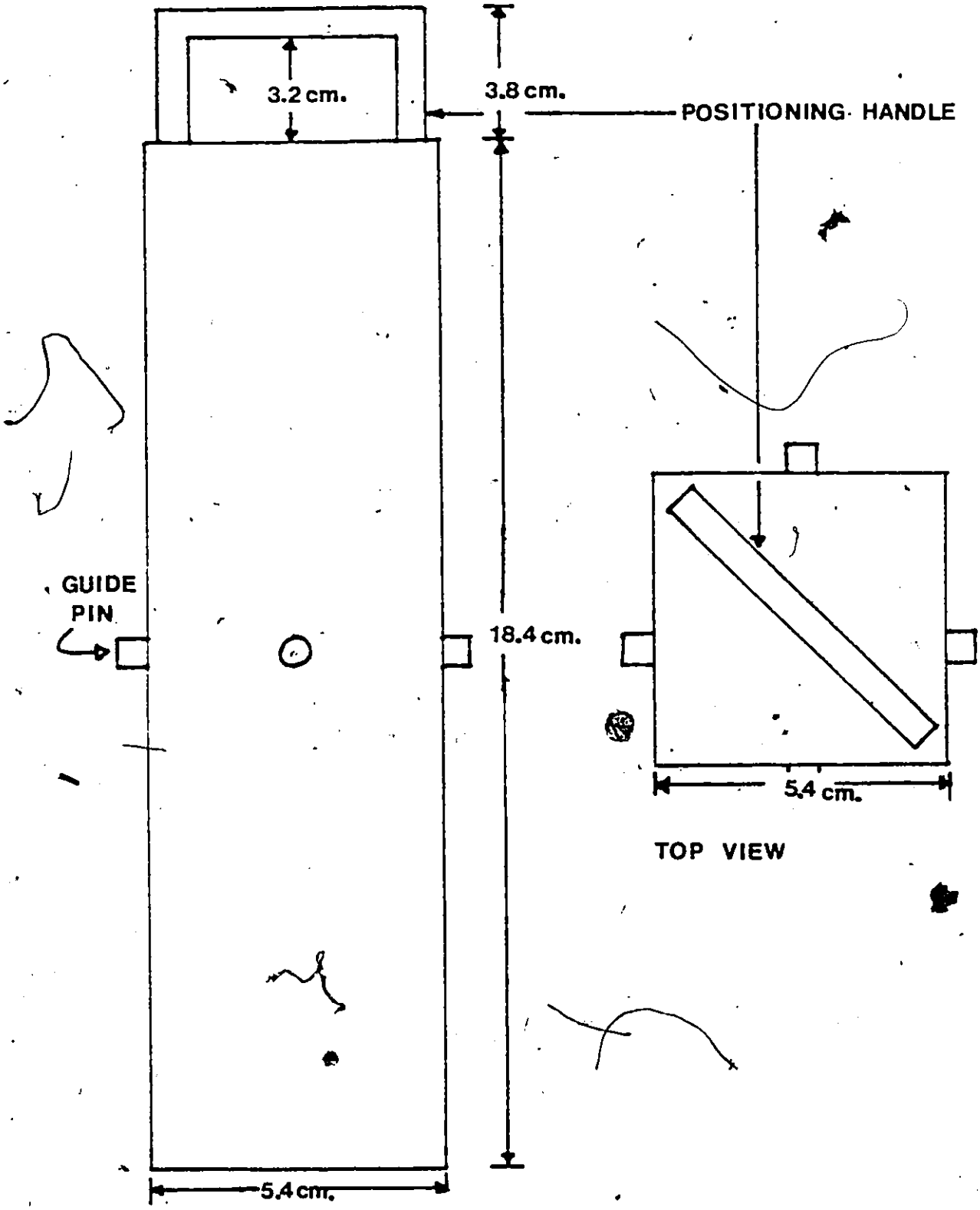

Figure 3.2 Physical Dimensions of Neutron Capture Gamma Ray Source Aluminum Container

TABLE 3.1

PHYSICAL MAKE-UP OF GAMMA RAY SOURCES

SOURCE	MAKE-UP
Aluminum	Solid (17.6 cm x 5.1 cm x 5.1 cm) slab
Iron	Solid (17.6 cm x 5.1 cm x 5.1 cm) slab in Aℓ container
Copper	Copper Filings in Aℓ container
Nickel	4 rods (17.6 cm x 2.5 cm diameter) in Aℓ container
Chromium	4 rods (16.6 cm x 2.5 cm diameter) in Aℓ container

1) The use of an AEP 215A γ ray monitor, in the "high range" mode allowed accurate determination of the beam position simply by observing the position corresponding to the maximum measured dose rate (typically > 10 R/hr).
2) A photograph of the beam was taken using Kodak AA industrial X ray film contained in an aluminum containing cassette which was placed in a relocatable position in front of the target. After developing, the film was replaced on the front face of the cassette which was repositioned. The 2.5 cm diameter darkened area on the film clearly defined the beam position.
3) Marks were made on the reactor wall face above and to the side of the target position as determined by both preceding methods, and could be used as a rough target positioning guide.

Target positioning was checked approximately twice weekly during the course of the experiments.

3.3 The Neutron Detector and Associated Electronics

The photoneutrons produced in the experiments carried out in this thesis were detected by means of a ^{3}He-filled gridded ionization

chamber (FNS-1, Seforad Applied Radiation Ltd. of Emek Hayarden, Israel). Like all other ^3He detectors, neutrons are detected by means of the reaction

$$n + {}^3He \rightarrow p + {}^3H + Q \qquad (3.3.1)$$

where Q = 763.8 ± 0.1 Kev (Sa 64). This positive Q value is small enough to allow excellent energy resolution over a wide energy range, and as has already been pointed out this allows for resolutions of approximately 12 Kev for thermal neutrons, and 27 Kev for 1 Mev neutrons for the particular detector used in this thesis. The theory behind ionization chambers is well documented (eg Ba 60). Of particular interest is the use of the Frisch Grid (La 60) to eliminate the position sensitive pulse height effect associated with charge collection in conventional ionization chambers. Figure (3.3) gives the physical parameters of the detector. In the next chapter the detector efficiency as a function of incident neutron energy will be discussed in relation to the determination of the photoneutron cross sections. Much more detail on this particular detector may be found elsewhere (Cu 71, Mc 77).

Depending on whether energy spectra or angular distribution measurements of the emitted photoneutrons were to be performed, the ^3He detector was placed in one of two positions.

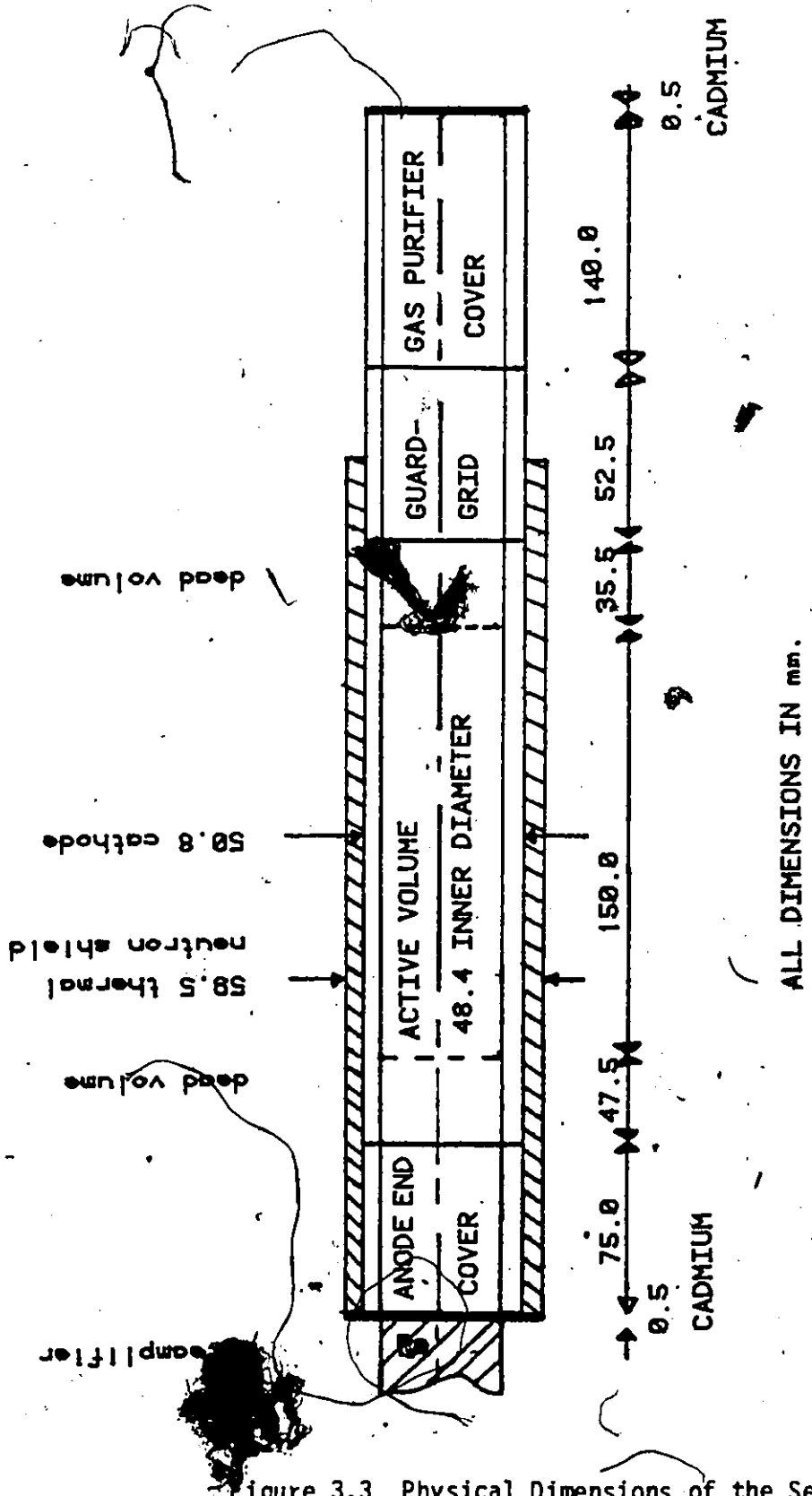

Figure 3.3 Physical Dimensions of the Seforad FNS - 1 ^{3}He Ionization Chamber

For energy spectrum measurements the detector was placed as close as possible to the photoneutron target, without directly intersecting the photon beam itself, in order to maximize the count rate. The detector was thus positioned perpendicular to the beam direction, and had its outer wall approximately 0.5 cm from the photoneutron target. Because of high efficiency for low energy neutrons, all photoneutron spectra showed a large thermal energy peak. While this peak (occurring at $E_n \sim 0$) was valuable for energy calibration the large epithermal continuum above it tended to obscure many low energy photoneutron groups. To counteract this effect, the detector was placed in a large (80 cm x 25 cm x 15 cm) BORAL (Boron-Carbide-Aluminum, $\sigma_{th} \approx 50$ b) containing box. The box completely surrounded the detector save for two 6 cm x 6 cm holes allowing the γ ray beam to enter, strike the target and egress.

For the angular distribution measurements the detector was fastened to a rotating stand which maintained its central anode wire at 12.7 cm from and perpendicular to the photon beam as in the manner which has been described by Barkman (Ba 81). In this manner the detector was free to rotate through azimuthal angles from 0° to 180° with respect to the beam. For the experiments carried out in this thesis, the detector angle was changed in 30° steps from 30° to 150°. Angles less than 30° or greater than 150° could not be attained since the detector would then intersect the photon beam itself.

In both cases, the Boral box and the stand were weighted down with lead weights and rested on foam cushioning in order to eliminate

microphonic pick up by the detector which again would tend to degrade resolution.

The electronics associated with the ^3He spectrometer are shown in Fig. (3.4). The detector anode was maintained at a constant +3000 volts by the Power Designs model AEC 1000 power supply. A voltage divider within the preamp (SR 101) kept the grid at +850 Volts, thus aleviating the need for a separate power supply. The preamp itself consisted of two stages, the first of which integrated the collected charge from the ionizing protons and tritons. The second stage consisted of a gain of ten voltage amplifier to make the output signal comparable in magnitude to that of a Ge(Li) detector, enabling conventional spectroscopy amplifiers to be used.

The signal from the preamp was then fed to an ORTEC MODEL 572 shaping amplifier. A 6 μsec shaping time constant was chosen since this afforded the optimum resolution over a wide energy range from all the available shaping times. The shorter time constants (3 μsec or less) proved unsuitable because of incomplete charge collection at higher neutron energies - corresponding to longer ionization track lengths. The longer time constant (10 μsec) descreased the energy resolution because of noise on the signal. The main feature of the ORTEC 572 amplifier which made it attractive for photoneutron spectroscopy was the pile up rejection option. Gamma rays may scatter from the target and produce photoelectrons from the chamber walls creating small output pulses which may randomly add to the "real"

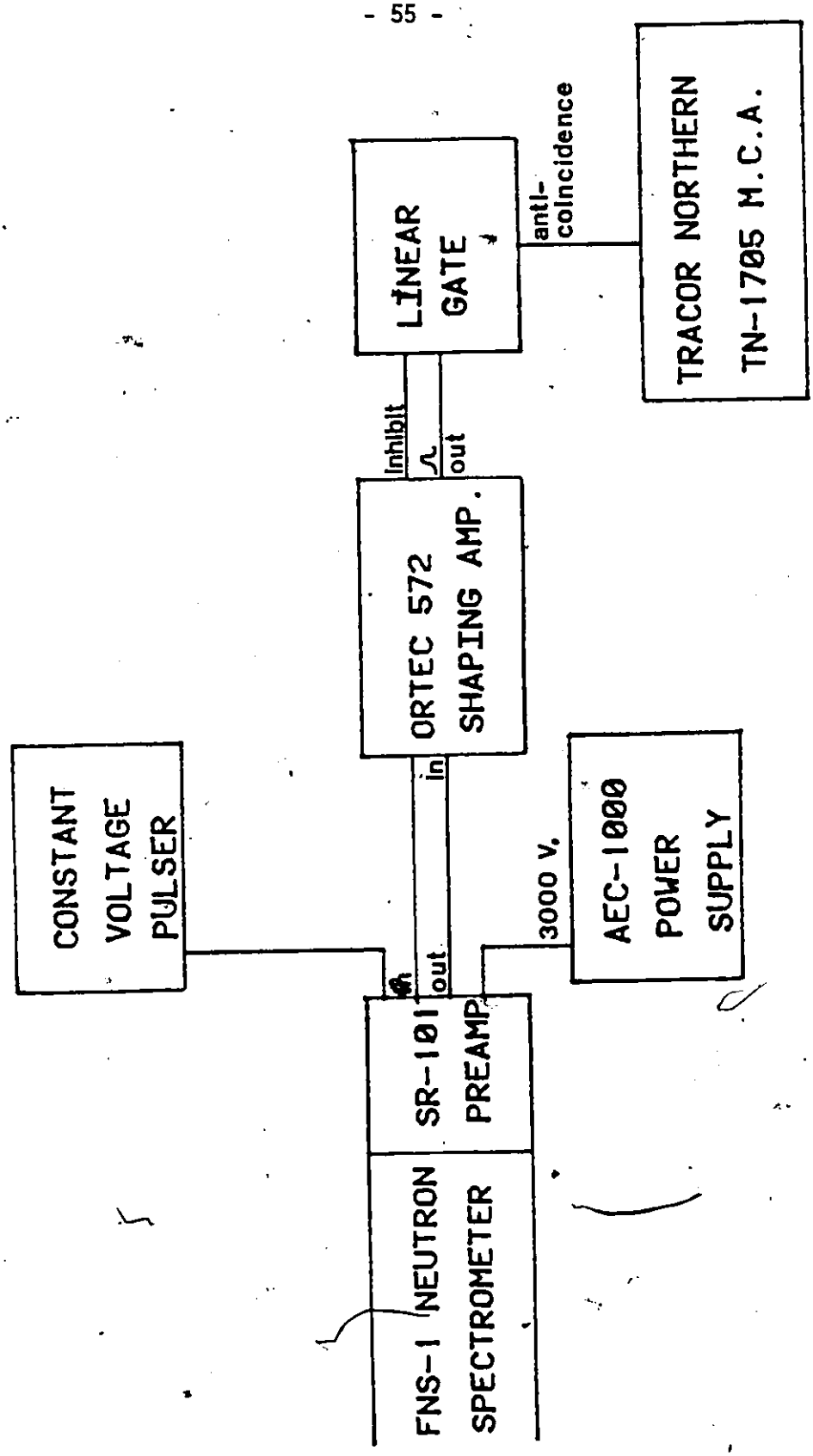

Figure 3.4 Electronics Associated with ^3He Spectrometer

neutron pulses degrading resolution. The amplifier however may be used to reject such pileup events. An output inhibit pulse of duration 6 x [shaping time] is created whenever a pileup is noted. By feeding the output and inhibit pulses to the input and gate, respectively, of a linear gate (CANBERRA MODEL 1451) in the anticoincide mode, pileup rejection was implemented.

A stabilization pulser was also fed to the preamplifier, creating a high energy signal of known constant voltage. This signal proved useful not only for neutron energy calibration and gain shift determinations but also for analysis of gamma ray pile-up, if any occurred.

The gate output was fed to the input of a TRACOR NORTHERN TN 1705 multichannel analyzer. Data were collected in 1024 channel spectra. Following data acquisition, data were transferred to a PDP 15 computer. Data files were then created in a NOVA 2 minicomputer (Data General) where all analysis took place.

3.4 The Beam Monitor

During reactor operation, while the total integrated neutron flux is held constant the localized flux at any one position within the reactor fuel grid may vary considerably as fuel burn-up and control rod adjustments take place. In addition, in the case of the McMaster Nuclear Reactor, any individual fuel element may be changed on a weekly

basis resulting in a new localized flux pattern. For these reasons, the γ ray flux incident upon the target, which of course represents the thermal neutron flux at the source, is a dynamic function of time.

Thus when performing the angular distribution measurements any photoneutron cross section measurement required an accurate knowledge of the incident γ ray flux. This was accomplished by means of a beam monitor and the associated electronics shown in Fig. (3.5).

The incident γ rays were allowed to Compton scatter from the target itself into a 7.62 cm x 7.62 cm NaI(Tl) detector, which was contained in a form-fitting lead shield.

The choice of the window around 511 Kev for the SCA allowed periodic checking of gain shifts with the use of a calibrated ^{22}Na γ ray source.

The form-fitting lead shield served to eliminate most, but not all of the background radiation from the reactor. The major source of the reactor background γ radiation was seen to be the 1.29 Mev γ ray from the decay of ^{41}Ar, which is built up via thermal neutron capture in ^{40}Ar. Such γ rays could Compton scatter from the lead shielding and enter the detector window. Because of the relatively short half-life ($\tau_{\frac{1}{2}}$ = 1.83 hrs) of ^{41}Ar, it was deemed advisable never to start an angular distribution measurement until the concentration of ^{41}Ar had reached equilibrium (~ 4 hrs after reactor startup).

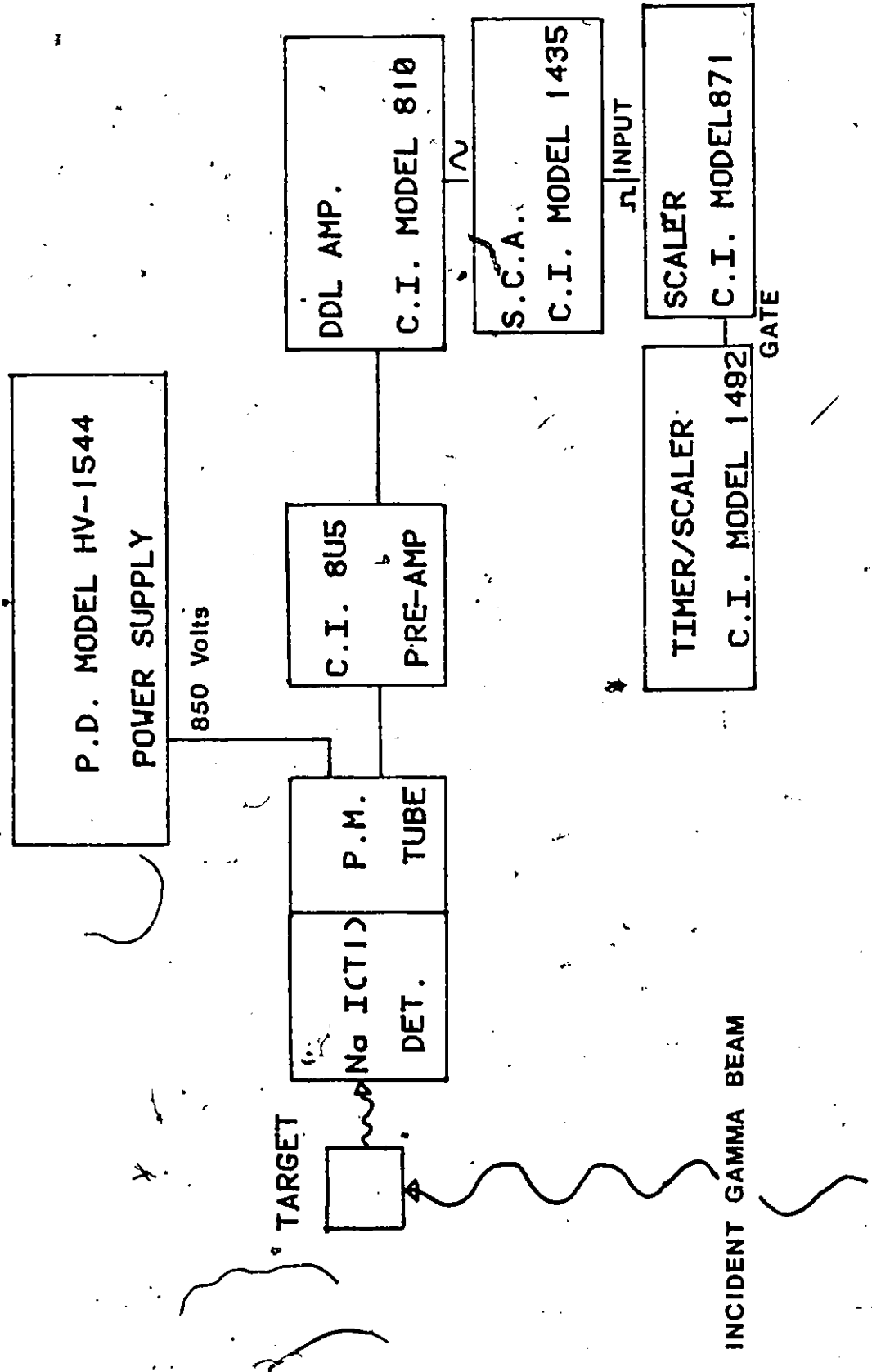

Figure 3.5 Electronics Associated with Beam Monitor

The background rate was measured periodically, with the target removed, and subtracted from the monitor rate. It was noted that the background rate was never more than 5% of the monitor rate.

While it might have been desirable to also monitor the scattered beam for energy spectrum measurements this was not carried out. The reason behind this was that, for different (γ,n) targets, a scatterer (probably Carbon) would have to placed before the target. Doing this was seen to result in degraded resolution resulting from beam scattering. However, all the experiments performed in this thesis, were carried out at least twice, and no statistically significant variations in neutron production rates were observed. In addition, when the beam monitor rates for angular distributions measurements (typically 70,000 sec. for any one angle) were integrated over a week (the typical time for any energy spectrum measurement) they were found to be constant to high accuracy.

3.5 Absolute Photon Flux Measurement

In order to determine accurately the photoneutron cross sections it was necessary to measure the γ ray flux incident upon the target. This proved to be a non-trivial procedure for many reasons. Firstly, with the reactor operating at full power the incident γ ray intensities were so great that any conventional detector placed in the beam would be rendered completely ineffective due to dead time losses. Secondly, at lower power it was found that conventional NaI(Tl) detectors, because of poor resolution and interference from single and

double escape peaks proved inadequate in producing accurate results. Finally, the use of intrinsic Ge detectors at low power while affording superior energy resolution was not considered feasible because of the dearth of information on the detector cross section at high energies.

To circumvent the problems a coincidence pair spectrometer was constructed. Figure (3.6) shows the spectrometer and the associated electronics. The principle behind such a spectrometer is well-established (eg Ro 74). Briefly, a γ ray with energy $E_\gamma > 1.022$ Mev may create a positron-electron pair in the centre crystal (A). Following positron annihilation, two 511 Kev γ rays are produced at an angle 180° with respect to each other and may be detected in the side crystals (B and C). If these two signals are detected within a 20 n sec resolving time, they may be used to gate the output signal from the centre detector. Clearly such time correlated events produce only signals with energy (E_γ - 1.022 Mev) at the analyzer and discriminate against all full energy, single escape and Compton scattered photons. The resulting spectrum proves much easier to analyze.

To make such a detector useful, it was first necessary to calibrate the spectrometer (both relatively and absolutely) as a function of incident γ ray energy.

(i) Relative Energy Calibration of the Spectrometer

Following thermal neutron capture, the prompt γ ray energy spectrum from any one element is well documented in the literature (for example Ra 67).

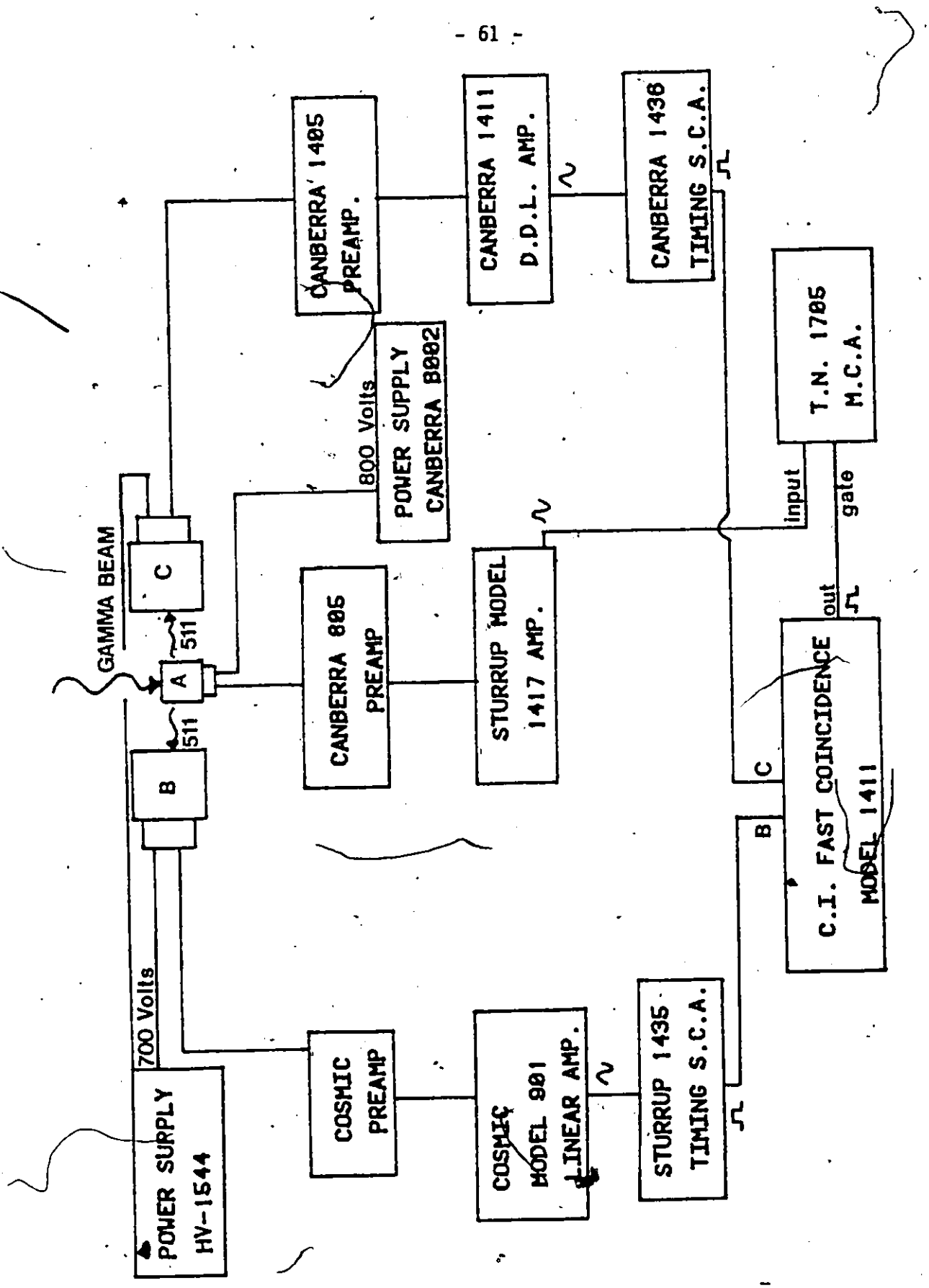

Figure 3.6 Pair Spectrometer and Associated Electronics

Thus in order to perform a relative energy calibration of the pair spectrometer it was decided to subject it to a series of prompt γ ray spectral beams. This was accomplished by irradiating various samples at the McMaster Reactor Tangential Facility (see section 3.6). A 1 cm diameter beam of known spectral components was then produced at the detector face. Three elements which proved useful for analysis were nitrogen (in gaseous form), iron, and beryllium.

The strong intensity peaks from these three sources are listed in Table (3.2). Analysis of the spectra produced from the three gave the relative efficiency of the detector over a range from 3 to 11 Mev.

(ii) Absolute energy Calibration of the spectrometer

A ^{56}Co γ ray source was produced at the McMaster Tandem Accelerator by $^{56}Fe(p,n)^{56}Co$ reaction. This source produces γ rays of energies up to 3.6 Mev as shown in Table 3.3. This source was then placed in the geometry shown in Fig. (4.5). The lead doughnuts give an approximate 2.5 cm beam incident upon the centre crystal, simulating the actual photon beams.

This source was then compared to a ^{56}Co source of known intensity by playing both in a 4π geometry ionization chamber.

Thus the absolute intensity of the source was determined. By consideration of the solid angle in the source-detector geometry, a measurement of absolute spectrometer efficiency at energies up to 3.6

TABLE 3.2

STRONG INTENSITY TRANSISTIONS FROM THERMAL NEUTRON CAPTURE IN N, Be AND Fe

ELEMENT	E_γ*(Mev)	I_γ*(No/100)
Nitrogen	3.531	9.58
	3.675	15.52
	4.508	15.31
	5.287	25.41
	5.294	18.58
	5.532	17.79
	5.560	9.05
	6.321	16.65
	7.300	8.36
	8.309	4.22
	10.828	15.00
Beryllium	2.590	24.00
	3.368	34.20
	3.444	11.80
	6.810	62.50
Iron	5.921	8.29
	6.019	8.08
	7.632	27.19
	7.646	22.14
	9.298	3.08

* All values taken from Ra 67

TABLE 3.3

γ RAYS FROM DECAY OF ^{56}Co

E_γ(Mev)*	I_γ(No/100)*
1.771	15.70
2.015	3.080
2.035	7.890
2.599	16.90
3.010	1.00
3.202	3.040
3.254	7.410
3.273	1.750
3.452	0.875

* All values from Le 78

Mev was determined. By comparison with the relative efficiency curves from the previous section, the spectrometer was absolutely calibrated for all γ ray energies up to 11 Mev.

3.6 The $^{180}Ta(n,\gamma)^{181}Ta$ Experiment

In order to identify positively the energy difference between the long-lived configuration and the ground state of ^{180}Ta, if any, an examination of the neutron capture γ ray spectrum of a 4% enriched ^{180}Ta target was carried out. Here, clearly neutron capture can only occur in the long-lived configuration and the energy difference between $Q\{^{180}Ta(n,\gamma)^{181}Ta\}$ and $Q\{^{181}Ta(\gamma,n)^{180}Ta\}$ represents the excitation energy of this configuration.

The 1 mg sample of tantalum oxide was enclosed in a graphite capsule and placed in the irradiation position of the McMaster Reactor tangential facility. The incident thermal neutron flux density at this position is approximately 2×10^{12} cm^{-2} sec^{-1}. The capture gamma ray spectrum was observed using a triple coincidence pair spectrometer, which consists of an intrinsic germanium detector surrounded by a quadrisected annulus of sodium iodide. Robertson (Ro 72) has given a more detailed account of the experimental arrangement.

Data were collected for three weeks, during which time the gain and zero intercept of pulse processing were stabilized on two reference

peaks. The lower energy reference peak was produced by the 1.275 Mev gamma ray from ^{22}Na in triple coincidence with the time-correlated annihilation radiation arising from the associated positron decay. This radiation was introduced by placing a ^{22}Na source on the face of the cryostat of the detector. The higher energy reference peak was produced by the 4.945 Mev ground state transition in the $^{12}C(n,\gamma)^{13}C$ reaction resulting from neutron capture in the graphite capsule. Upon completion of this experiment, similar procedures were used to observe the spectra produced by a 30 mg sample of natural tantalum and by a 1 mg sample of melamine ($C_6H_8N_{11}$) for comparison and calibration purposes respectively.

CHAPTER FOUR

4.0 DATA ANALYSIS

A typical photoneutron spectrum of the type to be analyzed in this thesis is shown in Fig. (4.1). The spectrum clearly involves a series of peaks arising from discrete transitions to excited states in the residual nucleus (see Chapter 3) superimposed upon an energy variant background continuum. The first step in any data analysis to be carried out was the subtraction of this background. The following section gives brief discussion to the causes of the background, while section (4.2) discusses the methodology behind the subtraction.

4.1 Causes of Background in Photoneutron Spectra

Five of the major factors influencing the background components are given below.

(i) Reactor Thermal Neutron Background

Any experiment performed in a nuclear reactor will have to deal with a significant contribution arising from transmission of thermalized neutrons through the reactor containment walls. For experiments conducted using a ^{3}He neutron detector the effect is

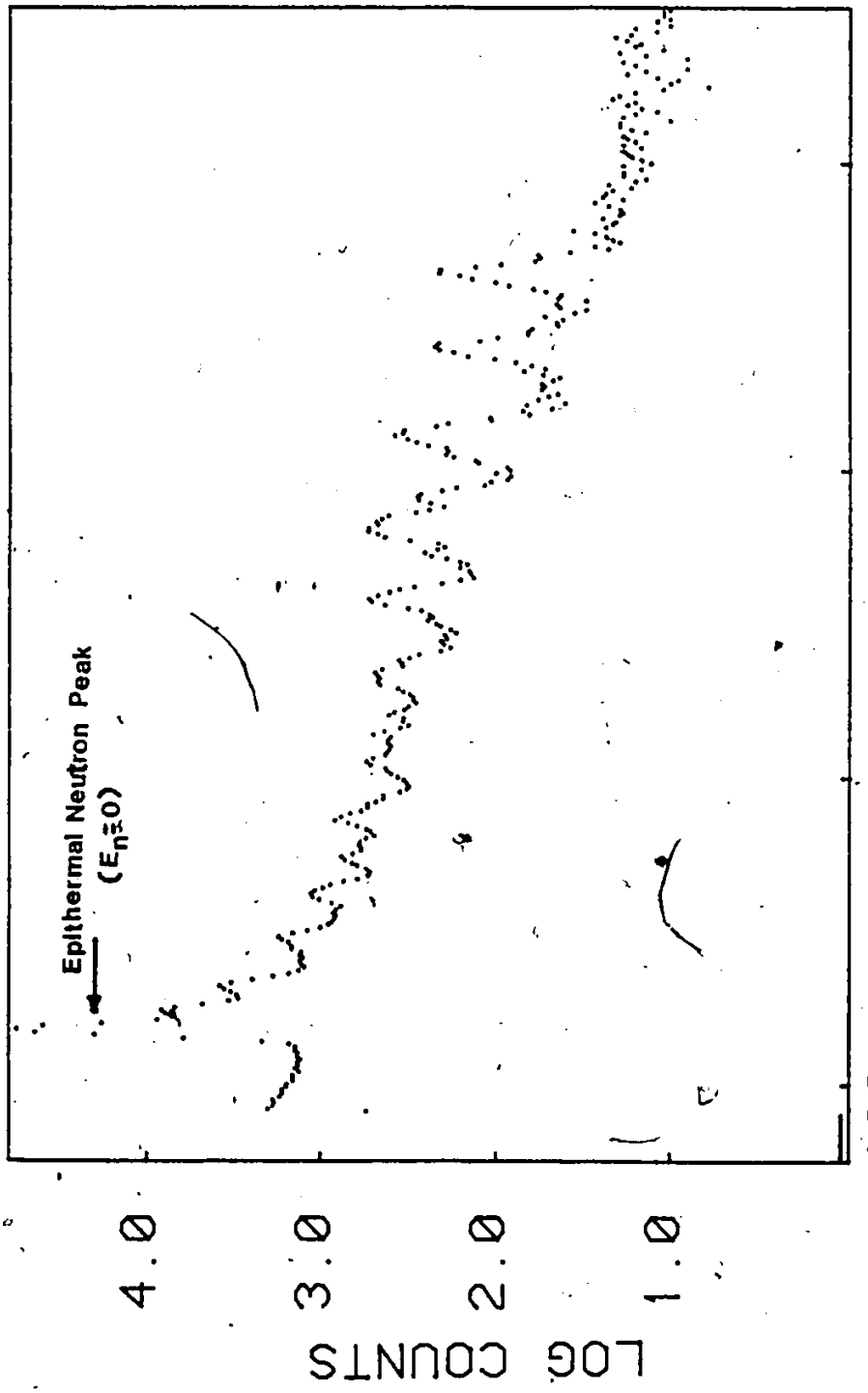

Figure 4.1 Typical Photoneutron Spectrum. The epithermal Neutron Peak and other Features Explained in the Text are Clearly Visible.

particularly noticeable because of the high detector efficiency at lower neutron energies (see sec. 4.6.2). This effect may be modelled by a Gaussian distribution (F.W. H.M. = 12 Kev) around 0 neutron energy, with a higher energy continuum above it due partially to the $\frac{1}{E}$ nature of the reactor neutron spectrum, and partially due to factors discussed below.

(ii) Gamma Ray Scattering

With the ^3He detector placed as close as possible to the photo-neutron target, it was possible for scattered γ rays to strike the chamber walls resulting in emitted photoelectrons which cause low energy pulses at the anode. The effects thus produced included a low energy continuum (extending below zero neutron energy) and a high energy tail on most peaks resulting from pulse pile-up. The latter effect, although somewhat abrogated by the pile-up rejection system was still observable, especially for the low angle angular distribution measurements to be discussed later in this chapter.

(iii) Wall Effect

If the proton (or triton) ionization track lengths extended outside of the active volume of the detector, then an event with a fraction of the total neutron energy would be recorded. Thus for higher energy neutrons there would exist a lower energy continuum below the full energy neutron peak.

(iv) Neutron Elastic Scattering

An examination of the total ^3He neutron cross section (BNL 325) reveals that over the energy range of 0-2 Mev the ^3He $(n,n')^3He$ scattering cross section is greater than the $^3He(n,p)^3H$ cross section. These elastic scatterings result in the neutron losing between 0 and $\frac{3}{4}$ of its original energy with equal probability, so an energy between 0 and $\frac{3}{4}$ En may be recorded. The reaction will result in a contribution to the actual (En $>$ 0) neutron spectrum only if En $> \frac{4}{3}$ Q = 1.018 Mev (here Q = the $^3He(n,p)^3H$ Q-value).

(v) Microphonic Pick-Up

Any sound or other vibrations causing the grid to move with respect to the anode would cause pulses to be recorded at the anode. Despite all efforts to eliminate this, the daily workings of the reactor proved enough to make this effect the major factor in degrading energy resolution. The effect was particularly distressing because of its random nature, the inability to model its spectral form, and the fact that the interference extends throughout the entire neutron energy spectrum.

4.2 Subtraction of Background

The subtraction of the background from a photoneutron spectrum was carried out in any one of three ways, depending on whether the peaks were well-isolated or not, or to some extent on their energy.

If any one single photoneutron peak was well isolated from its neighbours then a first, second or third order least squares fit was made to the contents of the channels on either side of the peak. The background contribution, Bi, to each channel determined from the fit

$$Bi = b_0 + b_1 i + b_2 i^2 (+b_3 i^3) \qquad (4.2.1)$$

could then be subtracted point by point from the original spectrum Y_i, giving the counts in each channel C_i due to the photoneutrons. The value of C_i was set to zero if negative or if $C_i < \sqrt{Y_i}$. This ensured the background was within a standard deviation of the contents of channel i. This method proved operable only for a few peaks - chiefly those strong transistions which rendered themselves available for angular distribution measurements and others near the ground state transition corresponding the highest energy gamma ray in any spectrum.

For most of the spectra, however, the high density of states in the residual nucleus coupled with the multiplicity of possible gamma rays at lower neutron energies resulted in very few isolated peaks superimposed upon a smooth background. The method chosen for background subtraction in these cases consisted of the fitting of background points to a cubic spline function as outlined below.

The first step involved the choosing, by eye, of local minima "knot" points each of which was representative of the background in any

one region of the spectrum. This gave as an approximation to the background at the knot points (channels) I_n, a discrete number of points $B(I_n)$. Next a three-point smooth was applied to these points, producing a new discrete set of data points $B'(I_n)$ as an approximation to the background. Following the smooth a cubic spline fit was made to the points $B'(I_n)$ resulting in an interpolated background function B''_i at all data points in the spectrum, again B''_i could be subtracted from Yi giving Ci. Also as before Ci was set to zero if $Ci < \sqrt{Yi}$.

Special attention was given to very low energy neutron groups where the contribution from the large epi-thermal neutron peak proved bothersome. In these cases a Gaussian was fit to the thermal peak and subsequently subtracted from the entire spectrum before either of the two preceding methods was employed.

4.3 Extraction of Peak Areas and Centroids

For the case of the single isolated well resolved photoneutron peaks as previously mentioned the sum over all C_i (eqn 4.2.1) provided the area with the associated error

$$\sigma^2_{AREA} = \sum_i [Y_i + \sum_{j,k=0}^{3} \sigma^2_{jk} (\frac{\partial Bi}{\partial bj})(\frac{\partial Bi}{\partial Bk})] \qquad (4.3.1)$$

determined from the variance covariance matrix of the fit.

The determination of the centroids associated with these peaks was also a straighforward procedure - the weighted sum over the sum of all channel contents proving adequate in most cases. For some peaks the deconvolution routine to be discussed later in this section was also applied.

The determination of peak areas and centroids was not as simple over most of the energy range because of the existance of large numbers of unresolved doublets or multiplets. The method chosen to separate the components in such cases was an iterative deconvolution algorithm based on Bayes' Theorem. The application of this algorithm to photo-neutron spectra has already been discussed by Kennett (Ke 73 a,b,c). A discussion of the concepts behind the algorithm is presented below.

We first consider the contents of the kth channel of the measured spectrum M_k to be the convolution of the true spectrum T with the response function of the detection system R, so

$$M_k = \sum_i R_{ki} T_i \qquad (4.3.2)$$

then the corresponding deconvolution

$$T_i = \sum_k R_{ik} M_k \qquad (4.3.3)$$

is expressed in terms of known quantities, if the above values are treated as probabilities. M_k (and T_i) may be viewed as a measure of the probability of an even occuring in channel k (or i), and the response function R_{ki} is the conditional probability of an event occurring in channel k of the measured spectrum, given that it came from channel i of the true spectrum.

The reverse conditional probability R_{ik} of the deconvolution can be expressed in terms of Bayes' theorem

$$R_{ik} = \frac{R_{ki}T_i}{\sum_j R_{kj}T_i} \tag{4.3.4}$$

By substitution from equations (4.3.3) and (4.3.4), we arrive at an expression for T_i which lends itself to an iterative solution

$$T_i(n+1) = T_i(n)\sum_k\left[\frac{R_{ki}M_k}{\sum_j R_{kj}T_j(n)}\right] \tag{4.3.5}$$

where $T_i(n+1)$ represents the contents of the ith channel of the true spectrum after $(n+1)$ iterations.

Clearly in order to evaluate the true spectrum the response function must be known. For this purpose the true photoneutron peaks were considered as delta functions compared to the observed peak

widths. The response function was considered as a Gaussian shape of varying full width half maximum, depending on neutron energy. Since, as already mentioned the F.W.H.M. varies by a factor of two over a 1 Mev range, the doconvolution technique was applied to only one small region of the spectrum at any one time. Over each small region the F.W.H.M. was viewed as constant, and then was increased before moving on to the next higher energy region. The F.W.H.M. was determined by extrapolation from the nearest energy isolated singlets on either side.

After a number of iterations (typically ~ 300) the photoneutron peaks could be reduced to two channels with the total peak area and controid conserved. A fast Fourier transform approach to the deconvolution was used to reduce computation time.

The preceeding techniques are illustrated pictorially in Fig. (4.2).

The error in the area of the peaks thus determined was assumed to be

$$\sigma^2_{AREA} = \sum_i (Y_i + B_i) \qquad (4.3.6)$$

where the sum extended over the peak region.

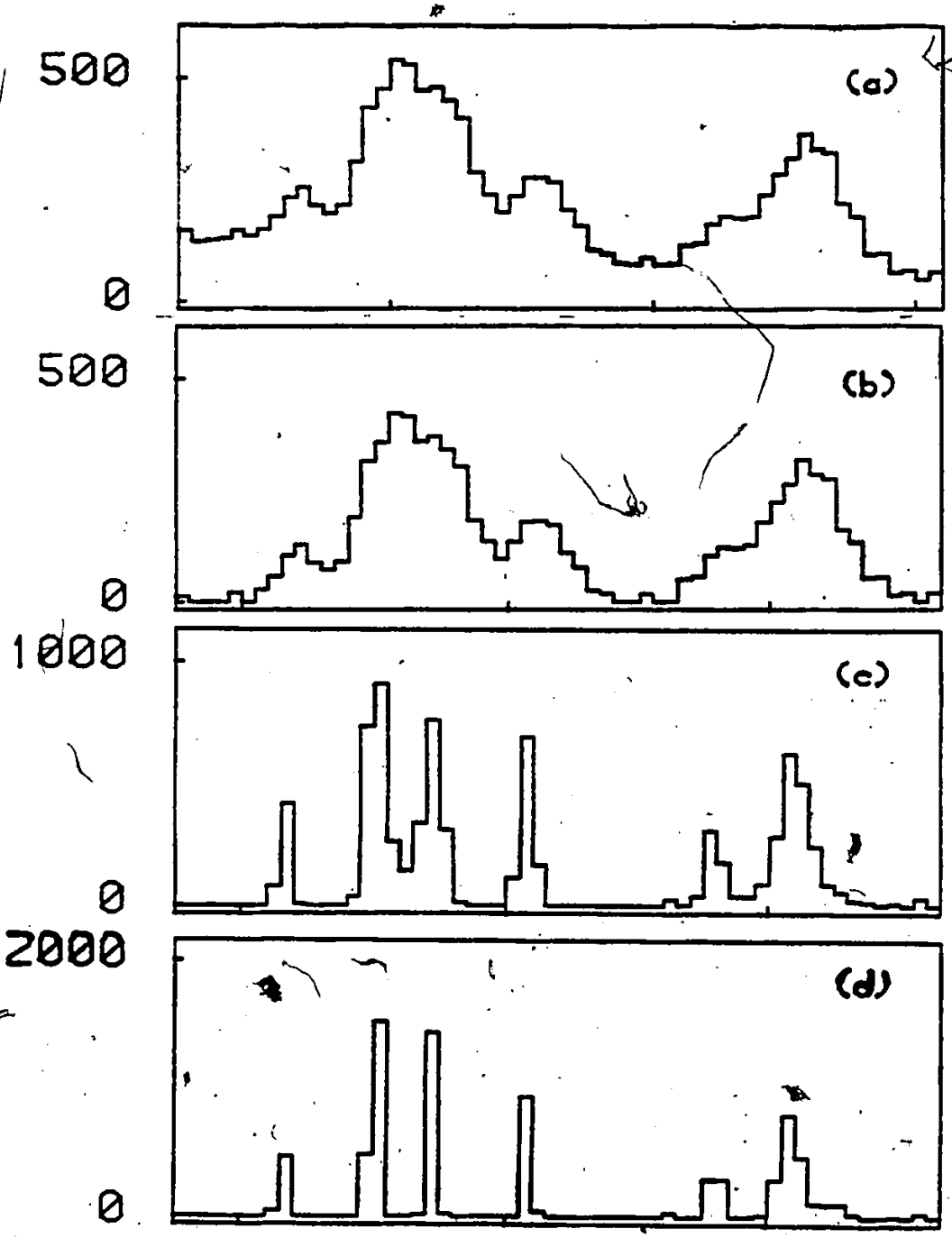

Figure 4.2 An example of the use of the Deconvolution Techniques Applied to one Region of a Photoneutron Spectrum .

a) Original Photoneutron Spectrum
b) Spectrum after subtracting background
c) Spectrum after 200 iterations of deconvolution algorithm
d) Spectrum after 500 iterations of deconvolution algorithm

The statiscal error in the centroid was simply taken as

$$\sigma_{PEAK} = \frac{F.W.H.M}{\sqrt{N}} \qquad (4.3.7)$$

where N = total number of counts in the peak.

4.4 The Angular Distribution Measurements

The strong intensity photoneutron groups resulting from aluminum (E_γ = 7724 Kev) and iron (E_γ = 7646 Kev) gamma rays on thallium, as well as iron (E_γ = 7632 kev) on a natural lead target rendered themselves applicable to angular distribution measurements. The third such experiment listed above has already been carried out (Bi 79). The results of the angular distributions and cross section measurements were used to check the validity of our technique.

The peak centroid and area determinations proceeded as in the previous section with the peak areas being evaluated at 30°, 45°, 60°, 75°, 90°, 105°, 120°, 135° and 150°.

A noteworthy problem occurred at the lowest two angles however. This was because of small angle scattering of incident γ rays from the target resulting in a large amount of pulse pileup. This in turn resulted in a high energy tail on the photoneutron peaks, and an apparent decrease in the peak area.

In order to take this effect into account, the high energy pulser spectrum was also examined as a function of angle. The

precision pulser provided a constant rate signal to the preamplifier and it was assumed that gamma ray pileup would be the same on this signal as on the real photoneutron peaks. Second and third order quadratic fits were made to the high energy pulser tail and subtracted from the apparent pulser area to give an effective pulser area. This effective area was then divided by the true pulser area (as determined from the 90° measurement) and the result was then divided into the measured photoneutron peak area to give the true area. Figure (4.3) gives evidence of the pileup problem. The technique resulted in increased error estimates for the 30° and 45° angular distribution measurements.

As shown later in this chapter, the photoneutron cross section at any one neutron energy is directly proportional to the area of the peak. Thus, for purposes of angular distribution measurements, it was deemed adequate to use the areas themselves - a practice which resulted in increased accuracy.

The photonuclear angular distributions were fit to a series of Legendre polynomials of the form $P_\nu(\cos\theta)$, by

$$\frac{d\sigma}{d\Omega}(\cos\theta)$$

$$= A(\cos\theta) = \sum_\nu a_\nu P_\nu(\cos\theta)$$

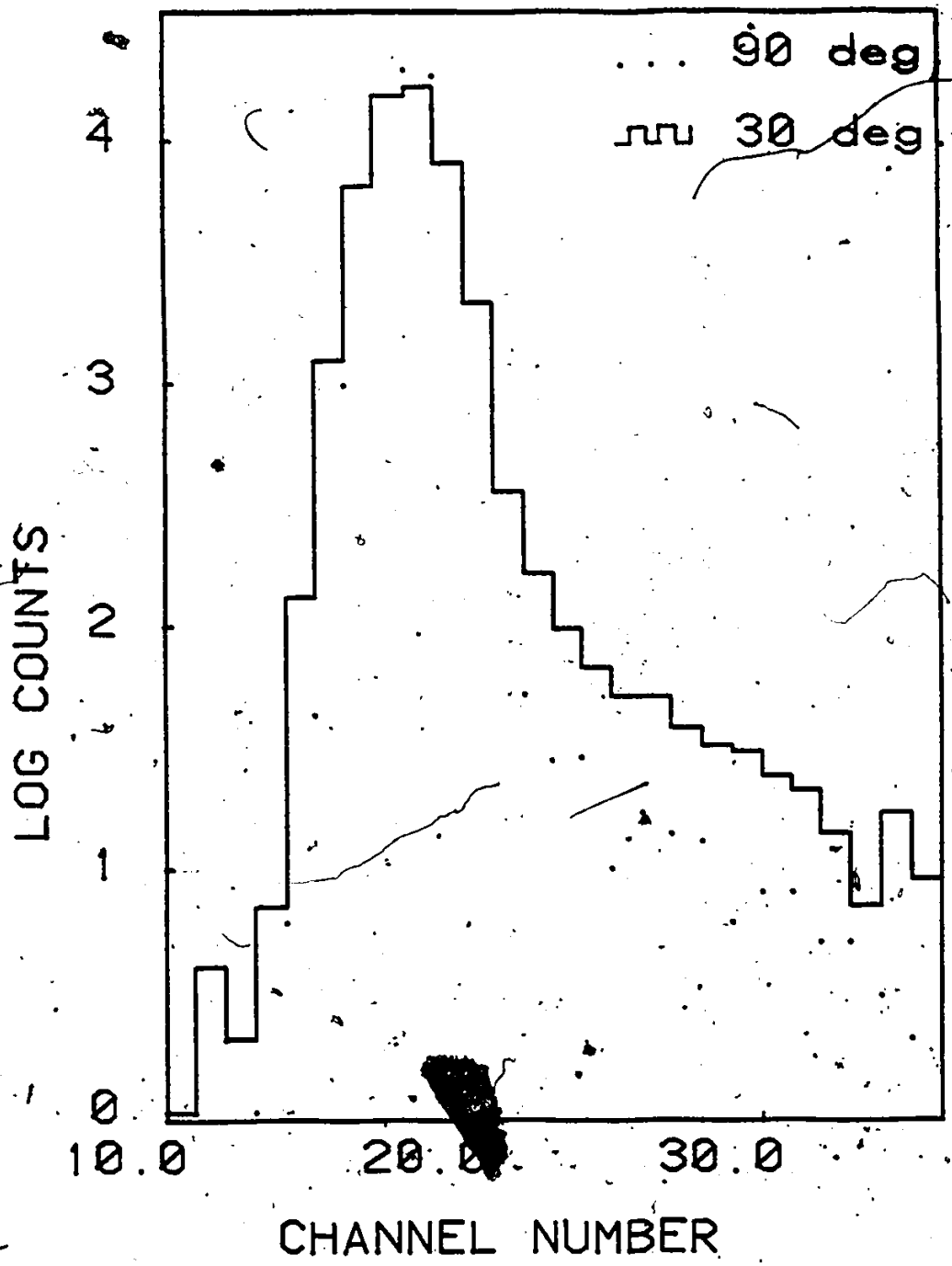

Figure 4.3 Pulse pileup associated with low angle photoneutron measurements. The high voltage pulser spectra from the iron γ ray striking the thallium target are shown at two angles.

where $A(\cos\theta)$ = photoneutron peak area at angle θ. Barkman (Ba 80) has given a more detailed account of the technique. Briefly the physical significance of the coefficients may be summarized as

a_0 -- D.C. level, the sum of intensities from all possible reaction channels.

a_1 - forward or backward asymmetry, indicative of possible E1-E2 mixing

a_2 - peakedness - indicates odd-odd or even-even ℓ neutron interference, but with no photon multipole mixing.

a_3 - similar to a_1 asymmetry, a non-zero value implies E1-E2 mixing.

4.5 Neutron Energy Calibration

The deconvolution method yielded a series of discrete peaks as a function of channel number (centroid) from the analyzer spectrum. In order to ascertain any meaningful information from these peaks it was necessary to calibrate the neutron energy as a function of channel number.

For low energy neutron measurements, this calibration was achieved with the aid of a precision pulser (ORTEC MODEL 614). The variable shaping time constant on this pulser was used to produce pulses with similar rise and decay times to those of thermal and low neutron energy peaks. The amplitude of the pulser was then varied systematically to scan the entire low energy neutron range

(corresponding to neutron energies less than ~ 400 Kev) and the centroid of each peak thus produced on the analyzer was noted. Using these results and the position of the thermal energy neutron peak (which corresponded to an actual (proton) energy of 763.8 ± 0.1 Kev) linear energy calibration of the form

$$E_n = AI + B \qquad (4.5.1)$$

where E_n = neutron energy

A,B = fitted constants

I = channel number

was achieved. During the course of experimental data collection, gain and zero shifts occurring within the amplifier were calculated by using the positions of the thermal ($E_n = 0$) and high energy precision pulser peak centroids. Briefly sumarizing this proceducure, if the thermal and pulser peaks were at channel positions T_1 and P_1 respectively during the calibration run then

$$E_n = A_1 + B_1 I \qquad (4.5.2)$$

so

$$E(T_1) = 0 = A_1 + B_1 T_1 \qquad (4.5.3)$$

and

$$E(P_1) = A_1 + B_1P_1 \qquad (4.5.4)$$

Now, if during data acquisition these two peaks shifted to T_2 and P_2 respectively, we then have

$$E(T_2) = 0 = A_2 + B_2T_2 \qquad (4.5.5)$$

$$E(P_2) = A_2 + B_2P_2 \qquad (4.5.6)$$

where A_2 and B_2 are the new parameters to be solved for.

Clearly

$$B_1T_1 = - A_1 \text{ and } B_2T_2 = - A_2 \qquad (4.5.7)$$

So, substituting

$$E(P_1) = - B_1T_1 + B_1P_1 = - B_2T_2 + B_2T_2 = E(P_2) \qquad (4.5.8)$$

so

$$B_2 = \frac{(P_1 - T_1)}{(P_2 - T_2)} B_1 \qquad (4.5.9)$$

and

$$A_2 = -\{T_2 B_2\} \qquad (4.5.10)$$

The above procedure proved adequate only for low neutron energies (typically $E_n < 400$ Kev) corresponding to transitions initiated with the aluminum and copper gamma ray sources. Above this energy the increasing ionization path lengths resulted in incomplete charge collection with the 6 μsec-shaping time used here, and the linear calibration scale proved inadequate. Rather a quadratic of the form

$$E_n = A + BI + CI^2 \qquad (4.5.11)$$

proved more tenable. The exact details of the determination of the above parameters depended on the photoneutron target, as outlined below.

4.5.1 Energy Calibration for the Thallium Spectra

The photoneutron spectrum from the aluminum source on thallium produced two exceptionally intense peaks which could be then used to firmly establish the ^{205}Tl photoneutron Q value. As will be seen in the next chapter this lead to $Q\{^{205}Tl(\gamma,n)^{204}Tl\} = (7549 \pm 1)$ Kev. The photoneutron spectrum from the copper source was then analyzed and the energies of the neutron peaks were calculated in 3 ways for comparison.

(i) The precision pulser calibration method previously discussed.

(ii) Since the energy levels in ^{205}Tl are well known then the neutron energies can be arrived at from

$$E_n = \frac{A - 1}{A}(E_\gamma - Q - E_x) \qquad (4.5.12)$$

A linear fit of neutron energy vs channel number was made.

(iii) A quadratic fit of neutron energy vs channel number was made.

The results of the three different methods are presented in Table (4.1). A discussion of the error assignments appears in the next section. Good agreement is seen between the three methods, having implications for the tantalum spectra which will be discussed later.

For photoneutron spectra arising from the nickel and chromium sources the linear energy calibrations proved inadequate. The energy calibration method then was to use the photoneutron Q value previously determined to ascertain the neutron energies of well known transitions to levels in ^{204}Tl. For each source the number of such easily determined neturon energies was more than 10. The strong transitions arising from neutron capture gamma rays from the aluminum casings of the sources as well as the thermal ($E_n = 0$) peak also proved useful for calibration. A quadratic fit of energy to peak centroid was then made.

TABLE 4.1

COMPARISON OF METHODS OF DETERMINING PHOTONEUTRON PEAK ENERGIES

COPPER SOURCE ON THALLIUM TARGET METHOD

CENTROID (CHANNEL NUMBER)	$\frac{\text{I.D.}}{(E_\gamma - E_x)}$	E_n	(1) (±.8)	(2) (±.5)	(3) (±.5)
146.5 ± .01	Thermal	0 ± 1	0.4	.005	-.1
152.9 ± .03	7724-141	33.8 ± 1	34.9	34.8	34.3
158.5 ± .08	7915-300	65.7 ± 1	65.6	65.2	64.6
188.0 ± .18	7915-141	223.9 ± 1	225.6	225.6	225.0
178.5 ± .1	7724-0	174.1 ± 1	174.8	173.9	173.3
213.5 ± .09	7915-0	364.2 ± 1	365.8	364.3	363.8

Methods

(1) Precision Pulser Method
(2) Linear Least Squares Fit
(3) Quadratic Least Squares Fit

It was noted that the absolute value of the quadratic coefficient C was never more than 10^{-4} of the linear coefficient and was always negative - which was to be expected from the physical nature of the term.

4.5.2 Energy Calibration for the Tantalum Spectra

With verification of the methodology from the thallium spectra, the precision pulser calibration technique was deemed accurate enough to evaluate neutron energies for the spectra arising from the aluminum and copper sources. Thus the $^{181}Ta(\gamma,n)^{180}Ta$ Q-value and six excited state energies were determined. These energies were then used as an "internal calibration" for the nickel and chromium neutron energy spectra. It should be noted that since these transitions resulted in high neutron energies ($E_n \sim 1400$ Kev) the well-known zero energy thermal peak proved useful as a low energy calibration point.

Error in Energy Level Assignments

For the purpose of assigning errors to the nuclear energy levels and Q values, each centroid corresponding to the population of an individual level was originally assigned a statistical error

$$E_s = \frac{\text{F.W.H.M.}}{\sqrt{N}} \qquad (4.5.13)$$

where F.W.H.M. = full-width half maximum of the neutron energy peak (Kev)

N = total number of counts in the peak

The fitting error could then be introduced by examination of the variance-covariance matrix as before and the error in the neutron energy was

$$E_E = \sqrt{(E_S)^2 + (E_F)^2} \qquad (4.5.14)$$

where E_F = fitting error

Now for the case of the tantalum spectra, where the excited state energies were not well known, the error in the photoneutron Q value was first determined as in eqn (4.5.14). The error in any individual excited state energy was then taken to be the quadrature sum of the neutron energy assignment error and the error in the Q-value.

4.6 Photoneutron Cross Sections

In order to calculate the cross section for any individual photoneutron group, a knowledge of many individual parameters is required. While the expression for the cross section is relatively straightforward, the acquirement of the parameters is not necessarily so. This introductory section simply states the general photoneutron cross section, while the following subsections give special discussion to the complexities contained therein.

Consider that the neutron detector measures R neutrons per second corresponding to photoneutron events initiated by photons of

energy E_γ, which then leave the residual nucleus of mass (A - 1) in the excited state E_x. We may then relate R to the cross section by:

$$R(A\text{-}1,E_x,E_\gamma) = \phi(E_\gamma)\left(1 - \exp\left(-\sum_j n_j \sigma_\gamma^j t\right)\right)\frac{n_A \sigma_{\gamma n}(A,E_x,E_\gamma)}{\sum_j n_j \sigma_\gamma^j}\,\varepsilon(E_n) \qquad (4.6.1)$$

where n_j = number of nuclei per unit volume of the jth isotope

n_A = number of nuclei per unit volume of the isotope of mass A

σ_γ^j = total photon interaction cross section for energy E_γ and the jth isotope

t = target thickness

$\sigma_{\gamma n}$ = photoneutron cross section

$\varepsilon(E_n)$ = efficiency of the detector for neutrons of energy E_n

$\phi(E_\gamma)$ = total flux (s^{-1}) for photons of energy E_γ incident upon the target

We may simplify eqn (4.6.1) by assuming that, since all photoneutron cross sections near 9 Mev will have values of a few millibarns whereas total cross sections will be of the order of 15 barns, then to a very good approximation all σ_γ^j are the same, and we denote them σ_γ. Thus

$$\sum_j n_j \sigma_\gamma^j = n\,\sigma_\gamma \qquad (4.6.2)$$

where n is the total number of nuclei per unit volume. Setting $Y_A = n_A/n$ we have

$$\sigma_{\gamma n}(A,E_x,E_\gamma) = \frac{R\ \sigma_\gamma}{\phi(E_\gamma)(1 - \exp(-n\ \sigma_\gamma t))Y_A\ \varepsilon(E_n)} \qquad (4.6.3)$$

4.6.1 The Total Photon Interaction Cross Sections

The total photon interaction cross sections used here are taken from the work of Storm and Israel (St 70). These authors have tabulated the total cross sections for a range of incident photon energy from 1 Kev to 100 Mev for targets ranging from Z = 1 to Z = 100. The quoted accuracy on these results is under 10%, and they may be graphed as smoothly varying curves in the energy region of interest for the photoneutron experiments. Typical values listed are for Tl(Z = 81) then σ_γ = 15.5 barns and 16.3 barns at 8 and 10 Mev respectively while for Ta(Z = 73) we find 13.1 barns and 13.9 barns respectively.

4.6.2 Energy Dependent Efficiency of the ^{3}He Spectrometer

The relative efficiency of the ^{3}He neutron detector may be expected at first glance to follow the ^{3}He(n,p)^{3}H cross section. However, this will only be true for lower neutron energies (typically below E_n = 200 Kev). Above this energy, as has previously been discussed, there is a large probability that the proton or triton track lengths will extend outside the active volume of the detector, resulting in a lower than full energy peak being recorded.

To calculate this effect McFee (Mc 77) performed experiments with known high energy neutron fluxes of varying energies resulting from proton bombardments of a lithium target causing the $^{7}Li(p,n)^{7}Be$ reaction. This author used a target to detector geometry similar to that used in the photoneutron experiments, and measured relative efficiency. The results were in good agreement with the experiments of Franz (Fr 73) and Cuttler (Cu 73). Recently Sailor and Prussin (Sa 80) calculated the relative detector efficiency arising from a point source of neutrons located near the surface of the spectrometer by using a Monte Carlo approach. Their results showed good agreement with the work of Franz (Fr 77).

Using these papers as a guideline a fit was made to the relative efficiency curve of the form:

$$\varepsilon = 23\ E_n^{-.68} \qquad (E_n < 100\ \text{Kev})$$

$$\varepsilon = 1.4916 - 6.13 \times 10^{-3} E_n + 1.33 \times 10^{-5} E_n^2 - 1.29 \times 10^{-8} E_n^3 \qquad (100\ \text{kev} < E_n < 2000\ \text{Kev})$$

$$\varepsilon = 170\ E_n^{-.86} \qquad (E_n > 2000\ \text{Kev})$$

The fit was seen to agree to the calculated efficiency values to within 5% over the entire energy range.

Finally the absolute efficiency must be known at least one point to noramalize the curve. We again turn to the work of McFee who has shown that at E_n = 1 Mev then $\varepsilon = 5.08 \times 10^{-5}$(Mc 77).

4.7 Gamma Ray Flux Measurements

By far the most difficult parameter to obtain for substitution into eqn (4.63) was ϕ, the incident γ ray flux upon the target. The experimental system used to measure the gamma ray fluxes has already been discussed (see sec. 3.5). An illustration of the effect of the pair spectrometer in "cleaning up" a gamma ray spectrum is shown in Fig. (4.4), which represents the gamma ray spectrum from the ^{56}Co source when placed approximately 10 cm from the front face of the centre detector.

4.7.1 Absolute Energy Calibration up to 3.6 Mev

The experimental set up for the absolute energy calibration with the ^{56}Co source is shown in Fig. (4.5).

The lead collimators were used to produce an approximate 2.54 diameter beam at the centre detector. The source was positioned on the detector axis and was contained in a plastic vial of approximately .75 cm diameter.

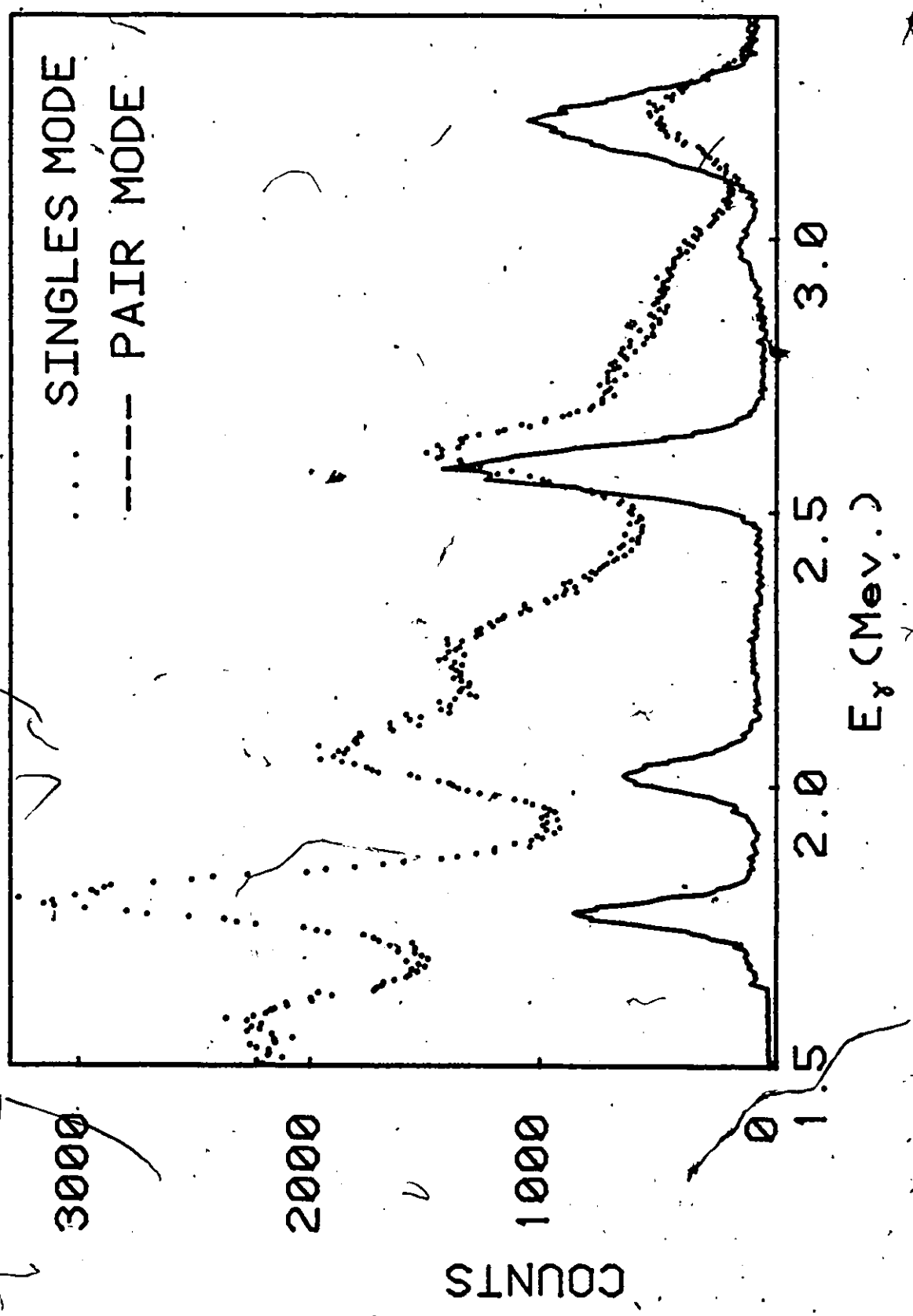

Figure 4.4 Comparison of spectra produced from ^{56}Co γ ray source. The advantages of the use of the spectrometer in the pair mode are clear. The pair mode spectrum has been shifted so that the energy scales coincide.

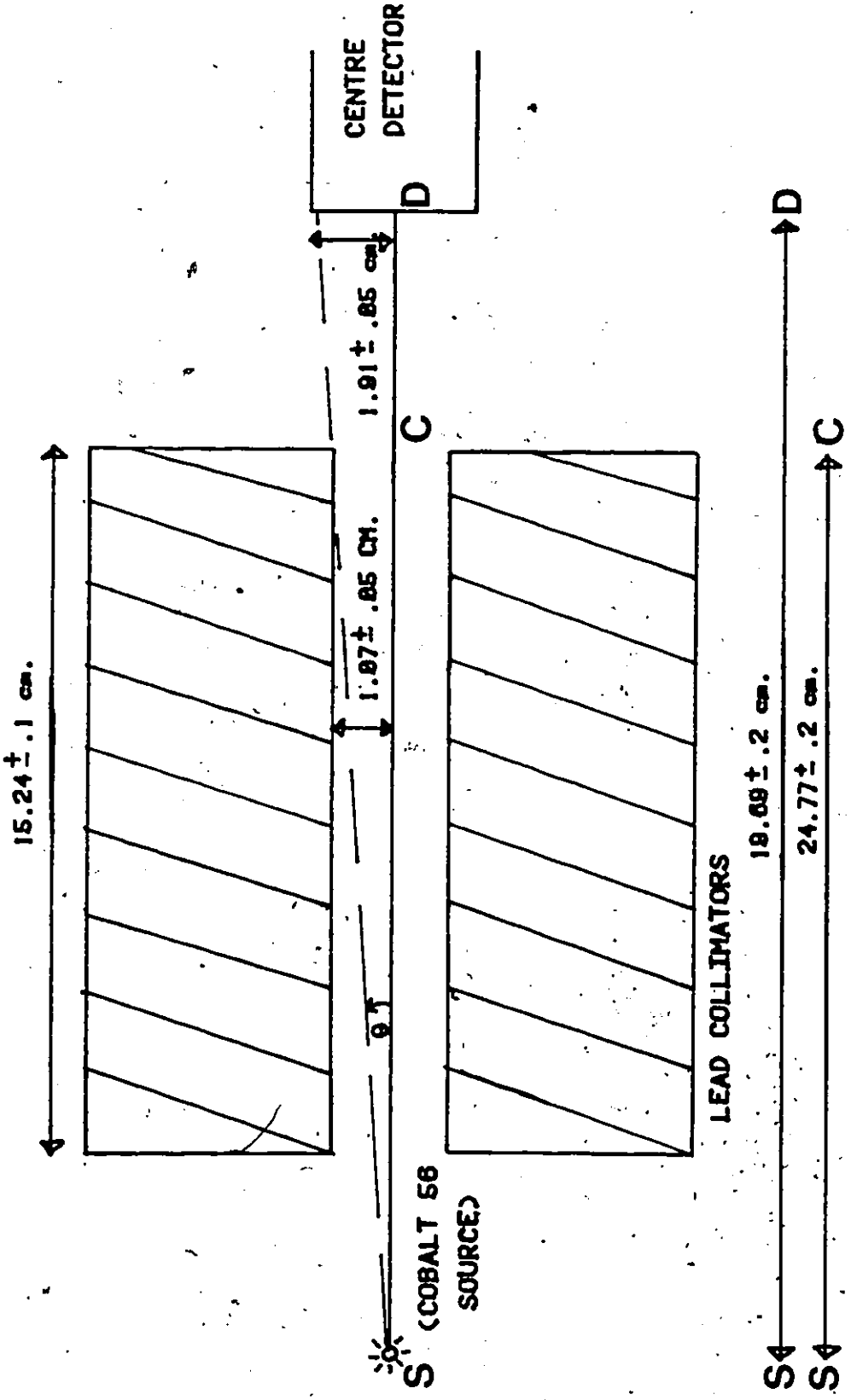

Figure 4.5 Experimental Geometry for Absolute Efficiency Determination of the Pair Spectrometer

The coincidence spectrum was collected over a 6 day period. The energy spectrum thus acquired is shown in Fig. (4.6).

The next procedure was comparison of the prepared source with a known standard. Direct comparison of source and standard intensities in the ionization well chamber gave the source strength as (8.30 ± 1%) times the standard.

By consideration of the decay of the source ($\tau_{\frac{1}{2}}$ = 78.8 days) and the solid angle considerations the total number of disintegrations during collection time could easily be attained.

The peak areas from Fig. (4.5) were determined using the cubic spline method previously described in this chapter. Peak identification proved no problem with the aid of Table (3.3). It was decided to use the 2.6 Mev peak as the standard for absolute calibration since it was the highest energy single isolated peak, and also happened to coincide with a peak energy arising from neutron capture in Be, which will be seen later to prove useful for comparison.

Once the areas of all peaks were calculated the relative efficiency of the detector as a function of incident gamma ray energy was calculated from

$$\varepsilon(E_\gamma) = \frac{\text{Area}\ (E_\gamma)}{I_\gamma} \qquad (4.7.1)$$

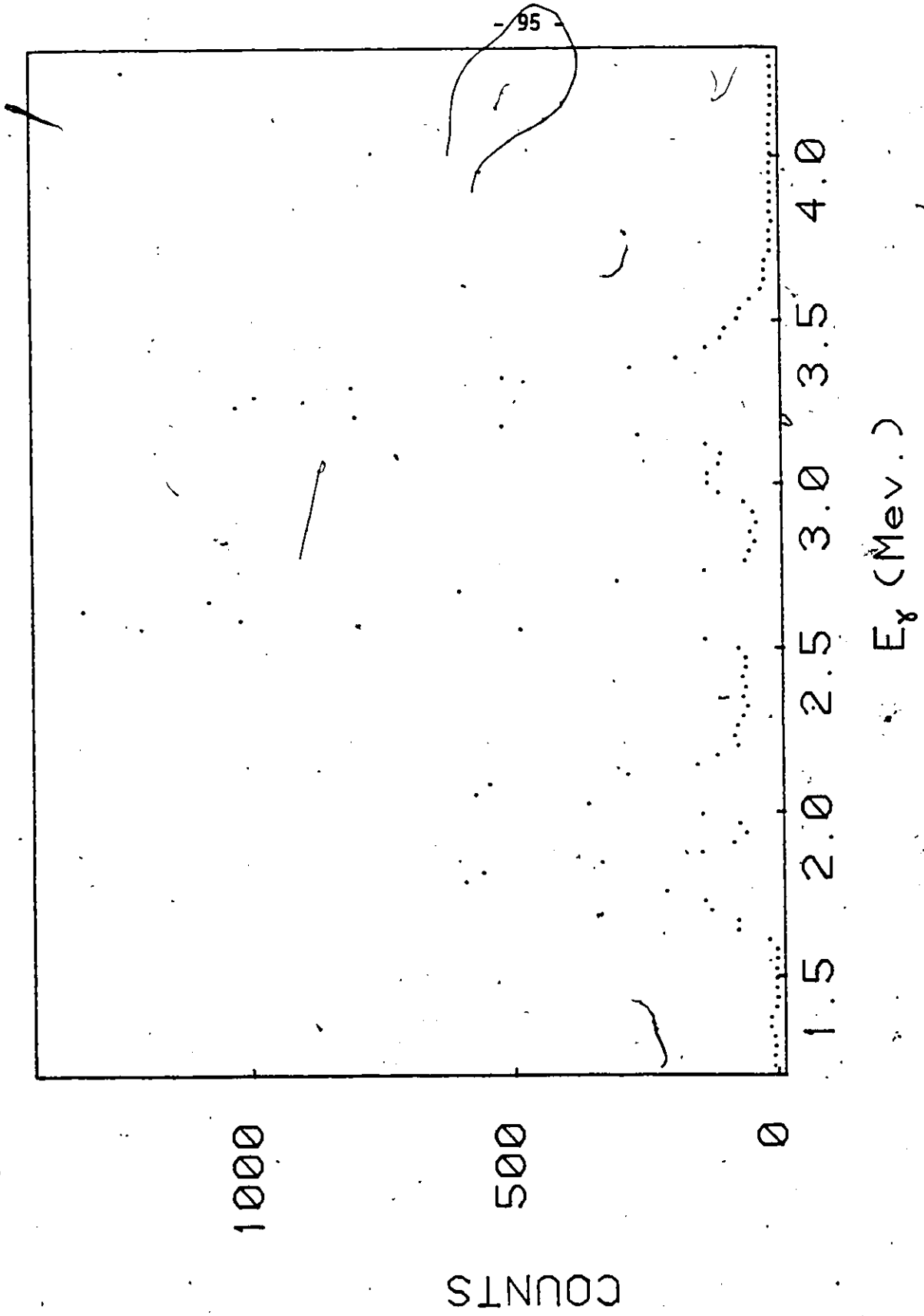

Figure 4.6 Pair Coincidence Gamma Ray Spectrum from the ^{56}Co Source

where I_γ is the number of γ rays produced per disintegration.

Finally a first order correction was made for transmission of 2.6 Mev γ rays through the lead collimators. Referring to the diagram, transmission may occur when $\theta_{min} < \theta < \theta_{max}$. Where

$$\theta_{min} = \sin^{-1}\left(\frac{1.27}{19.67}\right) = 3.70° \qquad (4.7.2)$$

$$\theta_{max} = \sin^{-1}\left(\frac{1.91}{24.77}\right) = 4.41° \qquad (4.7.3)$$

It is now necessary to calculate the radii corresponding to θ_{max} and θ_{min} at C, i.e. the limiting values of these radii in the lead collimator.

Clearly

$$R_{min} = 1.27 \text{ cm, and}$$
$$R_{max} = (19.69 \text{ cm}) \sin 4.41° = 1.51 \text{ cm}$$

The transmission may then be defined from simple geometry as

$$T = \int_{R_{min}}^{R_{max}} \frac{2r}{R_{min}^2} \exp(-\mu_4(E_\gamma)\frac{(r - R_{min})}{r}\sqrt{r^2 + (TS)^2})dr \qquad (4.7.4)$$

where μ_4 = linear absorption coefficient for lead.

From Storm and Israel (St 70) we note

$$\mu_4(2.6 \text{ Mev}) = 0.487 \text{ cm}^{-1} \qquad (4.7.5)$$

It was found that, after integrating numerically, the transmission resulted in an increased solid angle of (3.54 ± .04)%. These facets combined to give an absolute peak efficiency of $\epsilon = (4.996 \pm .21) \times 10^{-4}$ at 2.6 Mev.

4.7.2 Relative Energy Calibration for Higher Gamma Ray Energies

The energy spectra from neutron capture γ rays produced by irradiation of nitrogen, beryllium and iron targets in the thru tube facility are shown in Figs. (4.7), (4.8) and (4.9). These spectra proved particularly useful for analysis because of the wide energy level spacings compared to the detector resolution (F.W.H.M. ≈ 200 Kev). One important feature is readily apparent and that is the low energy tail associated with peaks of energies greater than ~ 6 Mev. This may be viewed as being caused by energy losses due to Bremsstrahlung and range effects, factors which will be discussed later (see Appendix). The method of determination of peak areas and relative efficiencies here proved somewhat more difficult because of the non-Gaussian nature of the peaks. The method chosen was to initially fit a first, second or third degree polynomial to the data points corresponding to higher energy region slightly above the peak to be analyzed. The background thus fitted was then extrapolated into the

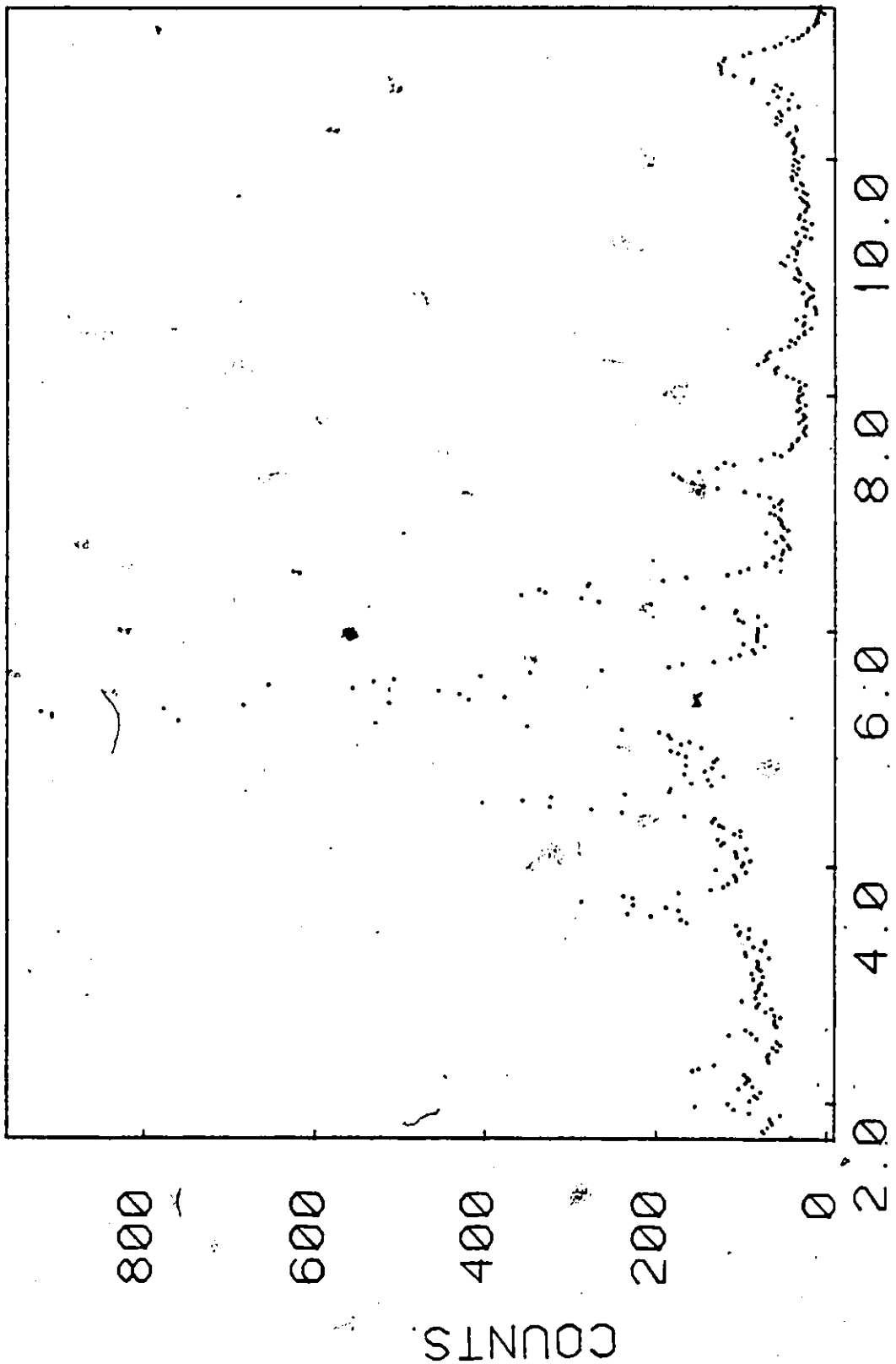

Figure 4.7 Pair Coincidence Capture γ Ray Spectrum from Nitrogen Sample in McMaster Tangential Thru Tube Facility

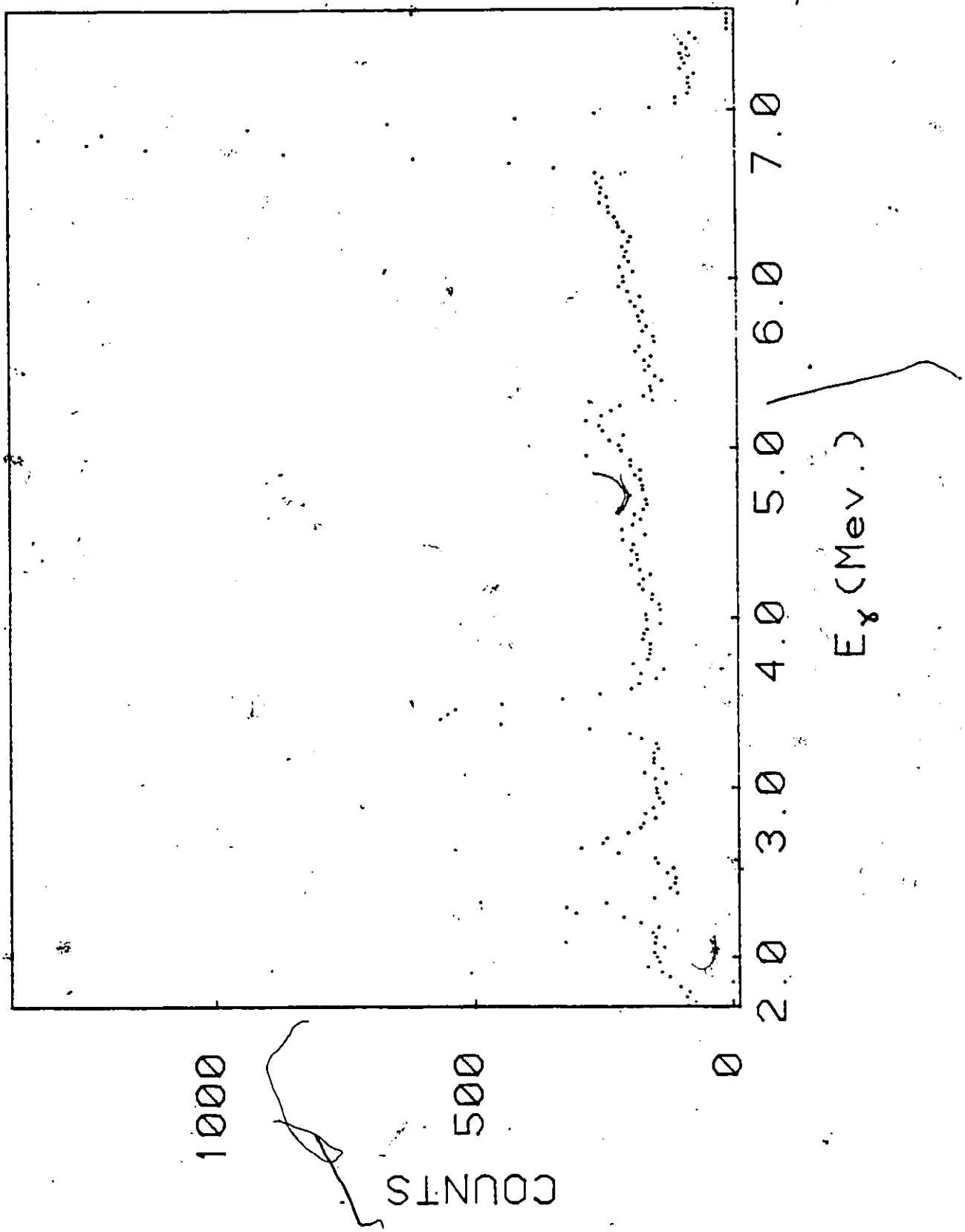

Figure 4.8 Pair Coincidence Capture γ Ray Spectrum from Beryllium Sample in McMaster Tangential Thru Tube Facility

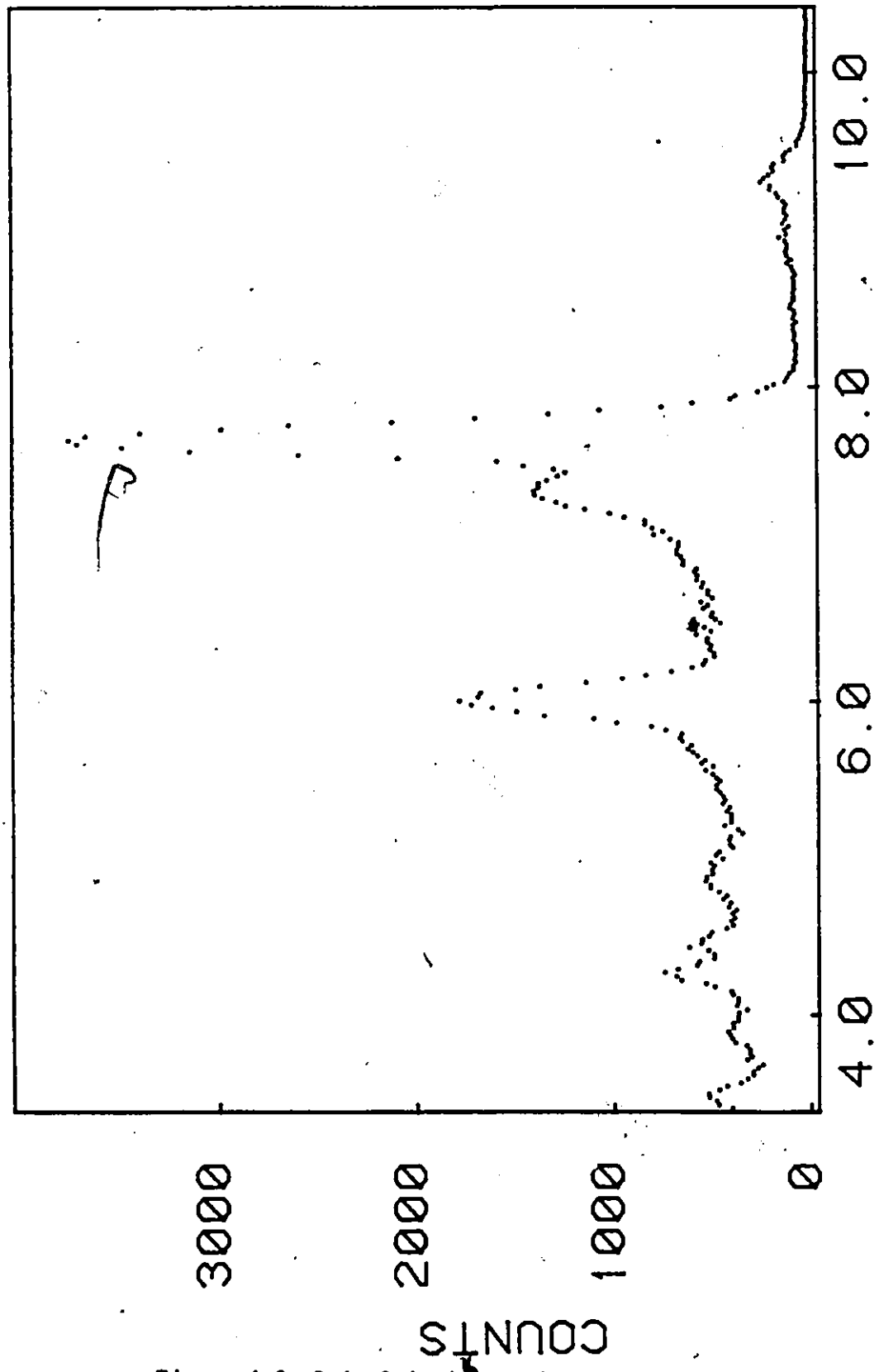

Figure 4.9 Pair Coincidence Capture γ Ray Spectrum from Iron Sample in McMaster Tangential Thru Tube Facility

region of the peak and subtracted channel by channel from the peak. A Gaussian fit was then made to the region of the peak deemed to be above the low energy tail to determine the centroid. In a manner analogous to Heath (He 64), the number of counts to the right of the centroids were doubled to yield the total peak area. The errors in the areas were taken as the quadrature sum of the statistical errors arising from the counts in the peak and the background fitting error. It should be noted that his method allowed only areas to be determined for single isolated peaks, however since the nitrogen spectrum offered seven such peaks it was deemed accurate enough.

The relative efficiency for each energy under consideration was calculated as in the previous section. Thus a curve of relative efficiency for $3 < E_\gamma < 11$ Mev was achieved. This curve and the curve from the previous section were normalized to each other by integration.

It should be noted that an assumption has been made here which needs some verification. The actual photon beam and the collimated ^{56}Co beam were both 2.54 cm in diameter, while that produced at the through tube was approximately 1 cm in diameter. The assumption made is that the losses due to Bremsstrahlung and range loss effects would be independent of beam size. The assumption finds support in the work of Dance et al (Da 68, 70). Thick targets of varying Z were bombarded by electron beams with energies in the range of 0.2 to 2.8 Mev. The angular distributions of the emitted Bremsstrahlung spectra were

strongly peaked with over 80% of the distribution in the forward direction. Berger and Seltzer (Be 68) have shown similar results for electrons transmitted through various thick targets.

This forward peakedness, if assumed consistent for NaI should result in similar distributions of energy losses from both beams.

4.7.3 Photon Beam Spectral Components

The coincidence spectrometer γ ray energy spectra arising from the various photon sources, as well as the spectrum with no source in the housing are presented in Figs. (4.10) to (4.15). The energy calibration here is straightforward since the capture γ ray energies are so well known (Ra 67). The extraction of peak areas followed along the lines of the preceeding section with again considerable "tail" contributions arising. The area of the highest energy line in each spectrum was measured with the exception of the iron spectrum where the 7.64 Mev doublet was used. Thus the only spectrum in which the most intense γ ray transition was not used was that arising from the chromium source. In this case however the ratio of intensities between the strongest (E_γ = 8.884 Mev) and the 9.720 Mev lines is well enough known to present no problems.

One interesting feature of all spectra is the presence of the 7.724 Mev line arising from neutron capture on aluminum in the source container to some extent, but mainly from the core fuel element

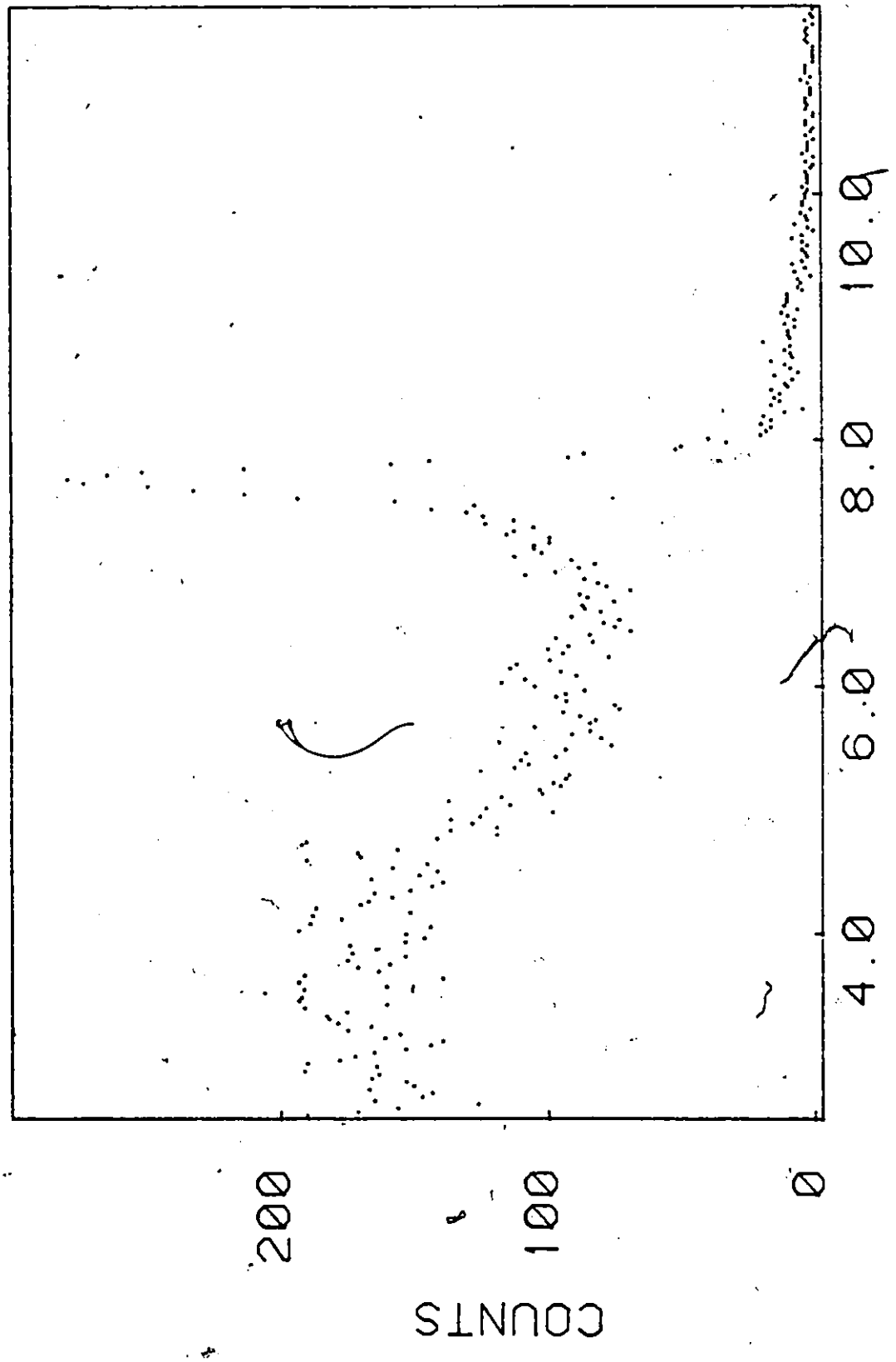

Figure 4.10 Aluminum Beam Pair Coincidence Spectrum

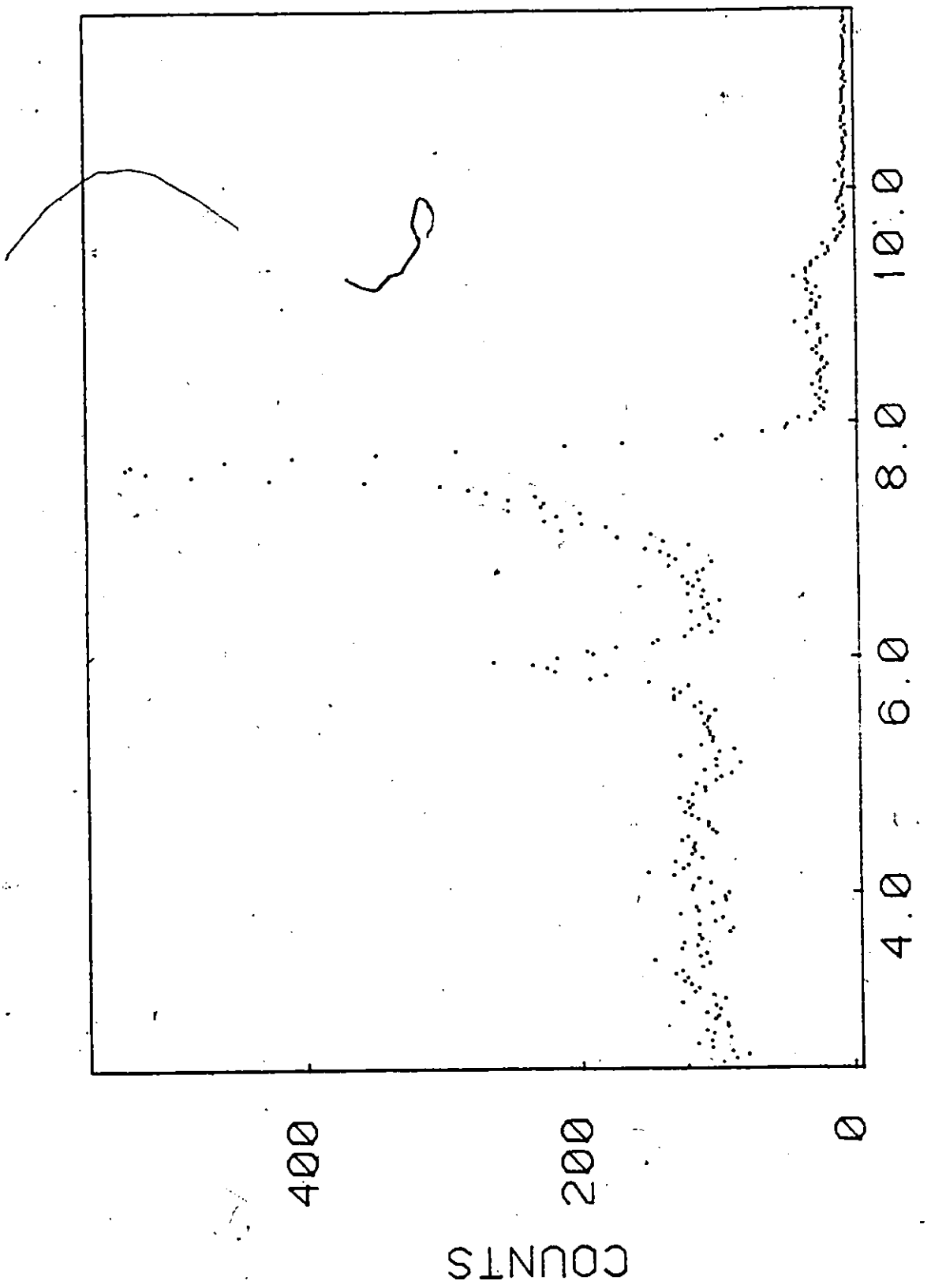

Figure 4.11 Iron Beam Pair Coincidence Spectrum

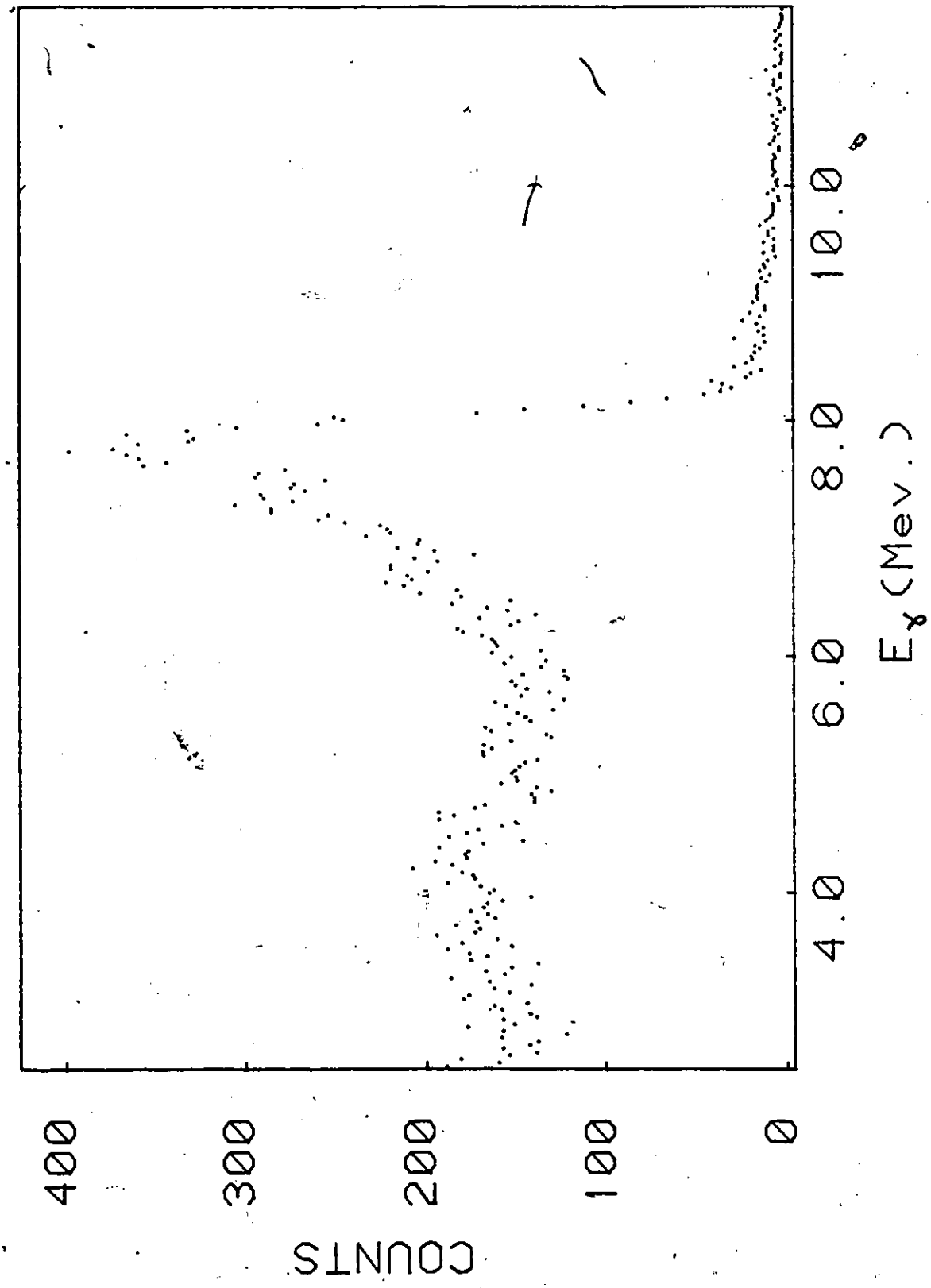

Figure 4.12 Copper Beam Pair Coincidence Spectrum

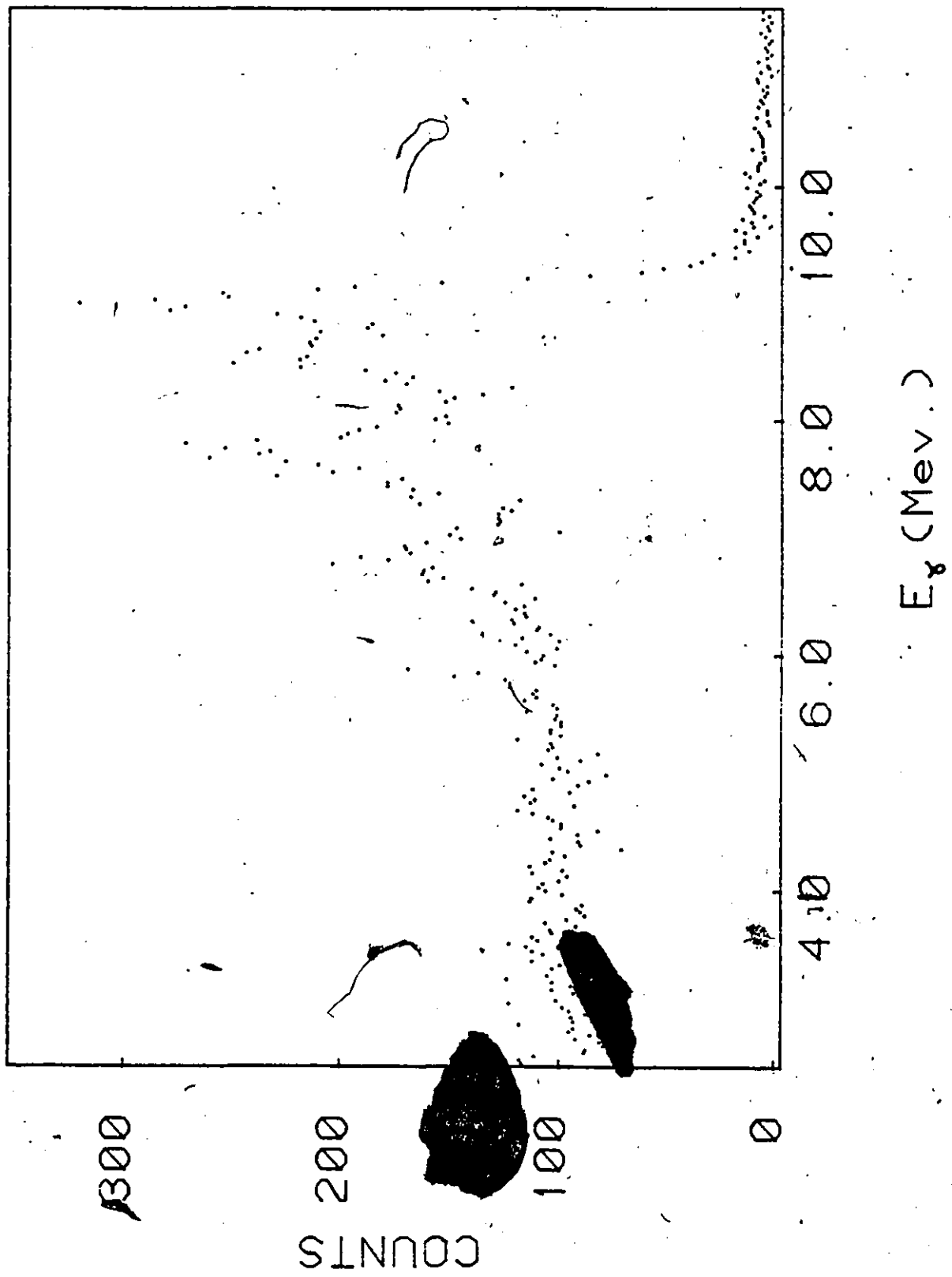

Figure 4.13 Nickel Beam Pair Coincidence Spectrum

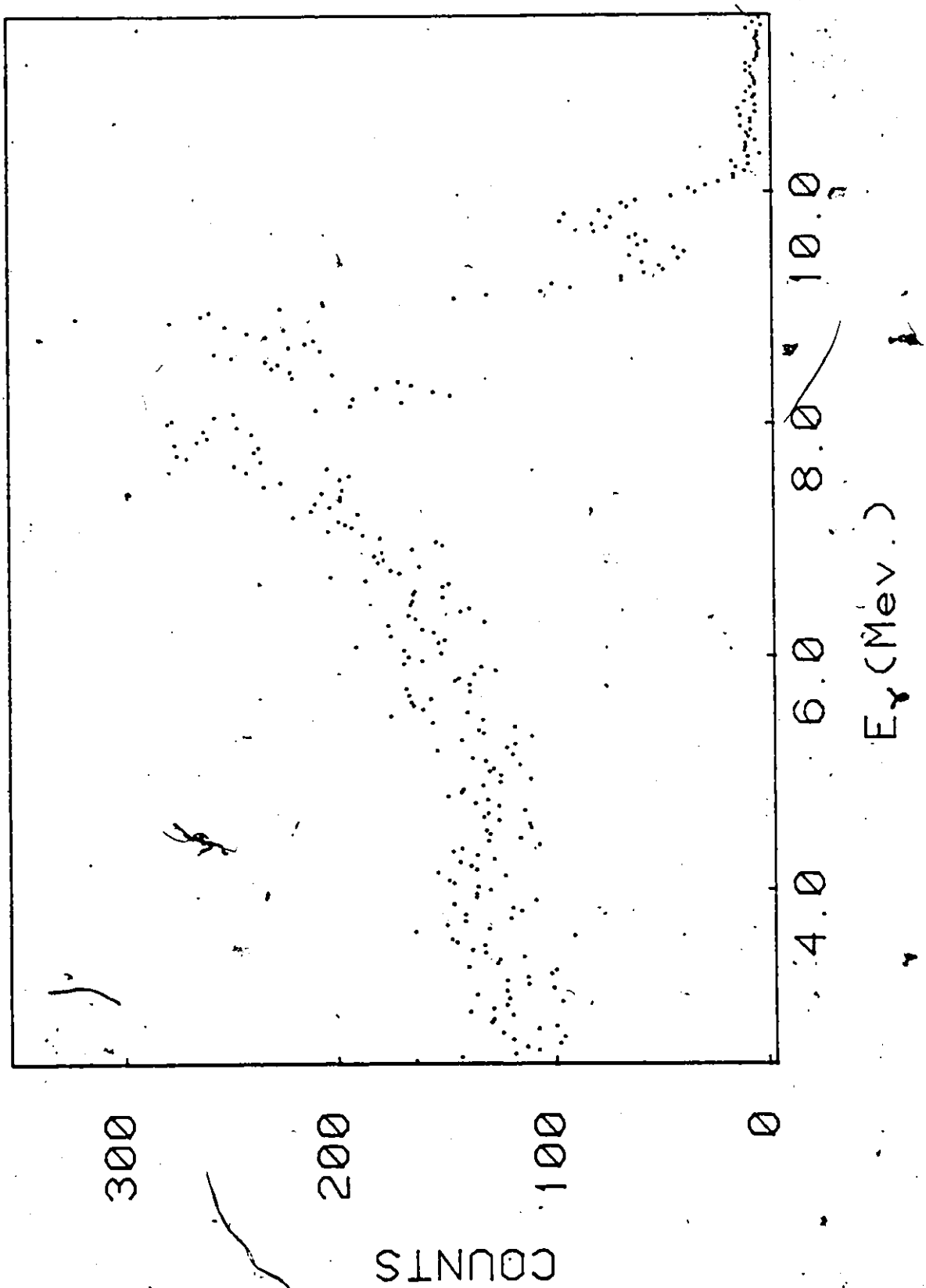

Figure 4.14 Chromium Beam Pair Coincidence Spectrum

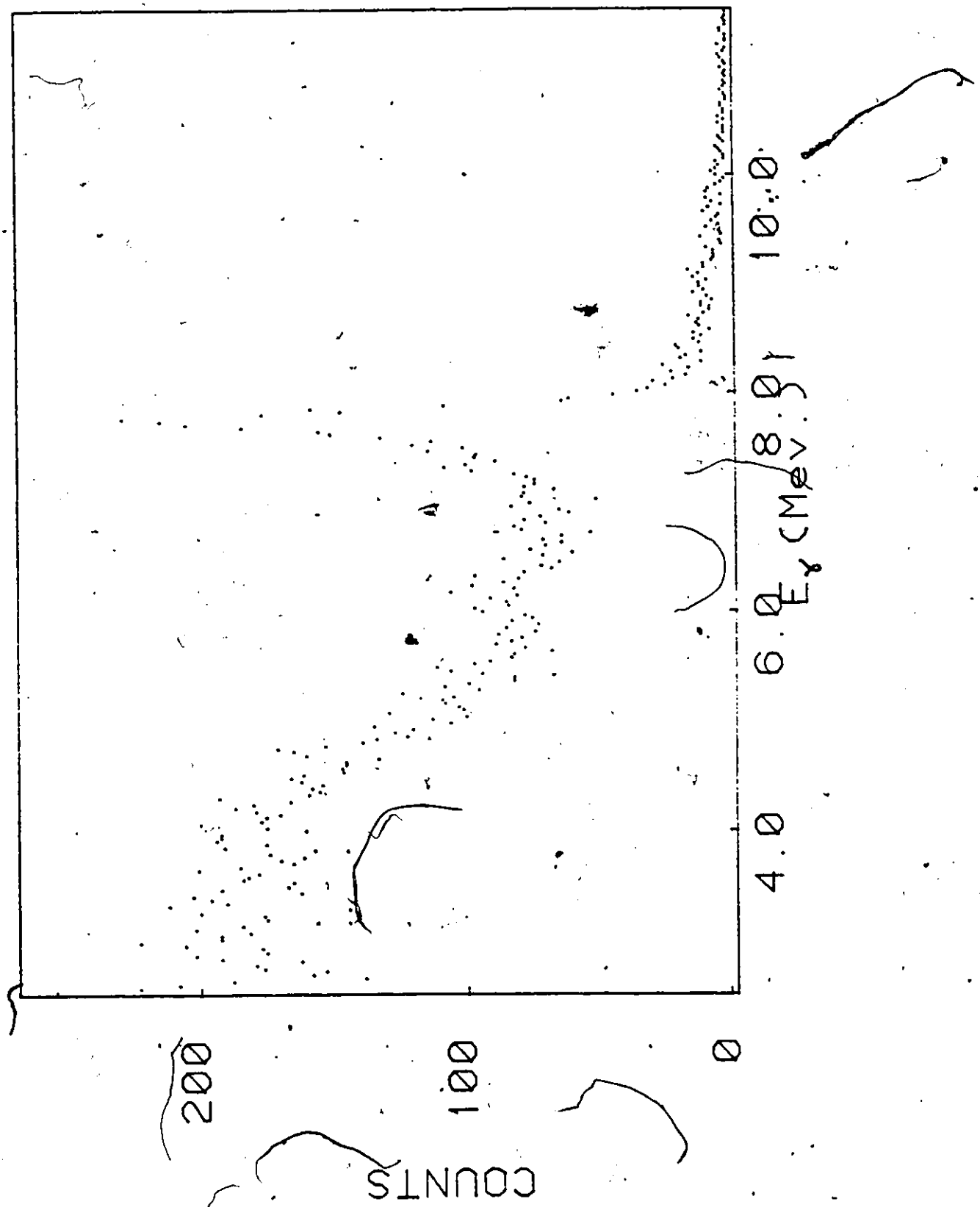

Figure 4.15 Pair Coincidence Spectrum Arising with no Source in Housing. The predominance of aluminum γ rays from neutron capture in the reactor core is clear.

cladding and element grid housing. This is clearly visible from the spectrum with no source being irradiated. The presence of this line proved a hindrance when measuring the areas of the copper (E_γ = 7.915 Mev) and iron doublet lines which were not clearly resolved from the aluminum line. Particular discussion of the circumvention of these problems is given in Chapter 5.

The spectra shown represent a data acquisition time of 1000 sec with reactor power at 10 Kw in order to minimize detector dead time losses. To relate the area $A(E_\gamma)$ of these peaks to the incident γ ray intensity $\phi(E_\gamma)(sec^{-1})$ at 2 Mw (normal reactor operating power) we write,

$$\phi(E_\gamma) = \frac{A(E_\gamma)}{\varepsilon_a(E_\gamma)} \cdot \frac{2 \times 10^6}{10 \times 10^3} \cdot \frac{1}{10^3 \text{ sec}} \qquad (4.7.6)$$

where $\varepsilon_a(E_\gamma)$ = absolute detector efficiency at energy E_γ.

Now

$$\varepsilon_a(E_\gamma) = \varepsilon_a(2.6 \text{ Mev}) \times \frac{\varepsilon_R(E_\gamma)}{\varepsilon_R(2.6 \text{ Mev})} \qquad (4.7.8)$$

with

$\varepsilon_a(2.6 \text{ Mev})$ = absolute detector efficiency at 2.6 Mev

$= (4.996 \pm .21 \times 10^{-4})$

$\varepsilon_R(E_\gamma)$ = relative detector efficiency at E_γ

$\varepsilon_R(2.6\ \text{Mev})$ = relative detector efficiency at 2.6 Mev.

So finally we have,

$$\phi(E_\gamma) = \frac{A(E_\gamma)}{(2.498 \pm .11) \times 10^{-3}} \times \frac{\varepsilon_R(2.6\ \text{Mev})}{\varepsilon_R(E_\gamma)}$$

The factor $\frac{\varepsilon_R(2.6)}{\varepsilon_R(E_\gamma)}$ is readily available from the efficiency curve to be presented in Chapter 5.

When calculating a cross section the propagation of errors followed normal procedure.

4.8 Detection Criteria

Some transitions to excited states E_x in the photoneutron spectrum showed no corresponding neutron peak. Rather than assign a value of zero for the photoneutron cross section, it was decided to place a lower limit based upon detection efficiency. To this end, in the area corresponding to a transition to E_x it was decided that a peak would be observed only if three consecutive channels had counts greater than $3\sqrt{Y_i}$ where Y_i was the average of the measured spectrum in that

range. Thus the minimum detectable area was $9\sqrt{Y_i}$, and the corresponding maximum cross section for the transition was deduced from this.

This concept of arriving at a maximum cross section for transitions which were not observed is important when considering the total reaction cross section at any one gamma ray energy, and when discussing reduced widths. The concept is particularly important when the 9.720 Mev chromium γ ray transitions are being considered. Here the relatively weak gamma ray flux and rapidly decreasing neutron detection efficiency for low excited state components, make detection difficult.

CHAPTER FIVE

5.0 RESULTS AND DISCUSSION

5.1 Determination of Neutron Energies and Photoneutron Q-Values

The first step in the placement of nuclear levels is the measurement of neutron energy. For both the thallium and tantalum targets the aluminum and copper initiated spectra were analyzed by employment of the precision pulser calibration method to determine these energies. The results of this analysis are presented in Tables (5.1) and (5.2). The spectra thus analyzed are shown in Figs. (5.1), (5.2), (5.3) and (5.4).

Both tantalum spectra data were acquired over a 500,000 sec. counting period, whereas the aluminum and copper γ ray spectra on thallium represent acquisition times of 200,000 sec. and 250,000 sec. respectively.

The major feature of the thallium spectra are the very high intensity transitions to both the ground state (E_x = 0) and first excited state (E_x = 141 Kev) initiated by the strong aluminum γ ray (E_γ = 7724 Kev). These strong transitions were used to clearly establish the $^{205}Tl(\gamma,n)^{204}Tl$ Q-value as 7549 ± 1 Kev. The two

TABLE 5.1

NEUTRON GROUPS AND ASSOCIATED FINAL STATES OBSERVED IN THE $^{205}Tl(\gamma,n)^{204}Tl$ REACTION

NEUTRON ENERGY (Kev)	Q-VALUE (Kev)	ASSIGNED FINAL STATE (Kev)
Aluminum E_γ = 7724 Kev		
175 ± 1	7549	0 ± 1
33 ± 1	7691	142 ± 1
Copper E_γ = 7915		
365 ± 1	7548	-1 ± 1
226 ± 1	7687	139 ± 2
174 ± 1	7739	*191 ± 2
65 ± 1	7848	300 ± 2
34 ± 1	7879	*331 ± 2

* denotes contribution from Aluminum (E_γ = 7724 Kev γ ray)

Photoneutron Q-value

$$Q\{^{205}Tl(\gamma,n)^{204}Tl\} = 7549 \pm 1 \text{ Kev}$$

TABLE 5.2

NEUTRON GROUPS AND ASSOCIATED FINAL STATES OBSERVED IN THE $^{181}Ta(\gamma,n)^{180}Ta$ REACTION

NEUTRON ENERGY (Kev)	Q-VALUE (Kev)	ASSIGNED FINAL STATE (KEV)
Aluminum E_γ = 7724 Kev		
145 ± 2	7528	0 ± 2
107 ± 1	7616	38 ± 2
37 ± 1	7687	109 ± 2
Aluminum E_γ = 7694 Kev		
80 ± 2	7614	38 ± 3
Copper E_γ = 7915 Kev		
333 ± 2	7580	0 ± 2
295 ± 1	7618	38 ± 2
225 ± 1	7688	109 ± 2
153 ± 1	7761	181 ± 2
103 ± 1	7811	231 ± 2
76 ± 1	7838	258 ± 2
25 ± 1	7889	309 ± 2

Photoneutron Q-Value

$$Q\{^{181}Ta(\gamma,n)^{180}Ta\} = 7579 \pm 2 \text{ Kev}$$

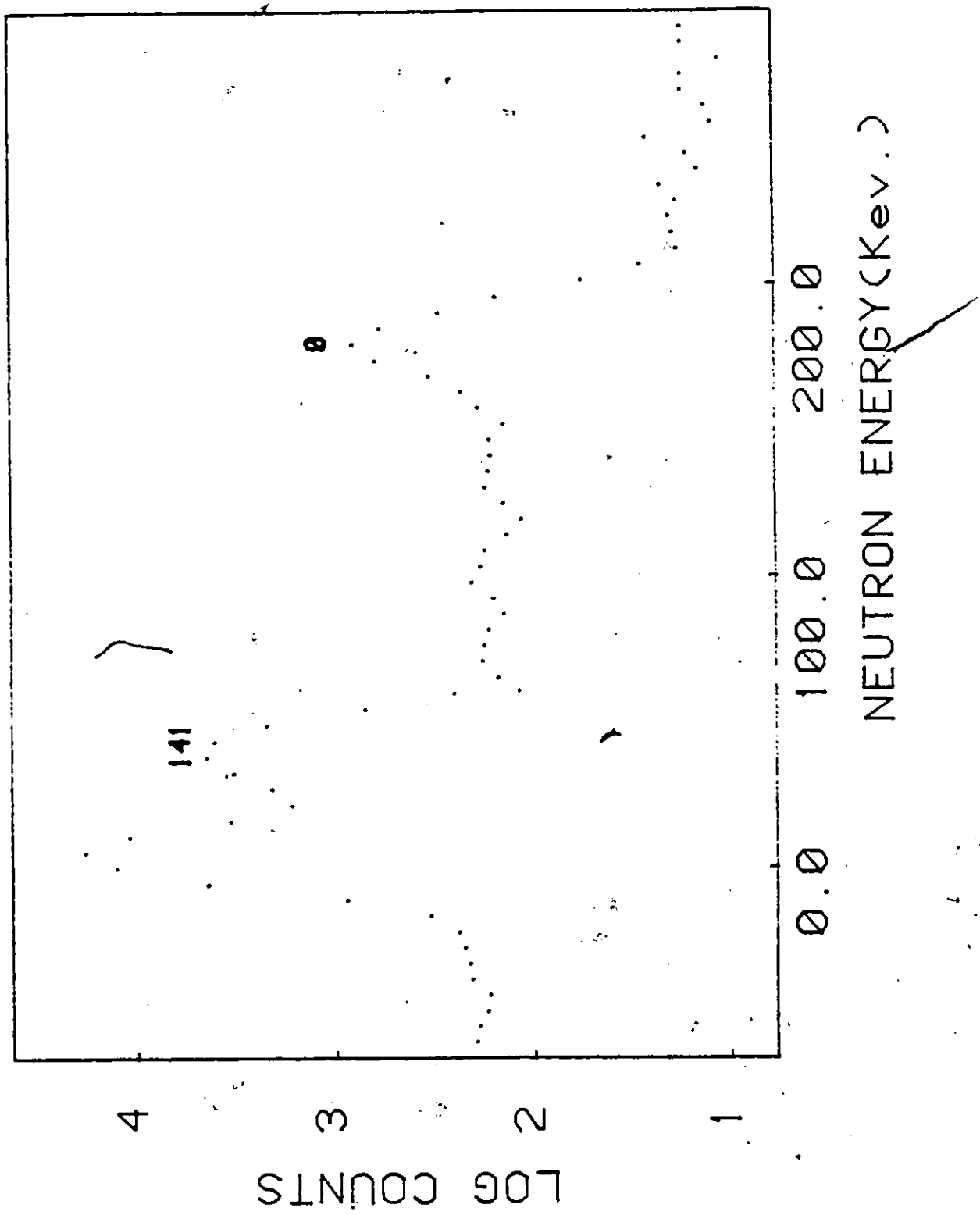

Figure 5.1 Photoneutron Spectrum from Aluminum (E_γ = 7724 Kev.) Source on Thallium. The numbers represent excited state energies.

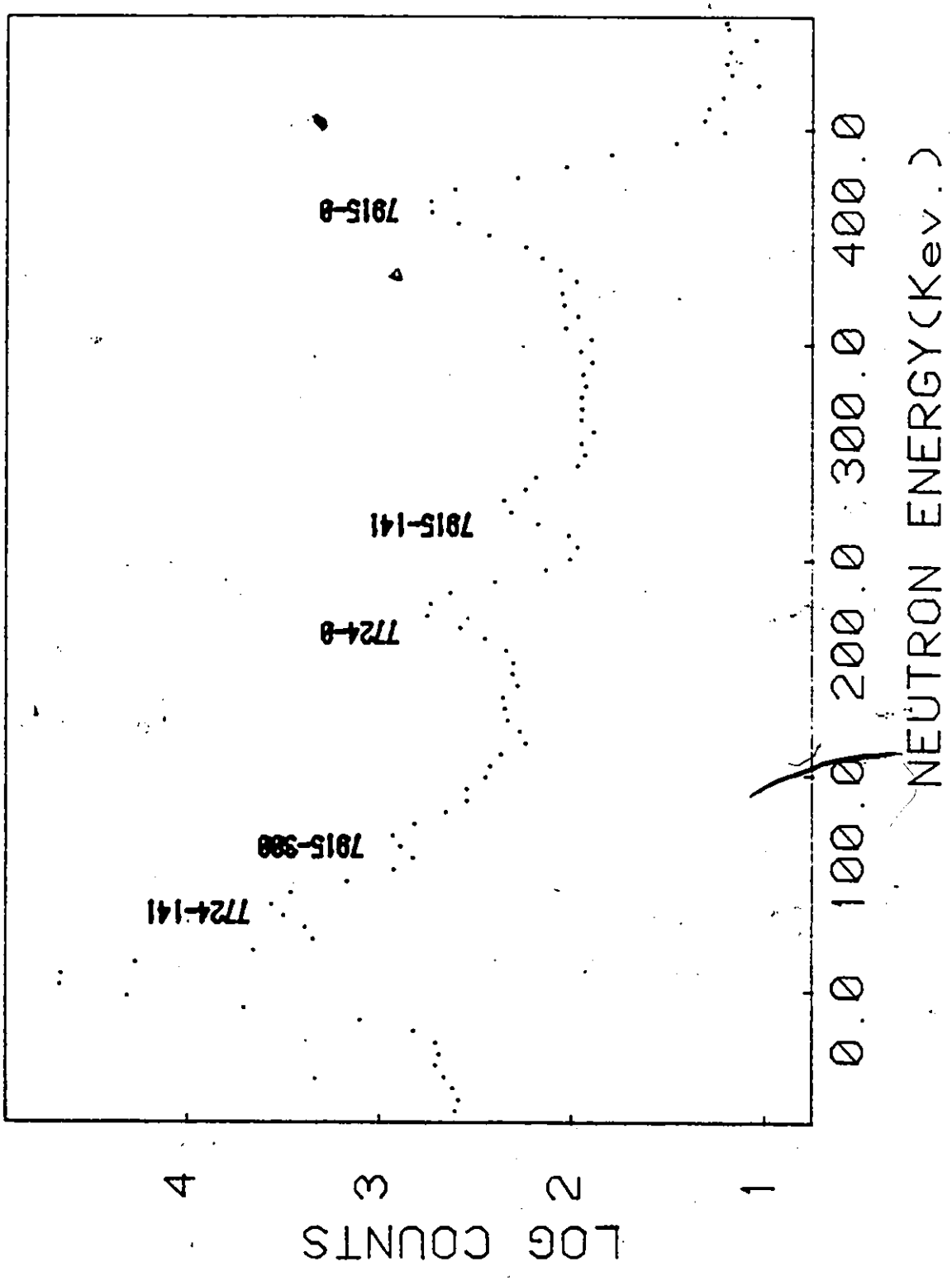

Figure 5.2 Photoneutron Spectrum from Copper (E_γ = 7915 Kev.) Source on Thallium

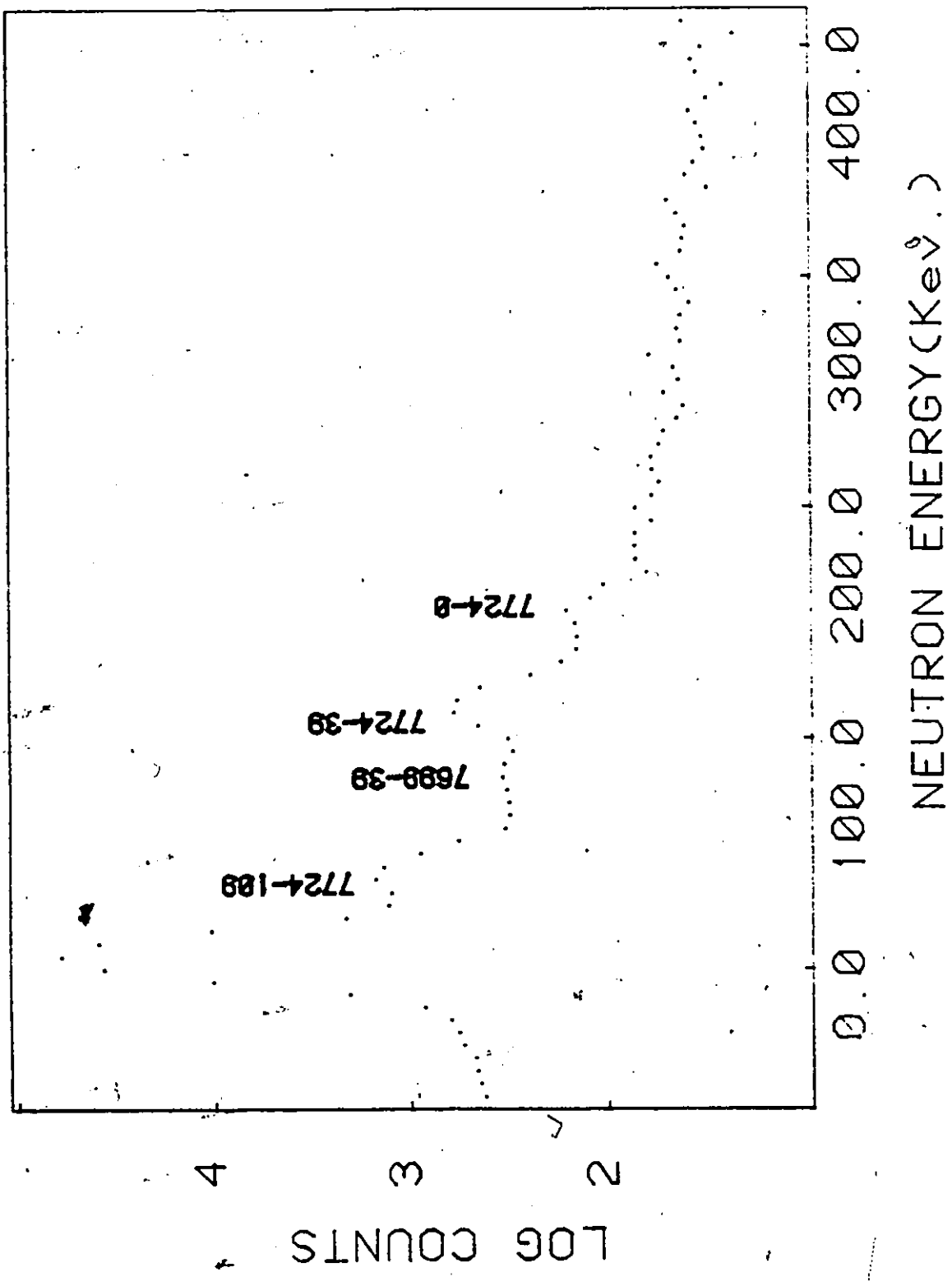

Figure 5.3 Photoneutron Spectrum from Aluminum Source on Tantalum. The first number is the γ ray energy, the second the excited state energy.

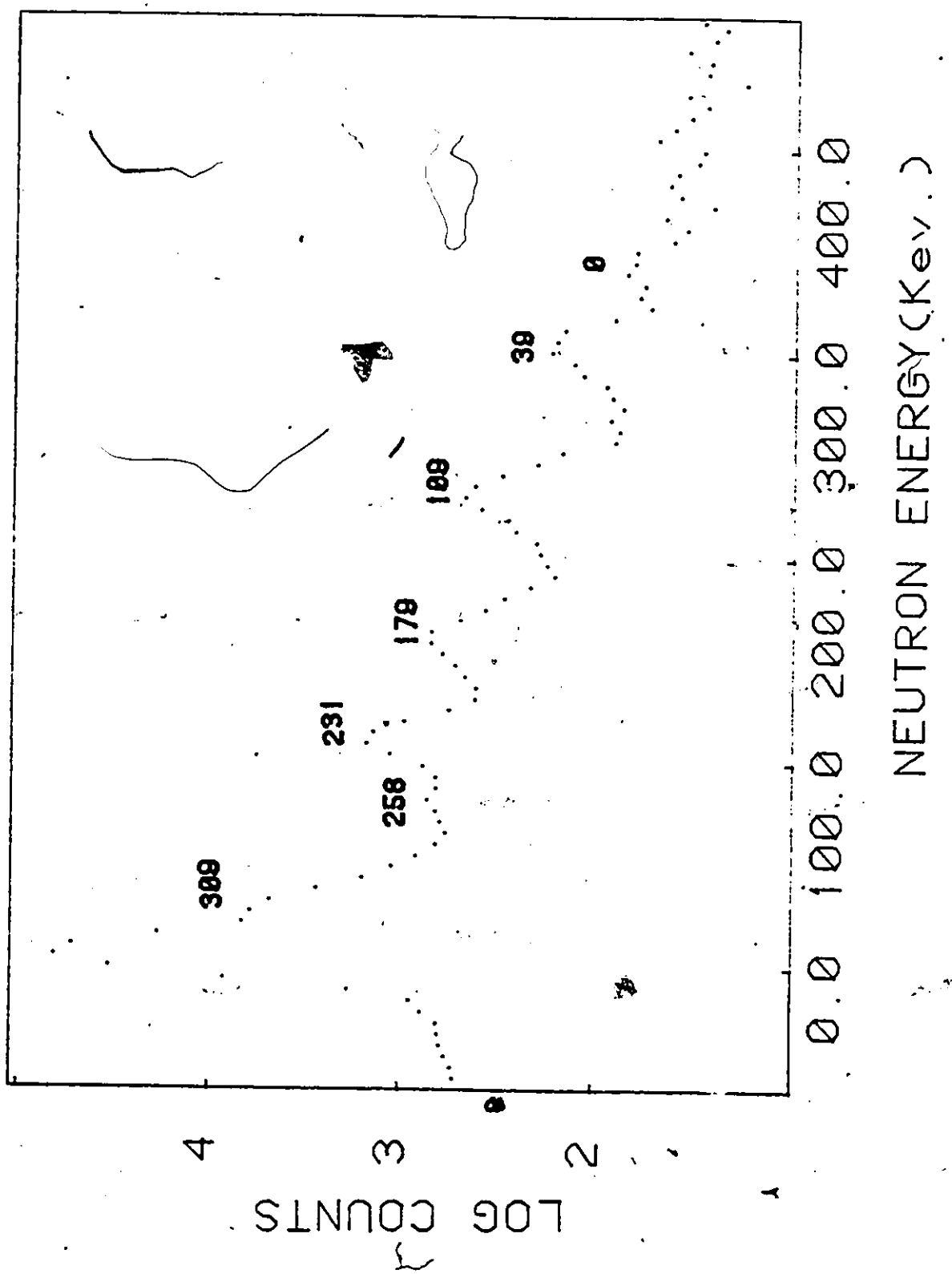

Figure 5.4 Photoneutron Spectrum from Copper (E_γ = 7915 Kev.) Source on Tantalum

transitions are also readily apparent in the spectrum arising from the copper source, since the aluminum γ ray from in core neutron capture on the fuel element grid makes a considerable contribution to the copper capture γ ray spectrum. The assigned excited state energy levels show excellent agreement with the level assignments of Lederer (Le 78) (see Fig. (1.1)), indicating the accuracy of the Q value. The value quoted here can be seen to be in agreement with McFee's (Mc 77) assignment of 7548 ± 3 Kev, but with much increased precision.

The case for the tantalum spectra does not lend itself to such simple interpretation. Here, since the energy levels are unknown, the procedure undertaken was to first assign possible Q-values to all observed neutron groups via the relation

$$Q = -\frac{A}{A-1} E_n + E_\gamma \qquad (5.1.1)$$

By inspection, the highest energy neutron group yields an average value of 7579 ± 2 Kev. This value is consistent with the work of Barkman (7580 ± 5 Kev, Ba 79) and Sharma (7593 ± 20 Kev, Sh 80) although again considerably more precise.

The determination of the photoneutron Q-value is of prime importance in the assignment of all nuclear energy levels, and the values quoted above were then used in analysis of the spectra produced by the nickel and chromium capture γ rays.

The thallium spectra will be discussed first, since for a variety of reasons they proved the easier to analyze. Figures (5.5) and (5.6) show the nickel and chromium source photoneutron spectra respectivley. Identification of all observed transitions is included here. This identification was accomplished by a quadratic fit of neutron energy to channel number using

$$E_n = \frac{A - 1}{A}(E_\gamma - Q - E_x) \qquad (5.1.2)$$

for the determination of neutron energy. In this manner energy identification of the transitions to low excitation energies ($E_x < 600$ Kev) initiated by the strongest intensity γ rays was made. These high energy neutron groups, together with the well defined thermal ($E_n = 0$) and aluminum (core) γ ray induced transitions previously mentioned proved adequate in each case for calibration. Thus a neutron energy was assigned to each observed group. This energy was then used to assign a transition to an excited state energy in ^{204}Tl for each possible γ ray energy via the equation

$$E_x = -\frac{A}{A - 1} E_n + E_\gamma - Q \qquad (5.1.3)$$

The results of such analysis are presented in Tables (5.3) and (5.4). From the tables, a photoneutron group was assigned as corresponding to a transition to a known level in ^{204}Tl if the possible excited state energy was within 1 Kev of the level energy listed in

TABLE 5.3

OBSERVED NEUTRON ENERGY GROUPS FROM NICKEL SOURCE ON ^{205}Tl

		POSSIBLE EXCITED STATE ASSIGNMENT (Kev) FOR EACH E_γ(Kev)				
NEUTRON ENERGY (Kev)	AREA	8999	8533	8121	7819	7724(Aℓ)
1442 ± 2	790 ± 40	-2 ± 2	-	-	-	-
1303 ± 2	829 ± 44	141 ± 2	-	-	-	-
1143 ± 2	680 ± 95	301 ± 3	-	-	-	-
1122 ± 2	795 ± 100	319 ± 3	-	-	-	-
1105 ± 2	448 ± 53	340 ± 2	-	-	-	-
1021 ± 1	883 ± 59	425 ± 2	-	-	-	-
980 ± 1	1299 ± 74	469 ± 2	0 ± 2	-	-	-
953 ± 1	1650 ± 75	491 ± 2	27 ± 2	-	-	-
910 ± 2	440 ± 61	537 ± 2	71 ± 2	-	-	-
840 ± 1	730 ± 68	607 ± 2	141 ± 2	-	-	-
823 ± 2	1145 ± 71	625 ± 2	159 ± 2	-	-	-
709 ± 2	525 ± 68	739 ± 2	273 ± 2	-	-	-
683 ± 1	963 ± 75	764 ± 2	298 ± 2	-	-	-
665 ± 1	654 ± 76	783 ± 2	317 ± 2	-	-	-
607 ± 1	204 ± 31	841 ± 2	375 ± 2	-	-	-
568 ± 1	660 ± 77	880 ± 2	414 ± 2	2 ± 2	-	-
550 ± 2	167 ± 79	898 ± 2	432 ± 2	20 ± 2	-	-
508 ± 1	1072 ± 54	940 ± 2	474 ± 2	62 ± 2	-	-
492 ± 2	287 ± 53	956 ± 2	490 ± 2	78 ± 2	-	-
446 ± 2	308 ± 52	1002 ± 2	536 ± 2	124 ± 2	-	-
434 ± 1	602 ± 74	1014 ± 2	548 ± 2	136 ± 2	-	-
398 ± 1	1562 ± 91	1050 ± 2	584 ± 2	172 ± 2	-	-
358 ± 1	630 ± 93	1091 ± 2	625 ± 2	213 ± 2	-	-
327 ± 1	1027 ± 99	1122 ± 2	656 ± 2	244 ± 2	-	-
271 ± 1	931 ± 107	1179 ± 2	713 ± 2	301 ± 2	-1 ± 2	-
229 ± 2	101 ± 39	1221 ± 2	755 ± 2	343 ± 2	41 ± 2	-
177 ± 1	1923 ± 206	1274 ± 1	808 ± 1	396 ± 1	94 ± 1	-1 ± 1
159 ± 1	968 ± 134	1292 ± 2	826 ± 2	414 ± 2	112 ± 2	17 ± 2
141 ± 2	329 ± 123	1310 ± 2	844 ± 2	432 ± 2	130 ± 2	35 ± 2
125 ± 3	299 ± 100	1325 ± 3	859 ± 3	447 ± 3	145 ± 3	50 ± 3
74 ± 1	3775 ± 183	1376 ± 2	910 ± 2	498 ± 2	196 ± 2	101 ± 2
35 ± 1	7815 ± 192	1417 ± 1	951 ± 1	539 ± 1	237 ± 1	142 ± 1

TABLE 5.4

OBSERVED NEUTRON GROUPS FROM CHROMIUM SOURCE ON ^{205}Tl

NEUTRON ENERGY (Kev)	AREA	POSSIBLE EXCITED STATE ASSIGNMENTS (Kev) FOR EACH E_γ(Kev)					
		9720	8884	8512	8485	7939	7724(Aℓ)
2162 ± 3	116 ± 24	0 ± 3	-	-	-	-	-
2018 ± 3	130 ± 25	144 ± 3	-	-	-	-	-
1858 ± 3	218 ± 39	305 ± 3	-	-	-	-	-
1823 ± 3	116 ± 26	339 ± 3	-	-	-	-	-
1743 ± 4	102 ± 22	419 ± 5	-	-	-	-	-
1691 ± 3	136 ± 25	472 ± 4	-	-	-	-	-
1671 ± 3	169 ± 26	493 ± 3	-	-	-	-	-
1632 ± 4	111 ± 23	531 ± 4	-	-	-	-	-
1539 ± 2	445 ± 31	625 ± 3	-	-	-	-	-
1423 ± 5	53 ± 26	741 ± 5	-	-	-	-	-
1332 ± 2	433 ± 36	834 ± 2	-2 ± 2	-	-	-	-
1190 ± 2	208 ± 36	975 ± 2	139 ± 2	-	-	-	-
1124 ± 3	115 ± 24	1042 ± 3	206 ± 3	-	-	-	-
1061 ± 4	35 ± 18	1106 ± 5	270 ± 5	-	-	-	-
1032 ± 2	909 ± 66	1134 ± 2	298 ± 2	-	-	-	-
1011 ± 1	1771 ± 70	1155 ± 2	319 ± 2	-	-	-	-
989 ± 2	596 ± 64	1178 ± 2	342 ± 2	-	-	-	-
916 ± 2	120 ± 58	1251 ± 2	415 ± 2	43 ± 2	15 ± 2	-	-
899 ± 2	702 ± 61	1269 ± 2	433 ± 2	61 ± 2	33 ± 2	-	-
861 ± 1	1955 ± 80	1306 ± 2	470 ± 2	98 ± 2	71 ± 2	-	-
838 ± 1	1595 ± 80	1329 ± 2	492 ± 2	121 ± 2	94 ± 2	-	-
797 ± 2	573 ± 69	1370 ± 2	534 ± 2	162 ± 2	135 ± 2	-	-
705 ± 2	1193 ± 76	1463 ± 2	627 ± 2	255 ± 2	228 ± 2	-	-
668 ± 2	338 ± 82	1501 ± 2	665 ± 2	297 ± 2	265 ± 2	-	-
642 ± 2	530 ± 82	1527 ± 2	691 ± 2	319 ± 2	291 ± 2	-	-
598 ± 2	512 ± 32	1570 ± 2	734 ± 2	362 ± 2	335 ± 2	-	-
573 ± 2	653 ± 84	1597 ± 2	761 ± 2	389 ± 2	361 ± 2	-	-
549 ± 2	664 ± 90	1620 ± 2	784 ± 2	412 ± 2	384 ± 2	-	-
431 ± 2	698 ± 80	1739 ± 2	903 ± 2	581 ± 2	503 ± 2	-	-
407 ± 2	387 ± 89	1763 ± 2	927 ± 2	555 ± 2	527 ± 2	-	-
347 ± 2	127 ± 59	1822 ± 2	986 ± 2	614 ± 2	587 ± 2	41 ± 2	-
287 ± 2	213 ± 93	1884 ± 3	1048 ± 3	676 ± 3	648 ± 3	103 ± 3	-
236 ± 2	214 ± 99	1935 ± 3	1099 ± 3	727 ± 3	699 ± 3	154 ± 3	-
212 ± 2	1089 ± 103	1959 ± 2	1123 ± 2	751 ± 2	723 ± 2	178 ± 2	-
177 ± 1	1937 ± 181	1994 ± 2	1158 ± 2	786 ± 2	758 ± 2	213 ± 2	-2 ± 2
123 ± 2	458 ± 101	2047 ± 2	1211 ± 2	839 ± 2	812 ± 2	266 ± 2	51 ± 2
89 ± 2	577 ± 113	2082 ± 2	1246 ± 2	874 ± 2	847 ± 2	301 ± 2	86 ± 2
72 ± 2	396 ± 123	2099 ± 2	1263 ± 2	891 ± 2	864 ± 2	318 ± 2	103 ± 2
35 ± 2	8321 ± 215	2136 ± 2	1300 ± 2	928 ± 2	901 ± 2	355 ± 2	140 ± 2

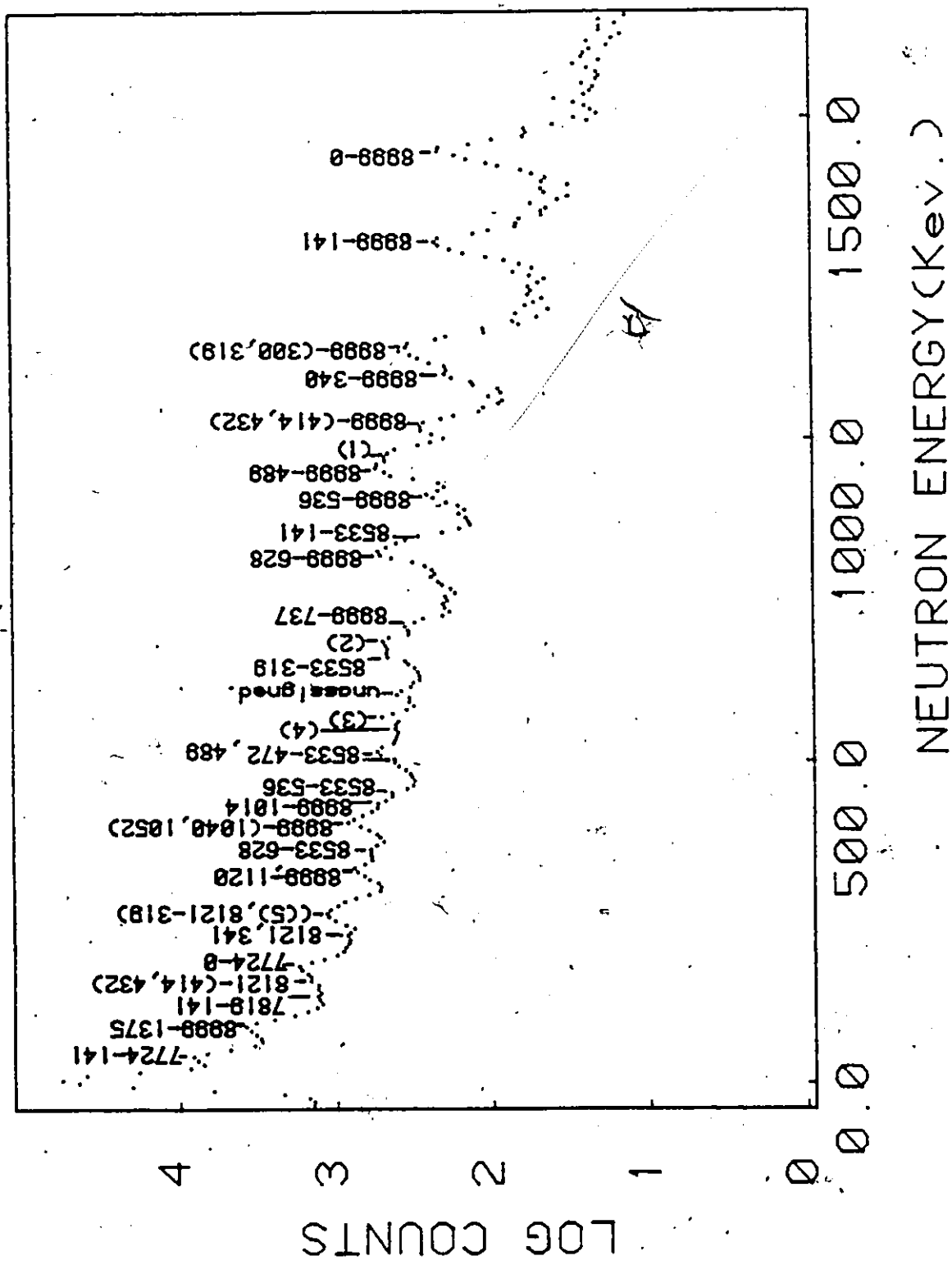

Figure 5.5 Photoneutron Spectrum from Nickel Source on Thallium

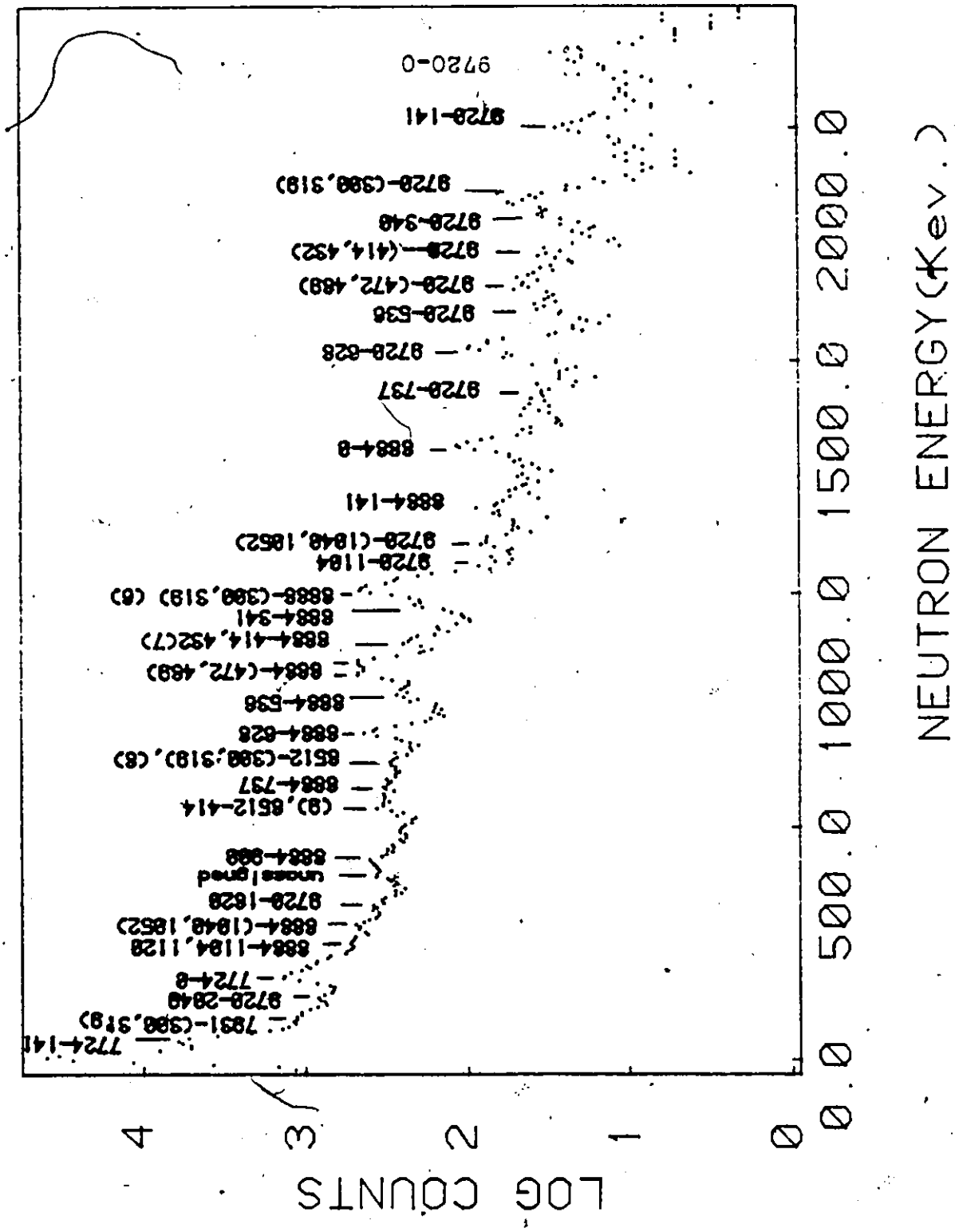

Figure 5.6 Photoneutron Spectrum from Chromium Source on Thallium

Fig. (1.1). This energy level uncertainty appears consistent with the results of experiments quoted by Lederer (Le 78).

Using this method, only two observed transitions could not be assigned as corresponding to energy levels in ^{204}Tl. These were the levels at 607 ± 1 Kev in the nickel spectrum at 407 ± 2 Kev in the chromium spectrum.

All other identified transitions are presented in Table (5.5). This table also includes the partial cross section for each transition based upon the results of section (5.6). In the table the bracketted numbers beside each cross section indicate where more than one energy level assignment is possible. The same number may correspond to two or more possible incident γ rays. The asterisks indicate levels which were too closely spaced and weakly populated to be resolved from each other.

Referring to Fig. (1.1) it is seen that for all levels under 1200 Kev, the tentative level assignments (dashed lines) of Lederer were not observed to be populated here. This would indicate either a non-favourable spin configuration or a clear non-existence.

Returning to the two neutron groups which did not correspond to known levels in ^{204}Tl, the logical assumption would be to assign these as being populated in the $^{203}Tl(\gamma,n)^{202}Tl$ reaction. Table (5.6) lists the possible excited state energy levels as derived from both Q-values

TABLE 5.5

LEVEL ASSIGNMENTS AND PARTIAL CROSS SECTION (mb) FOR $^{205}Tl(\gamma,n)^{204}Tl$ TRANSITIONS

EXCITED STATE ENERGIES (Kev)	7724	7819	7915	7939	8121	8485	8512	8533	8884	8999	9720
0	33.4 ±2.9	(3) 7.94 ±1.0	18.3 ±2.2		(3) 12.6 ±1.87			(1) 13.3 ±1.33	4.32 ±.53	5.54 ±.52	4.45 ±.99
141	55.2 ±4.7	3.18 ±.39	3.22 ±.37					7.27 ±.90	1.87 ±.37	5.30 ±.52	4.69 ±.99
300			8.19 ±.94	2.94 ±.60	(5) 20.7 ±2.6		(8) 9.47 ±2.40	(2) 8.94 ±1.01	(6) 7.21 ±.83	3.87 ±.62	7.27 ±1.91
319				1.72 ±.54	27.7 ±2.7		14.76 ±2.40	6.03 ±.86	13.85 ±1.35	4.46 ±.67	
340					2.06 ±1.18				4.22 ±.59	2.47 ±.36	3.82 ±.91
365											
414					15.4 ±2.3		18.0 ±2.60	(3) 5.92 ±.84	(7) .85 ±.42	2.07 ±.23	
432					4.90 ±1.85			(4) 1.49 ±.72	4.96 ±.62	2.46 ±.25	3.23 ±.75
472								9.43 ±.90	13.61 ±1.34	(1) 6.04 ±.60	4.18 ±.85
489								2.50 ±.51	11.02 ±1.13	7.69 ±.72	5.16 ±.90
536								2.61 ±.49	3.87 ±.58	2.03 ±.33	3.30 ±.74
573											
616											
628								4.84 ±.82	7.74 ±.85	5.11 ±.52	12.56 ±1.37

TABLE 5.5 (CONTINUED)

E_γ(Kev)

EXCITED STATE ENERGIES (Kev)	8884	8999	9720
737	3.21 ±.35	2.23 ±.34	1.40 ±.69
763	(9) 4.06 ±.64	(2) 3.61 ±.51	
900	4.06 ±.63	(4) .57 ±.29	
960			
1014		2.29 ±.34	
1040	1.02 ±.45	5.80 ±.58	2.45 ±.55
1052	1.02 ±.45	5.80 ±.58	2.45 ±.55
1104	.87 ±.41		.71 ±.31
1120	4.23 ±.55	3.42 ±.43	
1134			(6) 17.95 ±1.99
1203			
1251			(7) 2.19 ±0.32
1375		5.27 ±.50	
1393			

TABLE 5.5 (CONTINUED)

EXCITED STATE ENERGIES (Kev)	E_γ (Kev) 8884	8999	9720
1399			
1501			(8) 5.3 ±1.8
1522			
1741			(9) 10.5 ±1.4
1820			1.67 ±.79
2049			3.23 ±.76

TABLE 5.6

POSSIBLE ENERGY LEVEL ASSIGNMENTS IN $^{203}Tl(\gamma,n)^{202}Tl$ REACTION

SOURCE: NICKEL, E_n = 607 ± 1 Kev			
	Q = 7736 ± 3 Kev		Q = 7720 ± 20 Kev
E_γ (Kev)	E_x (Kev)	*Possible (Mev)	E_x (Kev)
8999	652 ± 3	.63	669 ± 20
8533	185 ± 3	.19	202 ± 20
SOURCE: CHROMIUM, E_n = 407 ± 2 Kev			
	Q = 7737 ± 3 Kev		Q = 7720 ± 20 Kev
E_γ (Kev)	E_x (Kev)	*Possible (Mev)	E_x (Kev)
9720	1574 ± 4	-	1590 ± 20
8884	738 ± 4	.72	754 ± 20
8512	365 ± 4	.35	382 ± 20
8485	338 ± 4	.35	356 ± 20

*Possible corresponding energy levels from Fig. 1.2

listed in Chapter 1. Possible accepted energy level assignments (Le 78) are also listed in the table. These levels were populated in the $^{203}Tl(p,d)^{202}Tl$ reaction, where the energy uncertainty of ± 20 Kev (Wa 71) makes positive assignment difficult. If the two strongest incident γ rays are accepted as those responsible for the population of the observed levels, then a rough Q-value of 7755 ± 20 Kev may be inferred.

The major difficulty in assigning the $^{203}Tl(\gamma,n)^{202}Tl$ Q value is the fact that the ground state transition is not observed. Any of the previously quoted Q-values would predict that this ground state transition should occur with neutron energy corresponding to the range between the 141 Kev and 300 Kev transitions from the $^{205}Tl(\gamma,n)^{204}Tl$ reaction. Observation yields nothing in this range.

The lack of evidence for the ground state transition may have implications regarding the spin of this level. The decay from ^{202m}Pb predicts a ground state spin and parity of 2^-, while the $^{203}Tl(p,d)^{202}Tl$ reaction indicates a spin of either 1 or 3, with no indication of parity. A 2^- state may be populated by s-wave emission, which would carry the highest neutron penetrability factor, and so should have the largest cross section. If the parity of the ground state is assumed negative, a 1^- state or a 3^- state may be reached by s and d wave emission respectively. Positive parity assumption requires p and f wave emission for the two cases. All quoted transitions have assumed E1 incident photon multipolarity. The fact that the ground state

transition is not observed may indicate a 3^+ (or 3^-) ground state and correspondingly low neutron penetrabilities. The higher energy excited state transitions in ^{202}Tl may be obscurred by the $^{205}Tl(\gamma,n)^{204}Tl$ transitions because of the lower isotopic abundance of ^{203}Tl.

Since the methodology had been shown to be reliable in the determination of the energy levels in ^{204}Tl, the same procedure was used to examine the energy levels ^{180}Ta. The energy calibration here proved more difficult since the only well-established levels were taken as those populated in the aluminum and copper photoneutron spectra - a total of seven.

Tables (5.7) and (5.8) give the neutron energies and possible level assignments thus derived. Table (5.9) gives the final energy level assignments together with the cross section for population of each level. The right hand column of this table lists the weighted values of the energy level assignments, and as such represents the proposed energy level scheme for ^{180}Ta. The letters beside the individual excited states indicate again where more than one possible excited state assignment is possible due to more than one possible gamma ray initiation. The nickel and chromium photoneutron spectra on tantalum are shown with all level assignments included in Figs. (5.7) and (5.8).

The level density of the low-lying states in ^{180}Ta may be calculated from the tables. The average level spacing is approximately

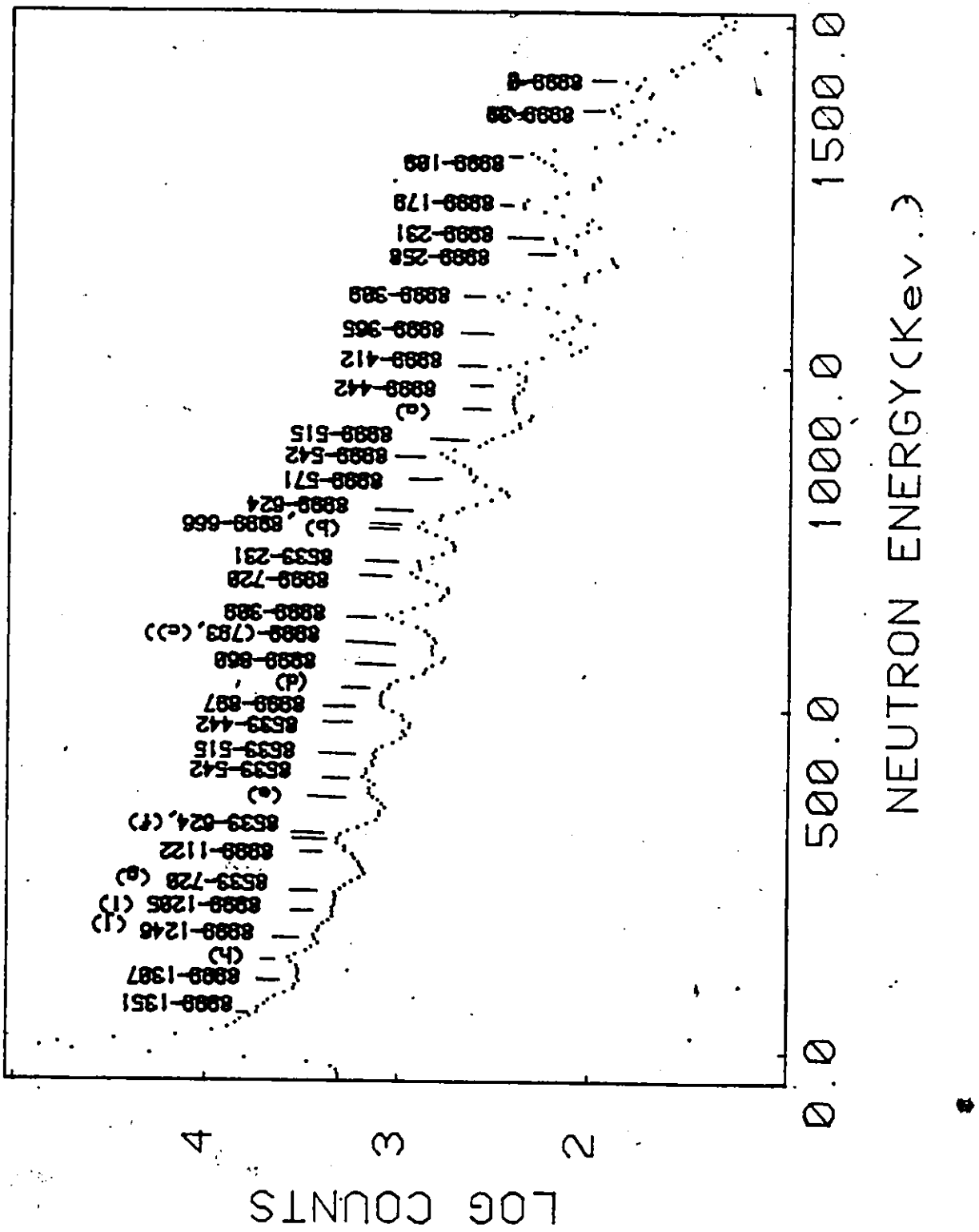

Figure 5.7 Photoneutron Spectrum from Nickel Source on Tantalum

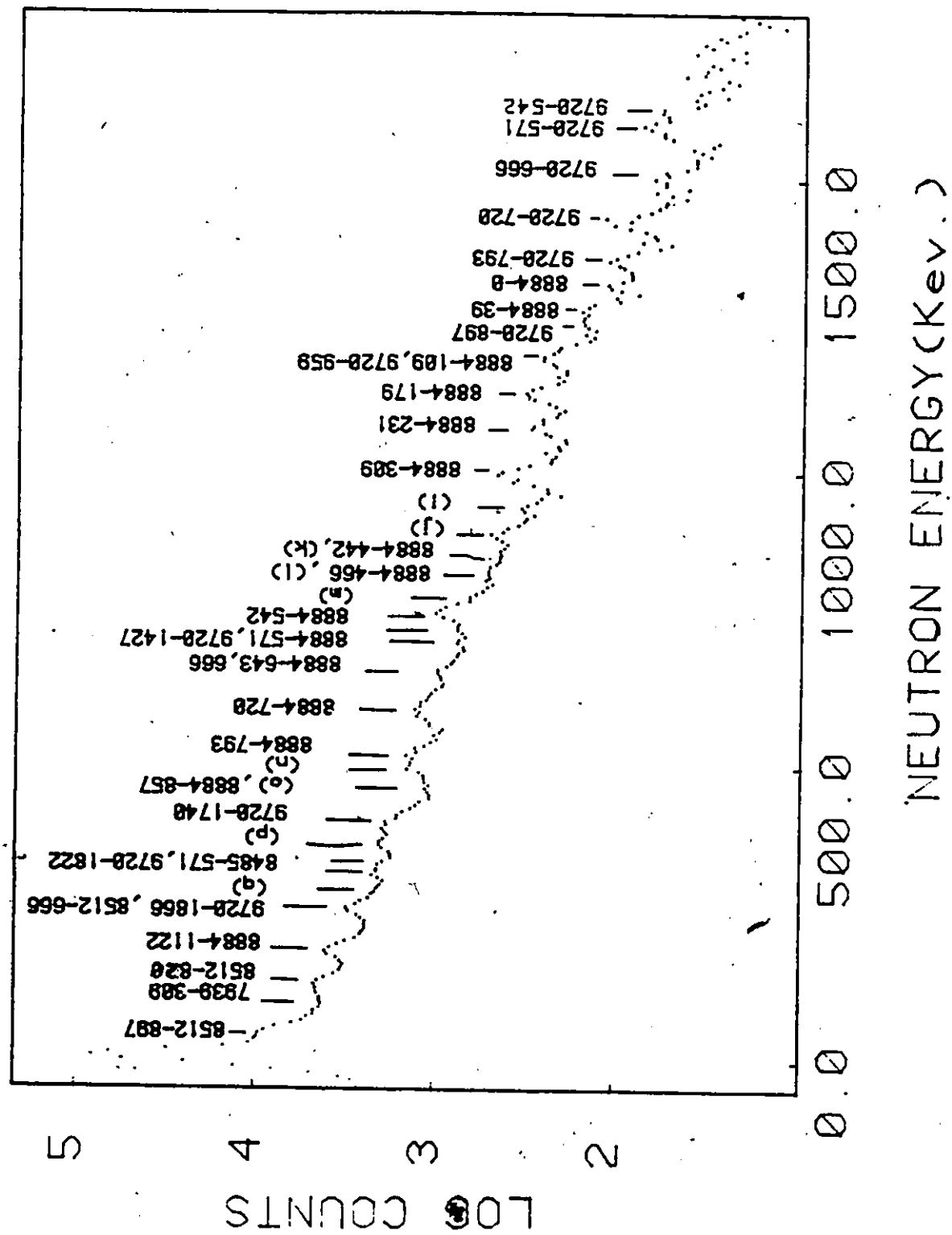

Figure 5.8 Photoneutron Spectrum from Chomium Source on Tantalum

TABLE 5.7

OBSERVED NEUTRON ENERGY GROUPS FROM NICKEL SOURCE ON TANTALUM

NEUTRON ENERGY (Kev)	AREA	POSSIBLE EXCITED STATE ASSIGNMENT E_γ(Kev)			
		8999	8533	8121	7819
1412 ± 2	197 ± 32	0 ± 3	-	-	-
1372 ± 2	209 ± 35	40 ± 3	-	-	-
1303 ± 2	750 ± 48	110 ± 3	-	-	-
1236 ± 2	869 ± 51	177 ± 3	-	-	-
1181 ± 2	411 ± 45	232 ± 3	-	-	-
1155 ± 3	53 ± 23	259 ± 4	-	-	-
1104 ± 1	1026 ± 57	310 ± 2	-	-	-
1049 ± 2	318 ± 40	365 ± 3	-	-	-
1000 ± 2	656 ± 63	414 ± 3	-	-	-
973 ± 2	256 ± 68	442 ± 3	-	-	-
951 ± 2	315 ± 69	464 ± 3	-2 ± 3	-	-
901 ± 2	387 ± 80	514 ± 3	48 ± 3	-	-
875 ± 1	1756 ± 86	540 ± 2	74 ± 3	-	-
846 ± 1	864 ± 85	569 ± 2	103 ± 2	-	-
798 ± 1	905 ± 95	622 ± 2	152 ± 2	-	-
772 ± 1	2111 ± 102	644 ± 2	178 ± 2	-	-
753 ± 1	727 ± 105	667 ± 2	197 ± 2	-	-
719 ± 1	1747 ± 111	705 ± 2	281 ± 2	-	-
697 ± 1	1934 ± 115	719 ± 2	253 ± 2	-	-
640 ± 1	3237 ± 112	776 ± 2	310 ± 2	-	-
620 ± 2	672 ± 111	797 ± 3	331 ± 3	-	-
597 ± 2	520 ± 104	820 ± 3	361 ± 3	-	-
557 ± 2	395 ± 92	860 ± 3	394 ± 3	-	-
538 ± 2	610 ± 82	879 ± 3	413 ± 3	1 ± 3	-
520 ± 1	1488 ± 132	897 ± 2	431 ± 2	19 ± 2	-
508 ± 2	1289 ± 132	909 ± 3	443 ± 3	31 ± 3	-
439 ± 1	1867 ± 143	979 ± 2	514 ± 2	101 ± 2	-
411 ± 1	1903 ± 149	1007 ± 2	542 ± 2	129 ± 2	-
382 ± 1	1110 ± 150	1036 ± 2	573 ± 2	158 ± 2	-
327 ± 2	1337 ± 166	1091 ± 3	626 ± 3	213 ± 3	-
311 ± 1	2495 ± 170	1107 ± 2	642 ± 2	229 ± 2	-
292 ± 1	1533 ± 131	1126 ± 2	661 ± 2	248 ± 2	-
235 ± 1	1185 ± 177	1184 ± 2	719 ± 2	306 ± 2	4 ± 2
214 ± 1	513 ± 184	1205 ± 2	740 ± 2	327 ± 2	25 ± 2
173 ± 2	963 ± 100	1246 ± 2	781 ± 3	368 ± 3	66 ± 3
134 ± 1	2855 ± 212	1285 ± 2	820 ± 2	407 ± 2	105 ± 2
110 ± 1	800 ± 189	1309 ± 2	844 ± 2	431 ± 2	129 ± 2
69 ± 2	1092 ± 240	1351 ± 3	886 ± 3	473 ± 3	171 ± 3

TABLE 5.8

OBSERVED NEUTRON ENERGY GROUPS FROM CHROMIUM SOURCE ON TANTALUM

		POSSIBLE EXCITED STATE ASSIGNMENTS E_γ (Kev)				
NEUTRON ENERGY (Kev)	AREA	9720	8884	8512	8484	7939
1585 ± 5	116 ± 41	547 ± 5	-	-	-	-
1558 ± 3	167 ± 43	574 ± 4	-	-	-	-
1473 ± 5	107 ± 31	660 ± 5	-	-	-	-
1408 ± 5	252 ± 35	725 ± 5	-	-	-	-
1342 ± 3	159 ± 39	792 ± 4	-	-	-	-
1308 ± 3	101 ± 42	826 ± 4	-3 ± 4	-	-	-
1257 ± 3	209 ± 49	827 ± 4	41 ± 4	-	-	-
1238 ± 5	183 ± 47	896 ± 5	60 ± 5	-	-	-
1189 ± 2	360 ± 59	945 ± 3	109 ± 3	-	-	-
1175 ± 2	420 ± 58	959 ± 3	123 ± 3	-	-	-
1121 ± 2	807 ± 67	1014 ± 3	178 ± 3	-	-	-
1069 ± 2	532 ± 68	1066 ± 3	230 ± 3	-	-	-
989 ± 2	994 ± 78	1147 ± 3	311 ± 3	-	-	-
932 ± 2	271 ± 51	1204 ± 3	368 ± 3	-4 ± 3	-	-
888 ± 2	610 ± 82	1248 ± 3	412 ± 3	40 ± 3	13 ± 7	-
858 ± 2	251 ± 85	1278 ± 3	442 ± 3	70 ± 3	43 ± 3	-
832 ± 3	367 ± 91	1304 ± 4	468 ± 4	96 ± 4	69 ± 4	-
786 ± 3	215 ± 80	1351 ± 3	515 ± 3	143 ± 3	116 ± 3	-
757 ± 2	1754 ± 112	1380 ± 3	544 ± 3	172 ± 3	145 ± 3	-
733 ± 2	414 ± 114	1404 ± 3	568 ± 3	196 ± 3	169 ± 3	-
710 ± 3	111 ± 32	1427 ± 4	591 ± 4	219 ± 4	192 ± 4	-
659 ± 2	520 ± 123	1478 ± 3	642 ± 3	270 ± 3	243 ± 3	-
639 ± 2	412 ± 31	1498 ± 3	662 ± 3	290 ± 3	263 ± 3	-
579 ± 2	1104 ± 136	1559 ± 3	723 ± 3	351 ± 3	324 ± 3	-
511 ± 2	1329 ± 143	1627 ± 3	791 ± 3	419 ± 3	392 ± 3	-
489 ± 2	862 ± 142	1649 ± 3	813 ± 3	441 ± 3	414 ± 3	-
460 ± 3	200 ± 45	1678 ± 4	842 ± 4	470 ± 4	443 ± 4	-
449 ± 2	212 ± 42	1696 ± 3	854 ± 3	483 ± 3	455 ± 3	-
399 ± 2	801 ± 41	1740 ± 3	904 ± 3	532 ± 3	505 ± 3	-
359 ± 2	1000 ± 176	1780 ± 3	944 ± 3	572 ± 3	545 ± 3	-
334 ± 2	832 ± 182	1805 ± 3	969 ± 3	597 ± 3	570 ± 3	24 ± 3
317 ± 2	880 ± 200	1822 ± 3	986 ± 3	614 ± 3	507 ± 3	41 ± 3
283 ± 2	483 ± 197	1856 ± 3	1020 ± 3	648 ± 3	621 ± 3	75 ± 3
267 ± 2	545 ± 206	1873 ± 3	1037 ± 3	665 ± 3	638 ± 3	92 ± 3
254 ± 2	1732 ± 176	1886 ± 3	1050 ± 3	678 ± 3	651 ± 3	105 ± 3
240 ± 2	370 ± 213	1900 ± 3	1064 ± 3	692 ± 3	665 ± 3	119 ± 3
184 ± 2	4536 ± 242	1956 ± 3	1120 ± 3	748 ± 3	721 ± 3	175 ± 3
112 ± 2	1705 ± 238	2028 ± 3	1192 ± 3	820 ± 3	793 ± 3	247 ± 3
73 ± 2	812 ± 91	2068 ± 3	1232 ± 3	860 ± 3	833 ± 3	287 ± 3
51 ± 2	418 ± 58	2090 ± 3	1254 ± 3	882 ± 3	855 ± 3	309 ± 3
36 ± 2	1570 ± 157	2105 ± 3	1269 ± 3	897 ± 3	870 ± 3	324 ± 3

TABLE 5.9

ASSIGNED ENERGY LEVELS AND CROSS SECTIONS FOR $^{181}Ta(\gamma,n)^{180}Ta$ TRANSITIONS

(Under 400 Kev)

E_γ (Kev)

ASSIGNED EXCITED STATE ENERGY AND CROSS SECTION (mb)

7724	7915	7939	8121	8485	8512	8533	8884	8999	9720	WEIGHTED AVERAGE OF ENERGY LEVELS
0±2 (0.21 ±.03)	0±2 (0.13 ±.03)		(d) 1±3 (36.3 ±7.4)			(a) -2±3 (1.41 ±.15)	-3±4 (.35 ±.15)	0±3 (.64 ±.12)		0 ± 2
38±2 (2.23 ±.20)	39±2 (0.83 ±.09)	41±3 (3.26 ±.87)		(k) 43±3 (3.14 ±.8)	(i) 40±3 (6.56 ±.81)		41±4 (.71 ±.18)	40±3 (.83 ±.13)		39 ± 2
109±2 (2.24 ±.14)	109±2 (1.97 ± .21						109±3 (1.17 ±.21)	110±3 (2.28 ±.24)		109 ± 2
	181±2 (2.10 ±.22					(b) 178±2 (9.59 ±.91)	178±3 (2.47 ±.30)	177±3 (2.52 ±.24)		179 ± 2
	231±2 (3.37 ±.34)		(f) 229±2 (43.6 ±4.4)			231±2 (7.76 ±.80)	230±3 (1.56 ±.24)	232±3 (1.14 ±.16)		231 ± 2
	258±2 (0.29 ±.04)							259±4 (.14 ±.08)		258 ± 2
	309±2 (4.27 ±.44)	309±3 (.51 ±.08)				310±2 (13.9 ±1.2)	311±3 (2.52 ±.30)	310±2 (2.69 ±.26)		309 ± 2
						(c) 361±3 (2.23 ±.44)	(i) 368±3 (0.68 ±.11)	365±3 (0.83 ±.10)		365 ± 3

TABLE 5.9 (CONTINUED)

(Over 400 Kev)

ASSIGNED EXCITED STATE ENERGY AND CROSS SECTION (mb)

8485	8512	8533	8884	8999	9720	WEIGHTED AVERAGE OF ENERGY LEVELS
(n) 414 ± 3 (7.34 ±1.8)		(d) 413 ± 3 (6.73 ±.76)	(j) 412 ± 3 (1.54 ±.25)	414 ± 3 (1.57 ±.19)		412 ± 2
(o) 443 ± 4 (1.69 ±.6)	(n) 441 ± 3 (5.41 ±1.3)	443 ± 3 (5.34 ± .70)	(k) 442 ± 3 (.62 ±.22)	442 ± 3 (.57 ±.16)		442 ± 2
	(o) 470 ± 4 (1.25 ±.4)		468 ± 4 (.91 ±.23)	(a) 464 ± 3 (.69 ±.16)		466 ± 3
		514 ± 2 (7.42 ±.83)	(m) 515 ± 3 (.52 ±.20)	514 ± 3 (.85 ±.19)		515 ± 3
(p) 545 ± 3 (11.2 ±2.1)		542 ± 2 (7.38 ±.83)	544 ± 3 (4.17 ±.46)	540 ± 2 (3.82 ±.36)	547 ± 5 (1.22 ±.44)	542 ± 2
570 ± 3 (8.94 ±1.0)	(p) 572 ± 3 (8.28 ±0.7)	(e) 573 ± 2 (4.17 ±.66)	568 ± 3 (.97 ±.28)	569 ± 2 (1.85 ±.24)	574 ± 4 (1.72 ±.47)	571 ± 2
(q) 621 ± 3 (4.67 ±1.9)		626 ± 3 (4.64 ±.68		622 ± 2 (1.90 ±.25)		624 ± 2
	648 ± 3 (3.51 ±.8)	(f) 642 ± 2 (8.36 ±.89)	642 ± 3 (1.19 ±.30)	(b) 644 ± 2 (4.39 ±.42)		643 ± 2
	665 ± 3 (3.75 ±1.3)		662 ± 3 (.95 ±.21)	667 ± 2 (1.50 ±.25)	660 ± 5 (1.04 ±.31)	666 ± 3

TABLE 5.9 (CONTINUED)

ASSIGNED EXCITED STATE ENERGY AND CROSS SECTION (mb)

8485	8512	8533	8884	8999	9720	WEIGHTED AVERAGE OF ENERGY LEVELS
		(g) 719 ± 2 (3.30 ±.56)	723 ± 3 (2.47 ±.37)	719 ± 2 (3.89 ±.39)	725 ± 5 (2.38 ±.38)	720 ± 2
793 ± 3 (6.91 ±1.41)			791 ± 3 (2.90 ±.41)	797 ± 3 (1.32 ±.24)	792 ± 4 (1.43 ±.37)	793 ± 2
		(l) 820 ± 2 (5.76 ±.61)		(c) 820 ± 3 (1.01 ±.29)		820 ± 2
	860 ± 3 (4.24 ±.83)		854 ± 3 (.44 ±.09)	860 ± 3 (.76 ±.18)		857 ± 2
	897 ± 3 (5.14 ±1.61)			897 ± 2 (2.83 ±.34)	896 ± 5 (1.53 ±.41)	897 ± 3
					959 ± 3 (3.66 ±.54)	959 ± 3
			1120 ± 3 (5.71 ±.60)	1126 ± 2 (2.28 ±.27)		1122 ± 2
				1205 ± 2 (.62 ±.22)	(i) 1204 ± 3 (1.73 ±.36)	1205 ± 2
				1246 ± 3 (1.1 ±.14)	(j) 1248 ± 3 (3.14 ±.41)	1246 ± 3

TABLE 5.9 (CONTINUED)

ASSIGNED EXCITED STATE ENERGY AND CROSS SECTION (mb)

8485	8512	8533	8884	8999	9720	WEIGHTED AVERAGE OF ENERGY LEVELS
				1309 ± 2 (.69 ±.16)	1304 ± 21 (2.26 ±.59)	1307 ± 2
				1351 ± 3 (.62 ±.16)	1351 ± 3 (1.35 ±.21)	1351 ± 2
					1427 ± 4 (.64 ±.19)	1427 ± 4
					1740 ± 3 (4.17 ±.46)	1740 ± 3
					8122 ± 3 (1.95 ±.25)	1822 ± 3
					1866 ± 3 (6.74 ±.75)	1866 ± 3

45.4 Kev for $E_x < 500$ Kev, and 43.4 Kev for $E_x < 1000$ Kev. These are somewhat smaller than the average spacings in ^{204}Tl of 62.5 Kev for $E_x < 500$ kev, and 71.4 Kev for $E_x < 1000$ Kev. The ^{180}Ta level spacing is however comparable to the observed spacings in other odd-odd nuclei in the same mass region. For example, in ^{182}Ta this spacing is approximately 45.7 Kev for $E_x < 500$ Kev, while ^{176}Ta shows an average spacing of approximately 47.8 Kev for $E_x < 200$ Kev (Le 78).

Clearly such high level densities will result in greater chance of the same neutron energy group being able to be populated by different photon energies. Even more important, however, is the increased chance of weakly populated levels being obscured by other nearly more strongly populated levels. This may be viewed as the reason that for the 9720 transitions a total of only 5 (or roughly 1 per 200 Kev) energy levels are observed for $E_x > 1351$ Kev. This effect has already been observed in the ^{204}Tl energy levels, where, for $E_x > 1200$ Kev, the 9720 Kev γ ray was not observed to populate some accepted levels. Thus some excited states in ^{180}Ta with $E_x > 1$ Mev may not observed because of chance overlap with an already observed energy level populated by another γ ray.

5.2 The $^{180}Ta(n,\gamma)^{181}Ta$ Reaction

From analysis of the results of the $^{180}Ta(n,\gamma)^{181}Ta$ reaction, the energies and relative intensities determined for transitions in the

region of 6 to 7 Mev associated with tantalum are given in Table (5.10). The resolution obtained expressed as full width half maximum was 3.8 Kev in the region of 7 Mev. The standard deviation in peak centroids contributes an uncertainty of approximately 0.2 Kev to the transition energy. When combined with the uncertainty in calibration, we estimate the standard deviation in the energy should be no greater than 0.5 Kev. The error in relative intensity is based on the uncertainty in peak area. Also shown in the table are the energies of those final states which have been independently observed in other reactions (Le 78). For completeness, also included are transitions corresponding to the $^{181}Ta(n,\gamma)^{182}Ta$ reaction. The Q value here is in excellent agreement with the value of 6062.9 ± 0.5 Kev reported by Helmer and Greenwood (He 71).

Identification of the $J^{\pi} = 15/2^{+}$ level at 716.59 Kev as the final state for the 6935.26 Kev gamma ray in the $^{180}Ta(n,\gamma)^{181}Ta$ reaction is based upon the available mass data (Sh 80), which requires a total energy release of 7693 ± 2 Kev. The energy difference between the 6935.26 Kev gamma ray and the 6112.25 Kev gamma ray is in excellent agreement with the energy difference between the $J^{\pi} = 15/2^{+}$ level and the $J^{\pi} = 21/2^{+}$ level at 1539.7 Kev. Both these levels have been identified in Coulomb excitation studies (Le 78). The intensity of the $^{181}Ta(n,\gamma)^{182}Ta$ ground state transition is given as 0.43% (Ra 67), while the thermal cross section for this reaction is 21.0 barns (BNL 325). The partial cross section for this transition is thus 90 mb. From the relative intensity and isotopic abundance, the partial cross section for the $^{180}Ta(n,\gamma)^{181}Ta$ transition to the $J^{\pi} = 15/2^{+}$ state is

TABLE 5.10

ENERGIES AND RELATIVE INTENSITIES OF TANTALUM CAPTURE GAMMA-RAYS

ENERGY (Kev) (STANDARD DEVIATION = 0.5 Kev)	RELATIVE INTENSITY (10% UNCERTAINTY)	CAPTURE ISOTOPE	FINAL STATE ENERGY* (Kev)	FINAL STATE SPIN AND PARITY
5965.29	100	181	97.8	4^-
6062.90	60	181	0	3^-
6097.58	86	180		
6112.25	38	180	1539.7	$21/2^+$
6180.67	54	180		
6420.00	33	180		
6935.26	36	180	716.59	$15/2^+$

*From Le (78)

Q-values

$^{181}Ta(n,\gamma)^{182}Ta$ 6063.3 ± 0.5 Kev
$^{180}Ta(n,\gamma)^{181}Ta$ 7652.3 ± 0.5 Kev

estimated to be 1.3 barns. For a total cross section of 700 ± 200 b (BNL 325) this would imply an absolute intensity of approximately 0.2%. The relative intensities of the five transitions observed for this reaction are comparable, indicating they are most probably dipole transitions. If one assumes s-wave capture, the maximum angular momentum transfer in this reaction for these transitions would be 3/2. This would imply that the target spin is 9 and that the capture contains significant contributions from both J = 17/2 and 19/2 resonances in order to populate with comparable intensity both J^{π} = $15/2^+$ and $21/2^+$ final states. The only resonance reported is at 0.433 ev (Ev 55). We calculate from the resonance parameters quoted that it would account for only some ten to fifteen percent of the thermal cross section.

It is most likely that the transitions observed are electric dipole since these are generally the strongest transitions. In this case the target state will be $J^{\pi} = 9^-$, and could result from the coupling of a [514] $9/2^-$ proton to a [624]$9/2^+$ neutron as has previously been suggested (Wa 79). The [514]$9/2^-$ proton state has been identified as the first excited state at 6 Kev in ^{181}Ta, while the [624]$9/2^+$ neutron state is the ground state of ^{181}W. It must be emphasized however that it is not possible to exclude the possibility that the observed transitions are magnetic dipole in character. It is difficult to see how a $J^{\pi} = 9^+$ state could be formed simply from the available low-lying single-particle states however.

Decay of the 9^- state would have to take place by electron capture to the 641 Kev state with $J^\pi = 6^+$ in ^{180}Hf, for which the Q-value is 287 Kev, or by negatron decay to the 688 Kev, $J^\pi = 6^+$ state of ^{180}W with a Q-value of 105 Kev. The transitions would be third forbidden for which the value of logft is expected to be about 18 (Pr 62). The lower limit of 10^{13} years indicates the value to be greater than 20. This higher value would be consistent with the fact that the decay corresponds to a transition from a state with K = 9 to one with K = 0.

From the results of the previous section (Q = 7579 ± 2 Kev) the 10^{13} year state is located at 73 ± 2 Kev above the ground state in ^{180}Ta. It should be noted that this naturally occurring isomer is never viewed directly in the photoneutron reactions reported here. This is consistent with a spin assignment of 9^-, since following E1 photon absorption in the $7/2^+$ target ^{181}Ta nucleus, the isomeric state may be populated only by the emission of g-wave ($\ell = 4$) neutrons for which the penetrability is vanishingly small especially at low energies (see Chapter 2).

5.3 Comparison of ^{180}Ta Levels Scheme with other Experimenters

The low energy level structure derived here is compared with the results of a previous study of the $^{181}Ta(p,d)^{180}Ta$ reaction (Wa 79) in Table (5.11). The spin and parity of the states suggested by this author is also listed. Five of the states observed in this work

TABLE 5.11

COMPARISON OF LOW ENERGY LEVELS POPULATED IN THE $^{181}Ta(\gamma,n)^{180}Ta$ REACTION WITH THOSE FROM THE $^{181}Ta(p,d)^{180}Ta$ REACTION

LEVEL ENERGY (Kev)		J^{π}(From (Wa 79))
(γ,n)	(p,d)	
0	0	1^+
39(2)	41	2^+
*73(2)		9^-
109(2)	106	3^+
179(2)	173	4^+, 8^+
231(2)		
258(2)		
309(2)	302	5^+

* This level is inferred from the difference in (n,γ) and (γ,n) Q-values, and is not observed directly in the photoneutron reaction.

correspond well with levels populated in the neutron pick-up process. There are two additional states at 231 and 259 Kev which are populated in the photoneutron reaction.

The relation between Warde's spin assignments and the individual photoneutron cross sections will be discussed more fully in the following sections.

The spins quoted by Warde indicate that there are a pair of closely spaced levels at 173 Kev, with spins and parities $J^{\pi} = 4^{+}$ and 8^{+}. In the photoneutron experiment the $J^{\pi} = 4^{+}$ member may be populated by p-wave emission. The $J^{\pi} = 8^{+}$ state is much less likely to be populated with comparable intensity, since this would require f-wave emission for which the penetrability is lower by approximately two to three orders of magnitude over the energy range of these experiments.

Very recent work on the $^{181}Ta(d,t)^{180}Ta$ reaction has resulted in the population of higher energy excited states in ^{180}Ta (De 82). The results of this study are compared to our energy levels in Table (5.12).

A majority of the levels from the (γ,n) reaction are seen to coincide to within 5 Kev to those populated in the (d,t) reaction. Seven levels populated in the (γ,n) reaction were not seen in the (d,t) work. Of the four levels not populated in the (γ,n) reaction, two may be explained by the non-favourable spin configuration for the 592 Kev

TABLE 5.12

COMPARISON OF HIGHER ENERGY LEVELS POPULATED IN THE $^{181}Ta(\gamma,n)^{180}Ta$ REACTION WITH THOSE FROM THE $^{181}Ta(d,t)^{180}Ta$ REACTION

LEVEL ENERGY (Kev)		J^{π} (From (De 82))
(γ,n)	(d,t)	
0	0	1^+
39(2)	45	2^+
*73		9^-
109(2)	114	3^+
	172	8^+
179(2)	187	4^+
231(2)		
259(2)		
309(2)	312	5^+
365(3)	376	9^+
412(2)	420	1^-
442(2)		
466(3)	462	7^-
	476	2^-
515(3)		
542(2)	545	3^-
571(2)	571	6^-
	592	10^+
624(2)		
643(2)	652	4^-
666(3)	671	8^-
720(2)	712	4^-
	753	7^-
	775	3^-
793(2)		
820(2)	822	5^-
857(2)		
	875	4^-
897(2)	893	
	930	
959(3)	948	6^-

* Inferred from the (n,γ) reaction.

and 753 Kev levels. The listed spins of 3^- and 4^- for the 775 Kev and 875 Kev levels respectively suggest s-wave neutron emission should be allowed, and thus transitions may be expected to be observed. The strongest line in nickel (8.999 Mev) produced possible excited state energies in the range of these two, but the strongest chromium line (8.884 Mev) did not. For this reason these two levels were not listed in the proposed ^{180}Ta energy level scheme presented here.

5.4 The Angular Distributions

The spectra which produced intense enough photoneutron groups to permit angular distribution measurements were:

(i) Aluminum (E_γ = 7724 Kev) on Thallium (^{205}Tl)
E_x = 0 and E_x = 141 Kev.

(ii) Iron (E_γ = 7646 Kev) on Thallium (^{205}Tl)
E_x = 0.

(iii) Iron (E_γ = 7632 Kev) on Lead (^{207}Pb)
E_x = 803 Kev.

The first spectrum above has already been shown in Fig. (5.1). The latter two spectra are shown in Figs. (5.9) and (5.10) respectively. Tables (5.13), (5.14) and (5.15) contain the results of these experiments. The areas listed for each angle are simply the observed peak areas corrected for incident photon beam intensity by the use of the beam monitor readings. This procedure resulted in decreased error assignments since the errors associated with incident photon flux

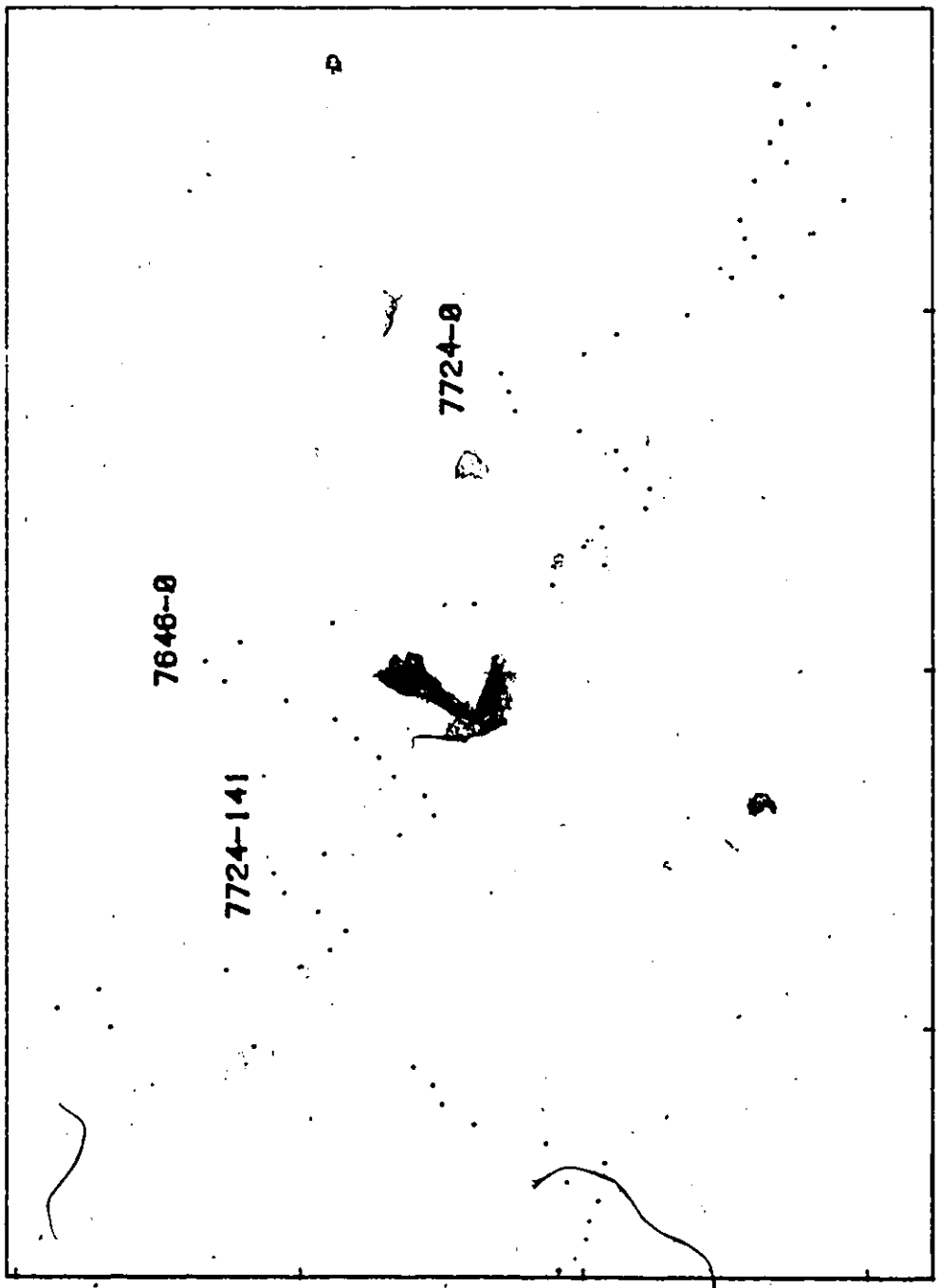

Figure 5.9 Photoneutron Spectr[illegible] Iron Source on Thallium

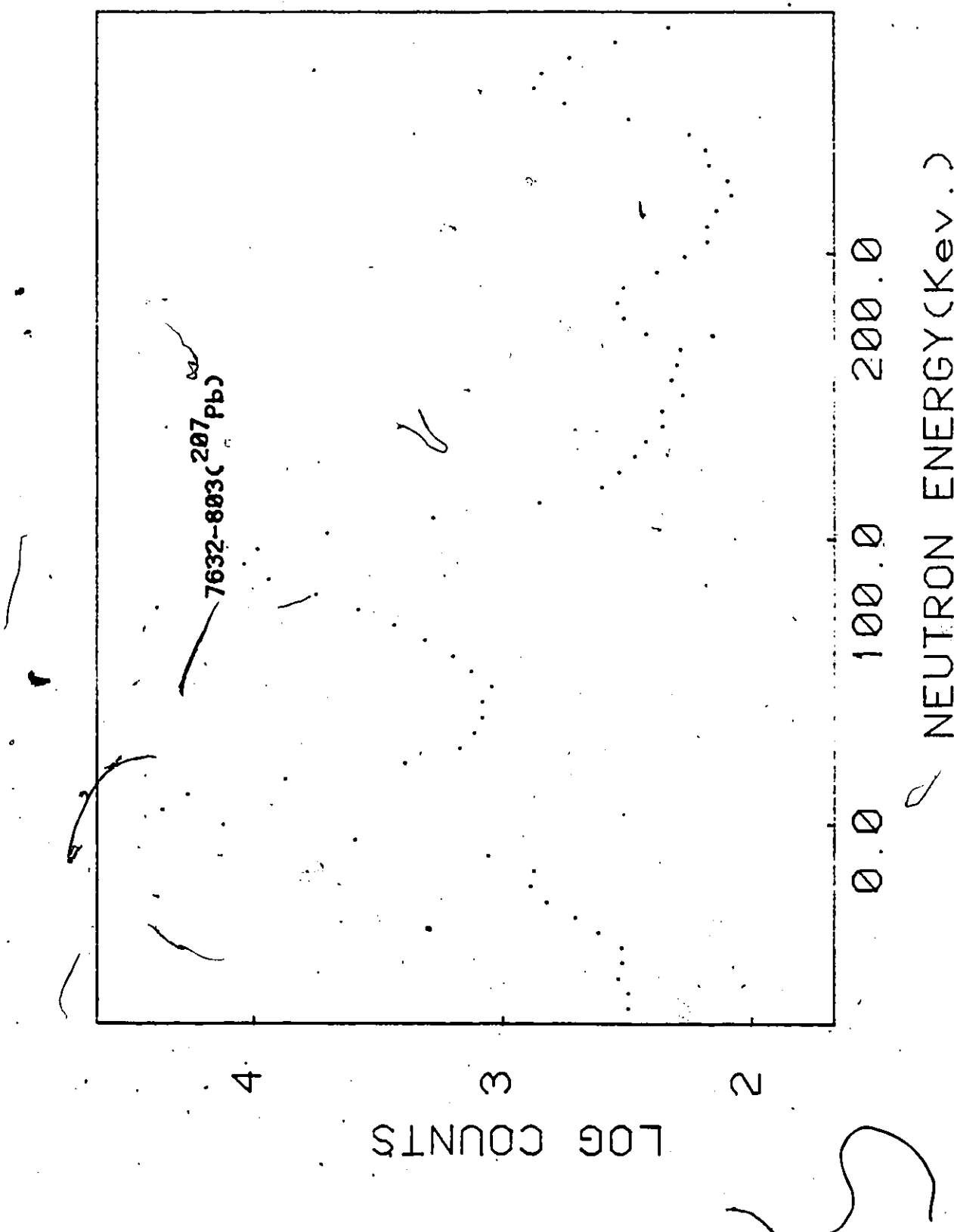

Figure 5.10 Photoneutron Spectrum from Iron Source on Natural Lead Target

TABLE 5.13

ANGULAR DISTRIBUTION OF EMITTED PHOTONEUTRONS FROM THALLIUM TARGET INITIATED BY ALUMINUM (E_γ = 7724 Kev) SOURCE

ANGLE	AREA (ARBITRARY UNITS)	
	E_x = 0	E_x = 141 Kev
30°	79.4 ± 4	350 ± 16
45°	77.8 ± 4	332 ± 16
60°	83.5 ± 3	366 ± 14
75°	84 ± 3	357 ± 14
90°	83.7 ± 3	370 ± 14
105°	84.1 ± 3	376 ± 14
120°	83.1 ± 3	364 ± 14
135°	81.5 ± 3	367 ± 14
150°	85 ± 3	347 ± 14

FITTED PARAMETERS

E_x = 0 Reduced Chi Squared = .33

$$\omega(\theta) = 1 + (-3.14 \times 10^{-2} \pm 1.31 \times 10^{-2})P_1(\cos\theta) + (-3.14 \times 10^{-2} \pm 1.7 \times 10^{-2})P_2(\cos\theta) + (-2.88 \times 10^{-2} \pm 2.25 \times 10^{-2})P_3(\cos\theta)$$

E_x = 141 Kev Reduced Chi Squared = .544

$$\omega(\theta) = 1 + (-1.99 \times 10^{-2} \pm 1.80 \times 10^{-2})P_1(\cos\theta) + (-5.77 \times 10^{-2} \pm 2.35 \times 10^{-2})P_2(\cos\theta) + (3.32 \times 10^{-2} \pm 3.09 \times 10^{-2})P_3(\cos\theta)$$

TABLE 5.14

ANGULAR DISTRIBUTION OF EMITTED PHOTONEUTRONS FROM THALLIUM TARGET INITIATED BY IRON (E_γ = 7646 Kev) SOURCE

ANGLE	AREA (ARBITRARY UNITS)
30°	269 ± 14
45°	274 ± 14
60°	293 ± 12
75°	273 ± 11
90°	283 ± 11
105°	283 ± 11
120°	278 ± 11
135°	289 ± 12
150°	268 ± 16

FITTED PARAMETERS

Reduced Chi Squared = .626

$$\omega(\theta) = 1 + (-1.15 \times 10^{-2} \pm 2.29 \times 10^{-2})P_1(\cos\theta) + (-2.07 \times 10^{-2} \pm 2.83 \times 10^{-2})P_2(\cos\theta) + (-8.71 \times 10^{-2} \pm 3.69 \times 10^{-2})P_3(\cos\theta)$$

TABLE 5.15

ANGULAR DISTRIBUTION OF EMITTED PHOTONEUTRONS FROM LEAD TARGET INITIATED BY IRON (E_γ = 7632 Kev) SOURCE

ANGLE	AREA (ARBITRARY UNITS)
30°	2684 ± 90
45°	2654 ± 90
60°	2732 ± 70
75°	2680 ± 70
90°	2628 ± 70
105°	2655 ± 70
120°	2828 ± 70
135°	2731 ± 70
150°	2713 ± 70

FITTED PARAMETERS

Reduced Chi Squared = .893

$$\omega(\theta) = 1 + (-1.43 \times 10^{-2} \pm 1.75 \times 10^{-2})P_1(\cos\theta) + (1.07 \times 10^{-2} \pm 2.17 \times 10^{-2})P_2(\cos\theta) + (1.19 \times 10^{-2} \pm 2.78 \times 10^{-2})P_3(\cos\theta)$$

measurement and detector efficiency did not have to be included. Total counting time for each angle in each spectrum was 70,000 sec. The fitted parameters in the tables have all been normalized to $a_0 = 1$.

The high photoneutron yield associated with these transitions is indicative of the excitation of an individual unbound resonance energy level. This type of behaviour would be expected based on the level density in ^{205}Tl as discussed in Chapter 2. The total cross sections for these levels (sec. 5.6) corroborate this assumption.

The angular distributions of the emitted photoneutron from the lead target may be compared to the work of Birenbaum et al (Bi 79) where the angular distribution coefficients are given as $\omega(\theta) = 1 + (0.01 \pm 0.01)P_2(\cos\theta)$. This isotropic distribution is in agreement with our results. By neglecting the P_1 and P_3 contributions Birenbaum presupposes the excitation of one single level only, and thus allows no odd-even ℓ neutron mixing. This assumption was not made here for the sake of generality, but clearly the results would not be affected.

Considering the target spin and parity of the ground state in ^{207}Pb are $J_A^{\pi A} = \frac{1}{2}^-$, and those of the 803 Kev level in ^{206}Pb are $J_A^{\pi A} = 2^+$, then the s-wave emission clearly establishes this strong resonance to have spin and parity $J^\pi = \frac{3}{2}^+$.

An examination of the aluminum spectra angular distributions also reveals dominance of s-wave neutrons for transitions to both the

ground state and first excited state in ^{204}Tl. The ground state spin and parity in ^{205}Tl are $\frac{1}{2}^+$. Lederer (Le 78) assigns the possible spins and parities of the ground state and first excited state in ^{204}Tl as follows: ground state, $J^\pi = 2^-$ or 3, 1st excited state J = 1.

The only possible combination of the above parameters which would produce the isotropic neutron distribution is for the dominant resonance to be $\frac{3}{2}^-$ and assign spins and parities in ^{204}Tl as:

ground state $J^\pi = 2^-$

1st excited state $J^\pi = 1^-$

Again, incident E1 photoexcitation is assumed here. The small values of a_1, a_2 and a_3 coefficients may indicate contributions from another resonance. A nearby resonance with spin $\frac{1}{2}$ could explain the higher relative population of the first excited state.

The angular distributions from the 7646 Kev iron gamma ray on thallium photoneutron spectra also reveal s-wave dominance. This would then establish the resonant spin as $\frac{3}{2}^-$ or $\frac{5}{2}^-$ in order to reach the 2^- ground state. This assignment is at odds with the work of Moreh et al (Mo 70) who assign $J_\pi^r = \frac{1}{2}^-$ on the basis of γ ray scattering experiments. This assignment clearly requires either p-wave neutron emission or the reassignment of the ground state spin. It is not clear at this point exactly how to reconcile this difference.

5.5 Determination of Photon Fluxes

5.5.1 The Pair Spectrometer Efficiency

The measurement of the pair spectrometer efficiency as a function of incident gamma ray energy yielded functional forms in the region of 3-11 Mev from the nitrogen capture γ ray spectrum and in the region of 1.7 - 3.6 Mev from the ^{56}Co decay spectrum. Normalization of the two curves to each other produced the curve drawn in Fig. (5.11). Also shown are the results from the beryllium and iron neutron capture gamma ray spectra, where the areas of the most intense peaks in each case have been normalized to the efficiency curve at their respective energies.

Also shown is the renormalized NaI pair cross section, taken from the work of Storm and Israel (St 70). It is noted that the two curves coincide up until $E_\gamma \approx 6$ Mev, when the efficiency curve turns over due to Bremsstrahlung and range effect losses.

An examination of the spectra in Figs. (4.7) (4.8) and (4.9) reveals good agreement with the form predicted in the appendix. In particular, the "dip" in the spectrum below the pair peak due to Bremsstrahlung reabsorption is evident, especially on the 10.83 Mev peak in the nitrogen spectrum. The long low energy tail below the higher energy peaks may be viewed as the sum of the exponential Bremsstrahlung component and the flat range effect component. It should be noted that very little tail effects are noted for $E_\gamma < 5$ Mev,

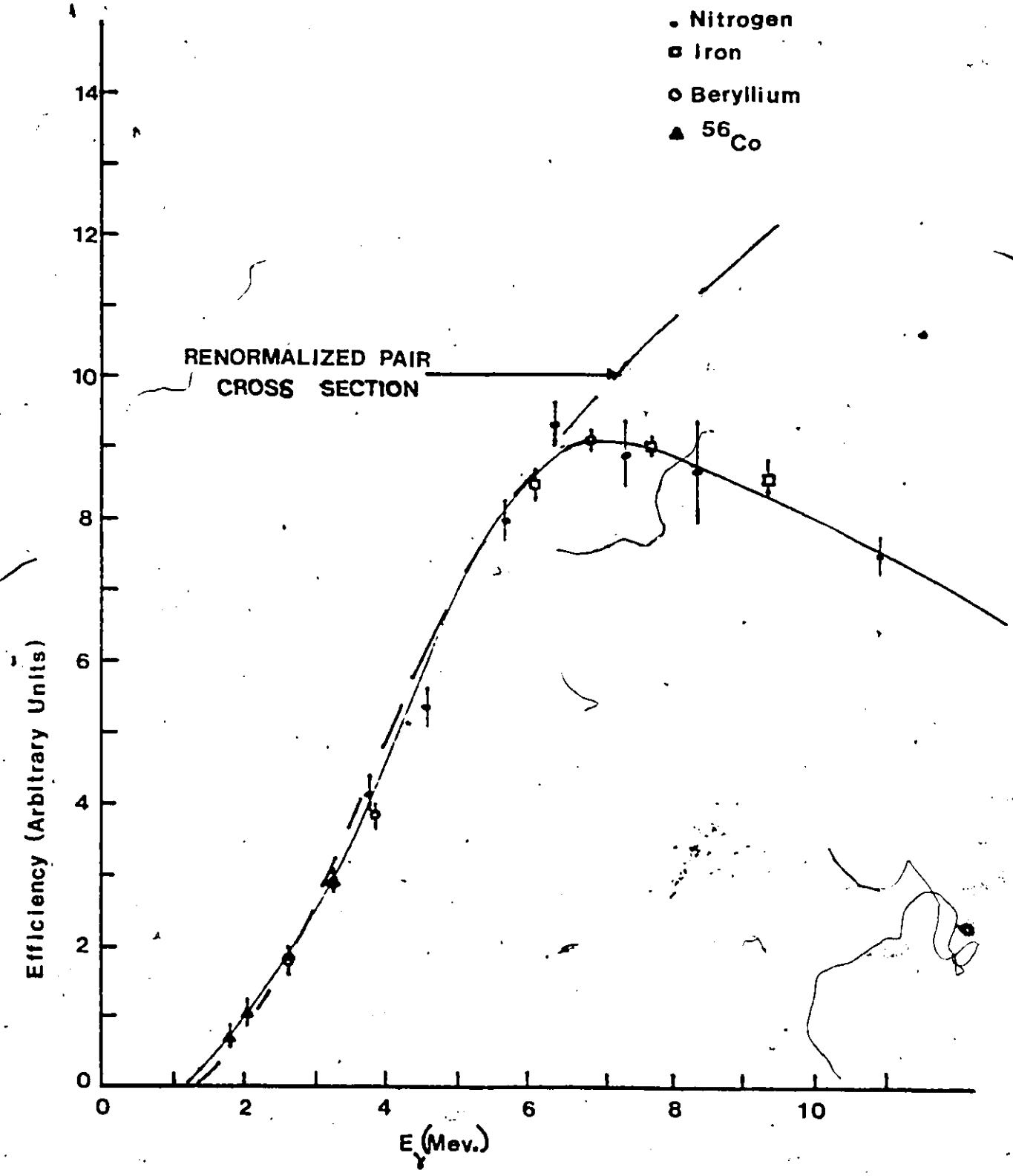

Figure 5.11 Relative Efficiency of Pair Spectrometer. The Renormalized NaI pair cross section is also shown.

which is consistent with the efficiency curve parallelling the pair cross section up until this energy.

As a further test of the model developed in the appendix, a quadratic least squares fit was made to the ratio of the relative efficiency divided by the pair cross section. The normalized result was

$$\frac{\varepsilon(E_\gamma - 1)}{\sigma_{pair}} = 1 - (.03 \pm .003)(E_\gamma - 1) - (2.44 \times 10^{-3} \pm 1.89 \times 10^{-4})(E_\gamma - 1)^2 \qquad (5.5.1)$$

which may be compared with the form derived in the appendix

$$\frac{\varepsilon(E_\gamma - 1)}{\sigma_{pair}} = 1 - 2.4 \times 10^{-2}(E_\gamma - 1) - 3.48 \times 10^{-3}(E_\gamma - 1)^2 \qquad (5.5.2)$$

The linear contribution is seen to be in good agreement with the predicted theory, indicating the range contribution to energy escape crises predominantly from electrons exitting via the back face of the crystal.

The measured quadratic term is somewhat lower than that predicted from the work of Dance. This may be explained by the fact that the crystal dimensions here are greater than the electron range, and consequently the reabsorption of Bremsstrahlung photons is more pronounced, resulting in a lower photon yield.

5.5.2 The Photon Beam Spectral Components

The determination of peak areas, and thus the incident gamma ray intensities was straightforward using the techniques in Chapter 4. The only cases where a straightforward area determination was not possible was for the case of the copper 7915 Kev line, and the iron 7632-7646 Kev doublet. Both were not resolved from the aluminum 7724 Kev line present in all spectra.

The method chosen to obtain these peak areas made use of the strong photoneutron transitions arising from the 7724 Kev line on ^{205}Tl. These transitions were clearly observed in the $^{205}Tl(\gamma,n)^{204}Tl$ spectra from the copper and iron sources.

Thus a measurement of the relative contribution of the 7724 Kev γ ray from either the Cu or Fe source compared to the Aℓ source was easily made. The spectrum from the Aℓ source was multiplied by this constant, and subtracted point by point from the Fe and Cu source spectra, leaving only the contribution from the strong intensity lines to be analyzed. No attempt was made to deconvolve the iron doublet, rather the total area was divided into the appropriate ratios given in Chapter 1.

The use of equation (4.7.9) allowed direct determination of the incident γ-ray intensity (sec^{-1}) at any one energy. The results appear in Table (5.16).

TABLE 5.16

INCIDENT GAMMA RAY INTENSITIES OF MAJOR PHOTON BEAM SPECTRAL COMPONENTS

SOURCE	E_γ(Kev)	INTENSITY (sec^{-1})
Aluminum	7724	$(2.32 \pm .15) \times 10^5$
Copper	7915	$(3.48 \pm .31) \times 10^5$
Nickel	8533	$(1.32 \pm .10) \times 10^5$
	8999	$(2.94 \pm .19) \times 10^5$
Chromium	8884	$(2.55 \pm .19) \times 10^5$
	9720	$(1.04 \pm .07) \times 10^5$
Iron	7632	$(2.32 \pm .20) \times 10^5$
	7646	$(1.89 \pm .15) \times 10^5$

5.6 Cross Sections of Individual Excited State Levels

5.6.1 Cross Sections of Strongly Populated Levels

The cross sections for the transitions which provided strong enough neutron groups to allow angular distribution measurements are presented in Table (5.17). By direct comparison these cross sections are seen to be orders of magnitude larger than the cross sections associated with "non-resonant" transistions listed in Tables (5.5) and (5.6). Thus this provides justification for their assignment as excitation of single unbound resonance levels in the target nuclei.

The value listed here for the cross section for the 7632 Kev initiated transition to the 803 Kev excited state in ^{207}Pb is 397 ± 34 mb. This is in excellent agreement with Buenbaum's quoted value of 370 ± 50 mb (Bi 79).

5.6.2 Cross Sections Populating Off-Resonance Regions

The partial cross sections for transitions into all observed excited states in ^{204}Tl and ^{180}Ta are given in Tables (5.17) and (5.18). Each element will be discussed individually.

(a) Thallium

The $^{205}Tl(\gamma,n)^{204}Tl$ cross section are lower at 7915 Kev than at 7724 Kev and 7646 Kev, indicative of off resonance behaviour. The

TABLE 5.17

CROSS SECTIONS OF STRONGLY POPULATED LEVELS

SOURCE	E_γ(Kev)	TARGET ISOTOPE	ENERGY OF EXCITED STATE POPULATED (Kev)	CROSS SECTION (mb)
Aluminum	7724	^{205}Tl	0	33.4 ± 2.9
Aluminum	7724	^{205}Tl	141	55.2 ± 4.7
Iron	7646	^{205}Tl	0	99.3 ± 7.7
Iron	7632	^{207}Pb	803	397 ± 34

ground state transition is populated more intensely by the 7915 Kev γ ray (by a factor of 6) than the transition to the first excited state. An examination of spins suggests the nearest strong resonance may be $J^{\pi} = \frac{5}{2}^{-}$ in nature. The excited state at 319 Kev (spin 1) is not populated here, and this may be due to positive parity requiring p wave neutron emission. The 300 Kev level at $E_n = 166$ Kev is strongly populated - a fact which suggests a negative parity assignment allowing s-wave neutron emission.

Also apparent from the copper source spectrum is the lack of any evidence of population of the ground state transition in the $^{203}Tl(\gamma,n)^{202}Tl$ reaction. If McFee's (Mc 77) Q-value of 7737 ± 5 Kev is accepted, this transition (E_n = 177 Kev) would be obscured by the $^{205}Tl(\gamma,n)^{204}Tl$ ground state transition initiated by the aluminum (E_γ = 7724 Kev) γ ray giving a photoneutron group at E_n = 174 Kev. A comparison was made of the ratios of the areas of the ground state to first excited state transitions to ^{204}Tl initiated by the Al γ ray in both the copper and aluminum source spectra. No statistically significant difference was observed in the two ratios, indicative of a small $^{203}Tl(\gamma,n)^{202}Tl$ cross section.

As the gamma ray energy is increased, one notices differences in the ratio of the ground state to first excited state transition cross section ratios. Since, according to the assigned spins and parities, s-wave emission is possible after E1 photoexcitation, this

may be an indication of the nearest strong resonance in each case. The cross sections of all levels show large fluctuations with incident γ ray energy, again indicative of a wide energy level spacing compared to incident γ ray resolution.

Maximum values for the unobserved ground state transition in the $^{203}Tl(\gamma,n)^{202}Tl$ reactions were calculated to be 0.9 mb at 8999 Kev, and 1.4 mb at 9720 Kev. These correspond to roughly 16% and 30% of the $^{205}Tl(\gamma,n)^{204}Tl$ ground state transition cross sections at these energies. This may be viewed as consistent with a ^{202}Tl ground state spin assignment of 3, when one considers the relative penetrabilities. The two transitions tentatively assigned as arising from the $^{203}Tl(\gamma,n)^{202}Tl$ reaction give cross sections of the order of 1-3 mb, depending, of course, on the incident γ ray energy assignment.

(b) Tantalum

The $^{181}Ta(\gamma,n)^{180}Ta$ cross sections are in general seen to be smaller and less variant than the $^{205}Tl(\gamma,n)^{204}Tl$ cross sections, both facts which may be attributed to the increased level density in ^{181}Ta. Only a very few cross sections may positively be assigned as being greater than 6 mb - with the exception of those levels populated by the 8533 Kev γ ray. The anomolous nature of the cross sections associated with this γ ray will show up again when a discussion of total reaction cross sections and reduced widths is made. For the case of the individual level cross sections at 8533 Kev, the extreme variations here would suggest, contrary to theory, that one resonance level is

dominating. If one accepts the spin assignments of Warde, and assumes the neutron group at 915 ± 2 Kev is populated by the 8.999 Mev γ ray, then the dominant resonance in this region would require a spin of $\frac{9}{2}$ or greater.

The multiplicity of level assignment ambiguities does not allow for easy fitting of the observed cross sections to optical model transmission coefficients. An examination of the cross sections of the ground state and first two excited states as a function of incident γ ray energy is presented in Table (5.18). From the table it is readily apparent that the ratios of these cross sections vary greatly. If one again assumes the spin assignments given by Warde (Wa 79) to be correct, all three states may be populated by p-wave neutron emission following E1 photoabsorption, and one would expect all three states to populated with comparable intensity. One possible explanation here is that the density of levels as proposed in Chapter 2 is too high. Table (2.4) lists the level densities of all spins and parities. The densities of states of spins and parities $\frac{5}{2}^-$, $\frac{7}{2}^-$ and $\frac{9}{2}^-$ (those capable of being reached by E1 photoexcitation) are roughly 10% of these quoted densities. At the lower γ ray energies this would correspond to an average spacing of 0.6 ev, and at 9 Mev a spacing of 0.1 ev. A possible interpretation is that whereas the total density of states allows smooth variation of the total cross section, the density of individual states is low enough for variations in partial cross sections to be observed.

TABLE 5.18

COMPARISON OF THE CROSS SECTIONS OF THE GROUND STATE TO FIRST EXCITED STATE ENERGIES IN $^{181}Ta(\gamma,n)^{180}Ta$ REACTION

E_γ(Kev)	$\frac{\sigma(39\ Kev)}{\sigma(ground\ state)}$	$\frac{\sigma(108\ Kev)}{\sigma(ground\ state)}$
7724	10.6	10.7
7915	6.4	15.2
8884	2.0	3.3
9720	1.3	3.6

5.7 Total Cross Sections and Gamma Ray Strength Functions

In order to evaluate the total photoneutron cross section at any one particular γ ray energy the procedure undertaken was to sum over all observed level cross sections and to make provision for the unobserved level transitions. The two photoneutron targets are discussed separately below.

(a) Thallium

The results for the $^{205}Tl(\gamma,n)^{204}Tl$ reaction are presented in Table (5.19).

The column headed observed minimum cross section represents the sum over all levels which could unambiguously be assigned as being populated by the particular γ ray in question. The next column (observed maximum) represents the sum over all levels which could possibly be assigned as being populated by the γ ray, i.e. this sum takes into account those numbered cross sections in Table (5.5). The third column represents the maximum cross section when all unobserved levels were assigned a maximum possible cross section. The strength function limits were calculated with the use of equation (2.6.12). The final column represents the expected strength function based on a fit to the tail of the Giant Dipole Resonance in Tl (a Lorentzian fit was used to known parameters) from the work of Bartholomew et al (Ba 73). An arbitrary error of $\pm .05 \times 10^{-7}$ has been assigned here.

TABLE (5.19)

TOTAL CROSS SECTIONS AND GAMMA RAY STRENGTH FUNCTIONS FOR $^{205}Tl(\gamma,n)^{204}Tl$ REACTION

E_γ(Kev)	OBSERVED CROSS SECTIONS		TOTAL MAXIMUM (including unobserved) (mb)	STRENGTH FUNCTION LIMITS ($\times 10^{-7}$)	STRENGTH FUNCTION FROM BARTHOLOMEW ($\times 10^{-7}$) ($\pm.05$)
	MIN(mb)	MAX(mb)			
7724	88.6±5.5		88.6±5.5	9.95±.61	4.8
7632	99.3±7.7		99.3±7.7	10.2±.79	4.6
7915	29.7±2.4		29.7±2.4	3.26±.26	5.1
7819	3.18±.39	11.12±1.07	11.12±1.11	1.22±.11	4.9
7939	4.66±.9	4.66±.9	8.66±1.3	0.40-1.06	5.1
8121	50.06±4.1	83.4±5.3	109.1±8.1	5.32-11.57	5.1
8485	-	-	8.2±1.4	0-1.85	6.2
8512	32.76±3.5	42.2±4.2	64.6±4.8	11-22	6.2
8533	32.7±3.5	62.3±4.1	66.7±4.3	3.31-6.75	6.2
8884	78.8±8.2	90.9±8.3	94.11±8.6	7.69-9.19	6.9
8999	60.0±1.9	70.2±2.1	72.8±2.1	5.77-7.1	7.1
9720	58.1±3.6	88.8±3.8	116.2±4.7	5.18-10.4	10.0

Several facts are immediately obvious from the table. Firstly the weak intensity gamma rays produce strength function estimates which have particularly large error limits. However, even in the case of the strong intensity gamma rays, the calculated strength functions exhibit large fluctuations with respect to the fit of Bartholomew. This last fact is particularly true of lower gamma ray energies, and this would be expected due to the lower density of energy levels in this region. From the strength functions it would appear that there is on or near resonance behaviour at 7724, 7632 and perhaps 8121 and 8512 Kev. The γ ray energies at which the strength function (or cross section) is considerably lower than the Lorentzian fit are 7646, 7819, 7915, 7937 and 8485 Kev.

It should be pointed out here that in his work Bartholomew shows the results of two separate experiments to determine strength functions. The first (Ea 73) measured the strength function from photoelastic scattering measurements on ^{205}Tl, while the second (Ga 57) consist of photoneutron cross section work on natural Tl. The fact that the error limits of the two experiments overlap may lend credence to the small $^{203}Tl(\gamma,n)^{202}Tl$ cross sections reported here.

(b) Tantalum

Table (5.20) gives the results of the cross section analysis applied to the $^{181}Ta(\gamma,n)^{180}Ta$ reaction. The table follows along the lines of the thallium cross section table. Again the preponderance of ambiguous energy level assignments due to the high density of states in

TABLE (5.20)

TOTAL CROSS SECTIONS FOR $^{181}Ta(\gamma,n)^{180}Ta$ REACTION

E_γ (Kev)	OBSERVED CROSS SECTIONS		LIMITS ON CROSS SECTION (including unobserved) (mb)	CROSS SECTION FROM (Hu 67) (mb)	CROSS SECTION FROM (Fu 58) (mb) (±2)
	MIN(mb)	MAX(mb)			
7724	4.68±.32	4.68±.32	4.68±.32	4.14±.36	5
7915	12.86±.64		12.86±.64		12
7937	.51±.08	3.77±.92	0.51-12.2		12
8121	0	79.9±8.6	0-89.5		18
8485	8.94±1	37.0±3.6	7.94-44.3		32
8512	7.99±1.5	38.1±3.1	7.49-45.2		32
8533	46.4±2.1	88.0±5.2	44.3-91.0		32
8884	27.6±1.8	33.1±2.2	25.4-36.2		35
8999	37.2±1.0	43.9±1.1	36.2-45.2	45.4±3.7	40
9720	29.6±1.5	35.0±1.7	28.1-50.2	65.0±5.5	58

^{180}Ta and the large number of gamma rays able to initiate low neutron energy tansititions results in large limits on the cross sections, especially for the weaker γ rays.

The references presented for comparison are taken from the works of Hurst and Donahue (Hu 67) and Fuller and Weiss (Fu 58). The former paper used monochromatic photon sources of aluminum, nickel and chromium sources, and the emitted photoneutrons were first thermalized and then counted with four $B^{10}F_3$ detectors. A smoothly varying cross section corresponding to the tail of a Lorentzian fit to the GDR was assumed here, and the weighted incident γ ray flux at each energy was used to derive the photoneutron cross sections. The second paper used a Bremsstrahlung incident photon beam (with subsequent poorer energy resolution) and again a BF_3 detector system. The values quoted are from the authors' smoothly drawn fit to the data, and an error of ±2 mb has been assigned.

In general the total photoneutron cross-sections are in excellent agreement with the two results. Since the Bremsstrahlung experiments clearly involve averaging over many resonances, it can safely be assumed that the capture gamma ray beams also average over a number of resonances - a fact predicted by the high level densities. The cross section is seen to be smoothly varying within error limits with two exceptions - those being the cross sections due to the 8533 Kev (Ni) γ ray and the 9720 Kev (Cr) γ ray.

The lower cross section exhibited by the chromium γ ray initiation may be explained easily by two facts. Firstly, the 11 lowest energy excited states in ^{180}Ta were not populated by this γ ray due to low γ ray flux and rapidly falling detector efficiency. Inclusion of the unobserved cross sections for these levels brings the total cross section close to 50 mb. Secondly, as previously mentioned, the low density in states above 1 Mev as populated by the 9720 Kev γ ray indicate many overlaps with other γ ray initiated transitions occur. Since these transitions were too high in energy to be verified by population with other γ ray sources, they were not considered as 9720 Kev initiated transitions. It would not seem unreasonable to raise the total cross section by up to 10 mb, and bring it in line with the references. This procedure would also result in the lowering of the upper limits on the 8485 Kev and 8512 Kev γ ray cross sections - a fact which would still leave them in accord with the reference.

The case of the total cross section for transitions initiated by the 8533 Kev γ ray is quite different. The total cross section here is, even at its minimum value some 1.4 times greater than the expected value. One possible explanation for this phenomenon is contribution from a giant resonance. The nearest such resonance is M1 (isovector) in nature and is predicted by theory to lie very roughly at $45/A^{1/3}$ Mev, which corresponds to 7.96 Mev for tantalum. However, the deformed nature of the nucleus, coupled with the lack of data on the precise location of such resonances may not rule out this as a candidate for explanation. In any event as seen earlier the dominant "resonance" at

8.533 Kev would be required to have spin $\frac{9}{2}$ or more, and averaging over resonances is not seen to occur at this energy.

The higher cross section at 8.533 Mev may have implications for the work of Hurst. Clearly Hurst's assigned value of $\sigma_{\gamma n}$ = 45.4±3.7 mb would be high if the 8.533 Mev anomoly is taken into consideration. Fuller's quoted value of 40 ± 2 mb would seem more reasonable, and is close to the average value presented here.

5.8 The Distribution of Reduced Widths

Table (5.21) gives the number of degrees of freedom for each of the two reactions based on the method proposed in Chapter 2. For the $^{181}Ta(\gamma,n)^{180}Ta$ reaction, the column labelled (a) represents the division of each cross section by $\sqrt{E_n}$, while the column (b) has used the spin assignments of Warde to allow for p-wave neutron emission for the low-lying states in Table (5.11). Thus the reduced widths for these cases was multiplied by the ratio of s-wave to p-wave transmission coefficients at that neutron energy. In the tables, only the unambiguously assigned level cross sections were used, and provision was made to include maximum unobserved cross section estimates.

The degrees of freedom for thallium are in general less than the estimates for tantalum, although not by as much as expected. This may be due to the fact that division by $\sqrt{E_n}$ does not yield accurate

TABLE 5.21

DEGREES OF FREEDOM FOR $^{205}Tl(\gamma,n)^{204}Tl$ and $^{181}Ta(\gamma,n)^{180}Ta$ REACTIONS

E_γ (Mev)	$^{205}Tl(\gamma,n)^{204}Tl$ ν	$^{181}Ta(\gamma,n)^{180}Ta$ ν	
		(a)	(b)
7.915		3.9 ± 1.04	3.15 ± 1.01
8.533	3.12 ± .91	1.66 ± 1.18	1.32 ± 0.81
8.884	3.05 ± .85	2.71 ± .91	3.42 ± .83
8.999	2.25 ± 1.01	4.88 ± .69	6.54 ± .64
9.720	3.01 ± .87	4.29 ± .72	4.29 ± .72

reduced width estimates for all levels, and also may be due to the lower density of individual spin states in Ta previously discussed.

Again, the most glaring discrepency is that of the 8533 Kev γ ray incident upon ^{181}Ta. The low (~ 1) degrees of freedom is indicative of some sort of resonance behaviour here.

The number of degrees of freedom is seen to generally increase with increasing γ ray energy, as expected. The lower value at 9.720 Mev for Ta, may be explained by the fact that there are a number of unobserved excited state transitions for $E_x > 1$ Mev.

5.9 Critique and Statement of Future Goals

The method of monochromatic photoneutron spectroscopy with energy variant incident γ ray sources has proven successful in two major areas - those being the precise determination of photoneutron Q-values and nuclear energy level schemes. In the work presented here the method has resulted in increased precision in the measurement of the $^{205}Tl(\gamma,n)^{204}Tl$ and $^{181}Ta(\gamma,n)^{180}Ta$ Q-values as well as the development of the energy level scheme in ^{180}Ta for excitation energies up to approximately 1 Mev which was previously unobserved.

The use of the pair spectrometer to accurately determine the incident gamma ray fluxes allowed for accurate determination of reaction cross sections. A measurement of these cross sections can be used to assign resonance parameters to the photoneutron reaction at

some gamma ray energies. Resonances were discovered at several incident gamma ray energies in thallium - a fact one may have predicted from the energy level density in ^{205}Tl. The total (γ,n) cross section for ^{181}Ta was shown to be a smoothly varying function of γ ray energy corresponding to the tail of the G.D.R. except for the interesting anomoly at 8.533 Mev. Thus, for the most part the incident γ ray may be viewed as averaging over many resonances in ^{181}Ta. The individual ^{181}Ta$(\gamma,n)^{180}$Ta excited state cross sections showed enough variation to suggest that complete averaging over all individual excited energy levels did not occur.

One interesting facet of this thesis was the inability to accurately determine the ^{203}Tl$(\gamma,n)^{202}$Tl reaction Q value. The ground state transition was never observed for this reaction. In order to populate this transition with measurable intensity, it would seem that a separated target of ^{203}Tl should be acquired. The incident γ ray flux upon the target could also be increased with the removal of some neutron moderating material from the beam port, although this would clearly increase the neutron background.

An examination of the literature reveals several nuclei which could provide interesting targets for the experimental techniques presented here. These include ^{127}I and ^{133}Cs which have listed Q values of 9153 ± 8 Kev and 8979 ± 24 Kev respectively (Wa 77). In addition, no levels in either ^{126}I or ^{132}Cs have been reported (Le 78). Since both targets represent 100% isotopic abundance, procurement is no problem. However the low densities of the elements and the expected

low photoneutron cross sections would suggest that higher photon fluxes are imperative. Two higher Z target nuclei which may be examined are ^{151}Eu and ^{191}Ir. The photoneutron Q values here are 7982 ± 6 Kev and 8120 ± 150 Kev respectively (Wa 77) with little knowledge of the excited levels in the residual nucleus (Le 78). The isotopic abundance here of 48% and 37% respectively suggest that separated isotopes would be necessary.

Another prospect for nonochromatic photoneutron spectroscopy would involve a systematic search for resonance excitation. The energy level density for A ~ 200 nuclei is low enough to allow for chance individual excitation of unbound resonances, while evidence of M1 isovector giant resonance structure may occur in the 7.7 to 9 Mev range for nuclei with A in the range of 125 to 200.

APPENDIX

ILLUSTRATIONS

TABLES

APPENDIX

BREMSSTRAHLUNG AND RANGE EFFECTS

Following pair creation in the sodium iodide crystal, the subsequent positron annihilation will result in a full energy peak being recorded only if the total electron energy is contained in the detector. The two major processes by which energy may escape the crystal are Bremsstrahlung and range effects. In order to understand the nature of the detector response function it is necessary to explore the physical processes of pair production, Bremsstrahlung and electron range more fully.

PAIR PRODUCTION

In the process of pair production, the incident photon interacts with the field of the nucleus to produce an electron - positron pair. The photon energy clearly must be greater than $2\ m_0c^2$ where m_0 is the electron mass, and one may write an energy equation to describe this effect as

$$h\nu = (T_- + m_0c^2) + (T_+ + m_0c^2) \qquad (A.1)$$

where T_- and T_+ refer to the kinetic energies of the electron and position respectively, and $h\nu$ is the incident photon energy.

The energy distribution of each of the created particles has been shown (Be 34) to be symmetric about $\frac{h\nu - 2m_0c^2}{2}$ and roughly constant over the entire energy range from 0 to $h\nu - 2m_0c^2$. The angular distribution of the created particles is strongly peaked in the forward direction (Be 34). For example, considering the case of a 9 Mev photon, then the average angle between the created particles and the incident gamma ray direction is approximately 3°.

BREMSSTRAHLUNG

Bremsstrahlung, or braking radiation, is electromagnetic radiation which is created by accelerating charged particles. Thus following pair production, the creation of Bremsstrahlung photons takes place as a result of the negative acceleration necessary to bring the positron or electron to rest.

In order to the escape of Bremsstrahlung photons from thick targets, it is useful to consider the experiments of Dance et al (Da

68, Re 76). The authors here bombarded targets of Aℓ, Sn, Fe and Au with mono-energetic electron beams of energies ranging from 0.2 to 2.8 Mev. The targets had thicknesses corresponding to the mean electron range at the particular electron energy. The total external Bremsstrahlung radiation emitted from the targets was represented by the form

$$I_{BREM} = (0.36 \pm 0.04) \times 10^{-3} ZT^2 \qquad (A.2)$$

where Z is the atomic number of the target and T is the electron energy. The angular distribution of the emitted photons was found to be strongly peaked in the forward direction. The energy distribution of the emitted photons was found to fit an exponential of the form e^{-KE}.

For thicker targets (and higher electron energies) Berger and Seltzer (Be 68a) have shown that the photoelectric cross section of the target material results in re-absorption of low energy photons and a hardening of the Bremsstrahlung spectrum. Robertson et al (Ro 75) have observed this spectral form in an examination of the Bremsstrahlung photons produced following pair creation in a Ge(Li) detector.

The expected Bremsstrahlung contribution to the detector response function is shown in Fig. (A.1).

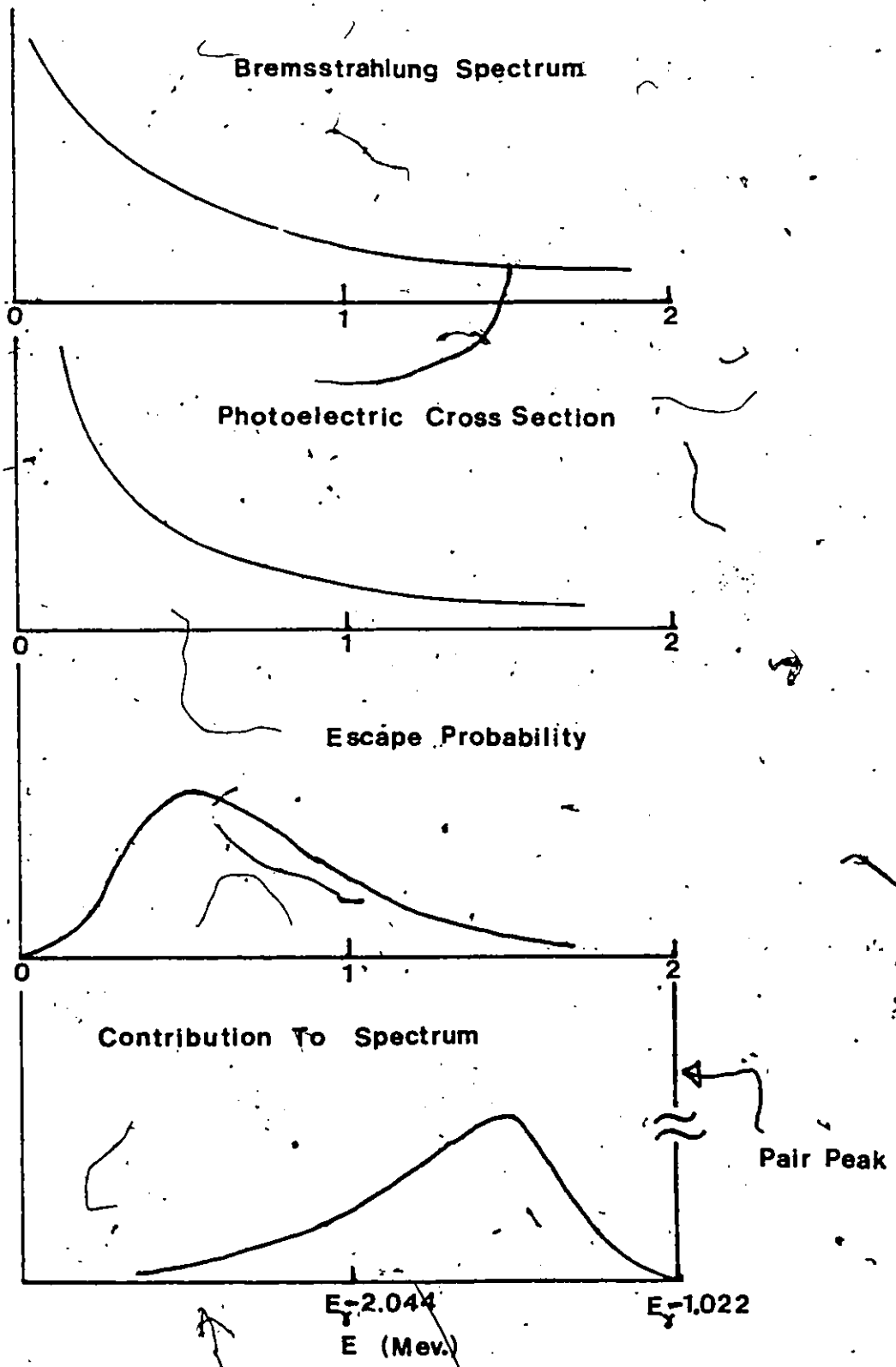

Figure A.1 Expected Bremsstrahlung Contributions to Pair Spectrometer Response

ELECTRON RANGE

Consider a beam of monoenergetic electrons incident upon a target. Then the number of transmitted electrons decreases with increasing target thickness in the manner shown in Fig. (A.2). The curve features a long tail due to electron straggling which is gradually masked by background statistics, and a flat linear portion just prior to the onset of the tail (eg Ar 66). The point at which the extrapolated linear portion meets the background is known as the electron range. For electron energies greater than 2.5 Mev Katz and Penfold (Ka 52) have derived an empirical relationship between the range $R(mg/cm^2)$ and electron energy E_0(Mev) as

$$R = 412\, E_0^{1.265 - 0.094 \ln E_0} \qquad \text{for } E_0 < 2.5 \text{ Mev}$$

$$R = 530\, E_0 - 106 \qquad \text{for } E_0 > 2.5 \text{ Mev} \qquad \text{(A.3)}$$

The work of Berger and Seltzer (Be 68b) gives the range of electrons in NaI, and these results are given in Table (A.1). For $E > 3$ Mev, we write

$$R(cm) = .76 + .15(E(Mev) - 4.0) \qquad \text{(A.4)}$$

The energy distribution of escaping electrons has been shown by Robertson (Ro 75) to be a flat continuum from 0 to (E_γ - 1.022 Mev).

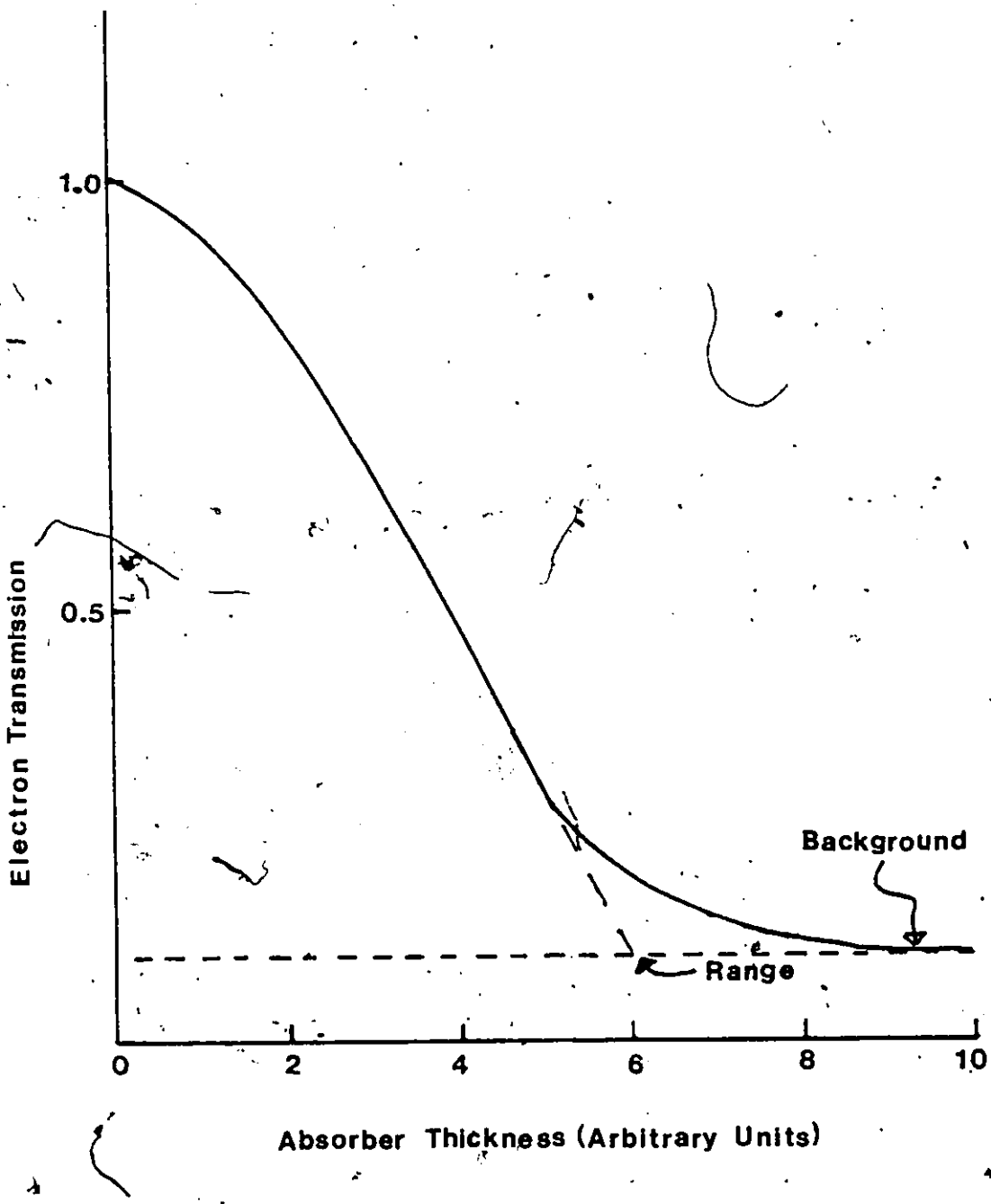

Figure A.2 Electron Transmission-Range Diagram

TABLE A.1

ELECTRON RANGES IN SODIUM IODIDE

ELECTRON ENERGY (Mev)	RANGE (cm)
2	0.39
4	0.76
6	1.08
8	1.36
10	1.64

MODELLING DETECTOR RESPONSE

The efficiency of the pair spectrometer may be expected to closely follow the NaI pair production cross section only when electron losses are not too severe. In order to model detector response, several simplifying assumptions must be made based upon the preceding sections. It is first assumed that electron propagation is confined to the forward (incident photon) direction, and secondly that the energy distribution of created electrons is flat from 0 to T_{max}, where $T_{max} = E_\gamma - 1.022$ Mev. Thus electrons may exit only through the back face of the crystal.

Using these assumptions losses due to Bremsstrahlung production may be written as (using equaiton A.2)

$$I_{BREM} = \left(\frac{1}{T_{max}}\right)(3.6 \times 10^{-4})Z \int_0^{T_{max}} T^2 dT$$

$$= (1.2 \times 10^{-4})Z\ T_{max}^2 \qquad (A.5)$$

Now taking as the average Z for NaI

$$Z = \frac{Z(Na) + Z(I)}{2} = 32 \qquad (A.6)$$

Then

$$I_{BREM} = (3.84 \times 10^{-3})T_{max}^2 \qquad (A.7)$$

The losses due to range effects may be modelled by considering the probability of an electron escape $P_e(T_{max})$ as

$$P_e(T_{max}) = P_c(T_{max})\ P_E \qquad (A.8)$$

where

$P_c(T_{max})$ = probability of an electron-positron pair being created within a distance R_{max} from the back face of the crystal, where R_{max} is the range corresponding to the maximum electron energy T_{max}.

and P_E = probability that an electron thus created will have enough energy to escape from the back face of the crystal.

The first term may be expressed as the ratio of the electron range at energy T_{max} to the crystal length (3.81 cm)

$$P_c(T_{max}) = .048\ T_{max}$$

To evaluate the second term, consider a uniform energy distribution of electrons located at a distance x from the back face of the crystal where $0 < x < R_{max}$. Here R_{max} is the range corresponding to the maximum electron energy T_{max}. An electron sampled from the distribution will escape if it has a range greater than the distance x.

Since the range varies linearly with electron energy, then the probability of escape from any distance x is

$$(1 - \frac{T(x)}{T_{max}}) = (1 - \frac{x}{R_{max}})$$

Thus the total escape probability is

$$P_E = \frac{1}{R_{max}} \int_0^{R_{max}} (1 - \frac{x}{R_{max}})dx$$

$$= \frac{1}{2}$$

So the range effect losses may be expected to vary as

$$P_e(T_{max}) = .024\ T_{max}$$

Thus the relative efficiency of the detector as a function of gamma ray energy may be thought of as the pair cross section with

appropriate Bremsstrahlung and range effect losses considered. We write

$$\varepsilon(E_\gamma) = \sigma_{pair}(E_\gamma)(1 - 2.4 \times 10^{-2} T_{max} - 3.84 \times 10^{-3} T_{max}^2)$$

or

$$\varepsilon(E_\gamma) = \sigma_{pair}(E_\gamma)(1 - 2.4 \times 10^{-2}(E_\gamma - 1) - 3.84 \times 10^{-3}(E_\gamma - 1)^2)$$

where $\varepsilon(E_\gamma)$ = pair spectrometer efficiency at E_γ,

and

$\sigma_{pair}(E_\gamma)$ = pair production cross section at E_γ.

This model is applied to experimental results in Chapter 5.

BIBLIOGRAPHY

Ah 73 J. Ahrens, H. Borchert, A. Ziegler and B. Ziegler, Nucl. Instr. and Meth. 108, 517 (1973).

Al 60 W.D. Allen, in Fast Neutron Physics, Part 1 Interscience Publishers Inc., N.Y., 361 (1960).

Ar 66 A.P. Arya, Fundamental of Nuclear Physics, Allyn and Bacon Inc., Boston, 240 (1966).

Ar 77 G. Ardisson, Radiochem. Radioanal Lett. 29(1), 7 (1977).

Av 62 E.H. Auerbach and F.G.J. Perey, Brookhaven National Laboratory Report No. BNL-765, 1962.

Au 71 R.L. Auble, Nucl. Data B5, 581 (1971).

Ba 60 R. Batchelor and G.C. Morrison in Fast Neutron Physics, Part 1 Interscience Publishers Inc., N.Y., 413 (1960).

Ba 73 G.A. Bartholomew, E.D. Earle, A.J. Ferguson, J.W. Knowles and M.A. Lone in Advances in Nuclear Physics, Plenum Press, London, 229 (1973).

Ba 79 J.N. Barkman, J.E. McFee, T.J. Kennett and W.V. Prestwich, Z. Phys. A289 (1979).

Ba 81 J.N. Barkman, Ph.D. Thesis, McMaster University (1981).

Be 34 H. Bethe and W. Heitler, Proc. Roy. Soc. A146, 83 (1934).

Be 68a M.J. Berger and S.M. Seltzer, NASA SP-169, 118 (1968).

Be 68b M.J. Berger and S.M. Seltzer, Nat. Bur. Std. Rep. 994, (1968).

Be 69a N. Bezic, A. Brinsek, G. Kernel and J. Snajder, Nucl. Instr. and Meth., 75, 190 (1969).

Be 69b R. Bergere, H. Beil, P. Carlos and A. Veyssiere, Nucl. Phys. A133, 417 (1969).

Be 76 R. Bergere, Lecture Notes in Physics, Photonuclear Reactions 1, Int. School on Electro- and Photonuclear Reactions, Springer-Verlag, Berlin, 1 (1976).

Bi 79 Y. Birenbaum, Z. Berant and R. Moreh in Neutron Capture Gamma Ray Spectroscpy, Plenum Press, N.Y., 564 (1979).

BNL325 Third Edition, Vol. 1, June 1973.

Br 51 H.N. Brown, W.L. Bendel, F.J. Shore and R.A. Becker, Phys. Rev. 84, 292 (1951).

Br 55 D.M. Brink, PL.D. Thesis, Univ. of Oxford (1955).

Br 57 D.M. Brink, Nucl. Phys. 4, 215 (1957).

Br 59 G.E. Brown and M. Bolsterli, Phys. Rev. Lett., 3 (10), 472 (1959).

Ca 71 R.W. Carr and J.E.E. Baglin, Nucl. Data A10, 143 (1971).

Ca 74 P. Carlos, H. Beil, R. Bergere, A. Lepretre, A. Deminiac and A. Veyssiere, Nucl. Phys., A225, 171 (1974).

Ch 34 J. Chadwick and M. Goldhaber, Nature 134, 237 (1934).

Cu 71 J.M. Cuttler, PL.D. Thesis, Technion (1971).

Cu 73 J.M. Cuttler, private communication to Bill (1973).

Da 68 W.E. Dance, D.H. Rester, B.J. Farmer and J.H. Jackson, J. Appl. Phys. 39, 2881 (1968).

Da 70 W.E. Dance, D.H. Rester, B.J. Farmer and J.H. Jackson, J. Appl. Phys. 41, 2682 (1970).

De 82 R. Dewberry, Princeton Univ., private communication (1982).

Do 66 B.S. Dolbilkin, V.A. Zapevalov, V.I. Korin, E. Lazereva, and F.A. Nikolaev, Bull. Acad. Sci. U.S.S.R. Phys. 30, 354 (1966).

Ea 73 E.D. Earle, J.W. Knowles, M.A. Lone and G.A. Bartholomew Contributions to the XXIII National Conference on Nuclear Spectroscopy and Structure of the Atomic Nucleus, Tbilisi, U.S.S.R., (1973).

Ev 55 J.E. Evans, E.G. Jokiand R.R. Smith, Phys. Rev. 97, 565 (1955).

Fi 70a F.W.K. Firk, Ann. Rev. Nucl. Sci. 20, 39 (1970).

Fi 70b F.W.K. Firk and E. Melkonian in Experimental Neutron Resonance Spectroscopy, Academic Press, N.Y. (1970).

Fr 73 H. Franz, private communication to J.M. Cuttler (1973).

Fr 77 H. Franz, W. Rudolph, H. Ohm, K-L. Kratz, G. Herrmann, F.M. Nul, D.R. Slaughter and S.G. Prussin, Nucl. Inst. and Meth. 144, 253 (1977).

Fu 58 E.G. Fuller and M.S. Weiss, Phys. Rev. 112, 560 (1958).

Fu 62 S.C. Fultz, R.L. Bramblett, J.T. Caldwell and N.A. Kerr, Phys. Rev. 127, 1273 (1962).

Fu 73 A. Furini, R. Alberini, D. Lattazari, Nvo. Cim. s11, 18A, 711 (1973).

Ga 57 B.L. Gavilrov and L.E. Lazareva, Sov. Phys. JETP 3, 871 (1957).

Ge 60 K.N. Geller, J. Halpern and E.G. Muirhead, Phys. Rev. 118, No. 5, 1302 (1960).

Gi 65 A. Gilbert and A.G.W. Cameron, Canadian Journal of Physics 43, 1446 (1965).

Go 48 M. Goldhaber and E. Teller, Phys. Rev. 74(9), 1046 (1948).

Gu 72 J. Guilles, R.E. Doebler and W.C. McHarris, Phys. Rev. CS, 2107 (1972).

Ha 57 S.S. Hanna and L. Meyer - Schützmeister, Phys. Rev. 108, 1644 (1957).

Ha 76a S.S. Hanna, Lecture Notes in Physics, Photonuclear Reactions 1, Int. School on Electro- and Photonuclear Reactions, Springer-Verlag, Berlin, 275 (1976).

Ha 76b E. Hayward, Lecture Notes in Physics, Photonuclear Reactions 1, Int. School on Electro- and Photonuclear Reactions, Springer-Verlag, Berlin, 340 (1976).

He 64 R.L. Heath, Scintillation Spectrometry, AEC (U.S.) Report TID-4500, Idaho (1964).

He 71 R.G. Helmer, R.C. Greenwood and C.W. Reich, Nucl. Phys. A168, 449 (1971).

Ho 79 R.J. Holt, H.E. Jackson, R.M. Laszewski and J.R. Specht, Phys. Rev. C20, 93 (1979).

Hu 55 D.J. Hughes and J.A. Harvey, Phys. Rev. 99, 1032 (1955).

Hu 67 R.R. Hurst and D.J. Donahue, Nucl. Phys. A91, 365 (1967).

Is 81 M.A. Islam, W.V. Prestwich and T.J. Kennett, Nucl. Instr. and Meth 85, 243 (1981).

Ja 75 H.E. Jackson, G.E. Thomas and K.J. Wetzel, Phys. Rev. 11(5), 1164 (1975).

Ka 52 L. Katz and A.S. Penfold, Revs. Mod. Phys., 24, 28 (1952).

Ke 69 M.A. Kelly, B.L. Berman, R.L. Bromblett, and S.G. Fultz, Phys. Rev. 179, 1194 (1969).

Ke 78a T.J. Kennett, P.M. Brewster, W.V. Prestwich, and A. Robertson, Nucl. Instr. and Meth., 153, 125 (1978).

Ke 78b T.J. Kennett, W.V. Prestwich and A. Robertson, Nucl. Instr. and Meth., 151, 285 (1978).

Ke 78c T.J. Kennett, W.V. Prestwich and A. Robertson, Nucl. and Meth., 151, 293 (1978).

La 60 R.W. Lamphere in Fast Neutron Physics, Part 1, Interscience Publishers Inc., N.Y., 454 (1960).

La 72 R.G. Lanier, T.J. Larsen, D.H. White and M.C. Gregory, Bull. Am. Phys. Soc. 17, 899 (1972).

Le 51 J.S. Levinger, Phys. Rev. 84(1), 43 (1951).

Le 78 C.M. Lederer and V.S. Shirley, Table of Isotopes, 7th Edition, John Wiley and Sons, New York (1978).

Lo 66 W.A. Lochstet and W.E. Stephens, Phys. Rev. 141, 1002 (1966).

Ly 69 H. Lyclama, T.J. Kennett and L.B. Hughes, Can. J. Phys. 47, 666 (1969).

Ma 60 J.B. Marion and J.L. Fowler, Fast Neutron Physics, Interscience Publishers Inc., N.Y. (1960).

Mc 77 J.E. McFee, Ph.D. Thesis, McMaster University (1977).

Me 58 L. Meyer-Shützmeister and S.S. Hanna, Bull. Am. Phys. Soc. 3, 188 (1958).

Me 66 J.L. Meason and P.K. Kuroda, Phys. Rev. 142, 691 (1966).

Mo 70 R. Moreh, S. Shlome and A. Wolf, Phys. Rev. C2, 1144 (1970).

Mu 60 C.O. Muelhause, in Fast Neutron Physics, Part 1, Interscience Publishers Inc., N.Y., 509 (1960).

Ne 60 J.H. Neiler and W.M. Good in Fast Neutron Physics, Part 1, Interscience Publishers Inc., N.Y. 509 (1960).

OC 62 J.S. O'Connell, P.A. Tipler and P. Axel, Phys. Rev. 126, 228 (1962).

Po 56 C.E. Porter and R.G. Thomas, Phys. Rev. 104, 483 (1956).

Pr 62 M.A. Preston, Physics of the Nucleus, Addison-Wesley, Reading, Mass. (1962).

Ra 67 N.C. Rasmussen, Y. Hukai, T. Inouye and V.J. Orphan, M.I.T. Report MITNE-85 (1967).

Re 70 D.H. Rester, W.E. Dance and J.H. Derrickson, J. Appl. Phys., 41(6), 2682 (1970).

Ro 72 A.A. Robertson, W.V. Prestwich and T.J. Kennett, Nucl. Instr. and Meth. 100, 317 (1972).

Ro 74 A.A. Robertson, Ph.D. Thesis, McMaster University (1974).

Ro 75 A.A. Robertson, G.C. Cormick, T.J. Kennett and W.V. Prestwich, Nucl. Instr. Meth. 127, 373 (1975).

Sa 74 G.R. Satchler, Physics Reports 14, 99 (1974).

Sa 80 W.C. Sailor and S.G. Prussin, Nucl. Instr. and Meth. 173, 511 (1980).

Se 77 E. Segrè, Nuclei and Particles, W.A. Benjamin Inc., Reading, Mass., 562 (1977).

Sh 80 K.S. Sharma, R.J. Ellis, V.P. Derenchuk, R.C. Barber and H.E. Duckworth, Phys. Lett. 918, No. 2, 211 (1980).

St 50 H. Steinwedel and J.H.D. Jensen, Z. Naturforsch, 5A(8), 413 (1950).

St 70 E. Storm and H. Israel, Nucl. Data A7, 566 (1970).

Wa 71 A.H. Wapstra and N.B. Gove, Nucl. Data A9, 561 (1971).

Wa 77 A.H. Wapstra and K. Bos, At. Data and Nucl. Data Tables 20. 1 (1977).

Wa 79 E. Warde, R. Seltz, G. Costa, D. Magnac and C. Geradin, J. de Phys., Lett. 40. L-1 (1979).

Wh 56 F.A. White, T.L. Collins and F.M. Rourke, Phys. Rev. 97, 1786 (1956).

Wy 65 J.M. Wyckoff, B. Ziegler, H.W. Koch and R. Uhlig, Phys. Rev. 137, 566B (1965).